Reduced-Order Cerebrovascular Modeling of the Aging Vascular System

by

Jeffrey D. Pyne

A dissertation submitted in partial satisfaction of the

requirements for the degree of

Doctor of Philosophy

in

Engineering – Mechanical Engineering

in the

Graduate Division

of the

University of California, Berkeley

Committee in charge:

Professor Shawn C. Shadden, Chair
Professor Tony M. Keaveny
Professor Chunlei Liu

Fall 2022

Reduced-Order Cerebrovascular Modeling of the Aging Vascular System

Abstract

Reduced-Order Cerebrovascular Modeling of the Aging Vascular System

by

Jeffrey D. Pyne

Doctor of Philosophy in Engineering – Mechanical Engineering

University of California, Berkeley

Professor Shawn C. Shadden, Chair

In medical conditions with disrupted cerebrovascular flow, including chronic alterations throughout aging or acute events such as ischemic stroke, cerebrovascular modeling can provide mechanistic and treatment insights. Reduced-order cerebrovascular modeling can be particularly useful for patient-specific or population-averaged cerebrovascular hemodynamics, where the governing flow dynamics include physically-driven non-linear constraints with active homeostatic regulation as well as highly variable and interconnected cerebral blood vessel networks. A coupled one-dimensional lumped parameter network (1D-LPN) cerebrovascular model is described with myogenic and CO_2 reactivity autoregulation modeling, circle of willis anatomical variations, cortical collateral flow compensation, cerebrospinal fluid generation/reabsorption, and intracranial pressure dynamics modeling. For parameter tuning of the numerous cerebrovascular model variables, a Bayesian optimization procedure establishes crucial parameter values with the remaining model parameters assigned through vascular aging and cerebral autoregulation quantitative population-averaged reviews. A specific focus on cerebrovascular aging alterations, a major source of vascular variance besides patient-specific variations, explores the parameter tuning procedure in a young population. The coupled 1D-LPN cerebrovascular model design, age-related vascular critical review, cerebral autoregulation critical review, and model parameter tuning procedure, comprises a prototype vascular test bed with the capability to model cerebrovascular-specific medical conditions while accounting for age-related vascular alterations.

To the lovely Melanie Brucks – May our vasculature grow old together

Contents

Acknowledgments

Inevitably, throughout the PhD experience, the success of an individual is largely influenced by their support group and those around them. I couldn't have asked for a better cohort of critically-thinking academics, life-long friends, and supportive family to encourage both my professional and personal development. I am forever grateful and appreciative to all of you.

First, I'd like to recognize my advisor, Shawn Shadden. Thank you for always giving me the freedom to explore all of my burning questions and guide me through the process of answering them. Exploring the physiological complexity of the brain has only deepened my curiosity and has provided endless questions to keep me busy for a lifetime.

Secondly, I'd like to thank my fellow PhD students and lab mates. Beyond all of the thoughtful and insightful discussions over the years, we managed to have a lot of fun and I'm honored to have shared this journey with you. Miguel, I know I can always rely on you for a meandering philosophical conversation. We have a lot to discuss. Sarah, I'm quite proud of us for maintaining the air recyclers in the lab thus keeping lab morale high. We have lots of cuttings to share. Debanjan, thank you for being my academic big brother and improving my spice knowledge. We have lots of spice combinations to experiment with.

To my family, thank you for your continuous support throughout the entire program. Mom, Dad, Jenny, and Eric, your encouragement and joyful times were such propellant through each step of my journey. Merrie and Rick, your exceptional advice and insight provided the optimal nozzle for that propellant.

Lastly, Melanie – I have you to thank for everything. Your role is incalculable and I'm endlessly grateful to have you in my life. Thank you for always inspiring me, believing in me, commuting hours and hours from our Burlingame (Millbrae) home, being there for the highs and lows, showing me the world, and for just being authentically you. Love you forever.

Chapter 1

Systemic Vascular and Cerebrovascular Aging Quantitative Critical Review

1.1 Introduction

With natural human aging comes many global vascular-related changes and subsequent potential cerebrovascular-related pathological events. Worldwide, cerebrovascular diseases represent a leading cause of death and disability, especially within the elderly population, while also placing a huge economic burden on the medical system and individuals [1, 2]. In particular, in diseases such as acute ischemic stroke [3], Alzheimer's disease [4, 5, 6, 7], vascular dementia [8, 9], leukoaraiosis, and intracranial atherosclerosis [10, 11] to name a few, there exists an interconnected mechanistic relationship between systemic vascular properties, vascular geometries, cerebral blood flow, and degree of ischemia. When studying these cerebrovascular diseases, establishing a proper baseline state for normal healthy aging becomes important so that pathological states can be built upon an existing reference point and disentangled from typical age-related changes. Proper attainment of this baseline healthy state could aid in both diagnosis of pathology severity and the evaluation of success potential between various treatment options. Due to the complexity of the human cerebrovascular system with its interdependent dynamics and sheer number of influencing variables across the cardiovascular system as well as their difficulty to experimentally and clinically measure, computational methods can provide a physics-based approach to establish a cerebrovascular healthy baseline state across aging.

1.1.1 Cerebral Autoregulation Mechanisms

For proper brain function, the human brain requires a continuous supply of blood flow to deliver oxygen, glucose, hormones, and nutrients to sustain neuronal activities such as gener-

ating membrane potentials and synthesizing neurotransmitters while additionally transporting metabolites like carbon dioxide and lactic acid to other parts of the body [12, 13, 14]. To maintain this critically important constant blood supply, the cerebrovascular system utilizes a protective autoregulation mechanism to prevent substantial increases or decreases in cerebral blood flow that is controlled across a complex signaling system. Physically, the autoregulation mechanism utilizes circumferentially-aligned tunica media smooth muscle cells to dilate or constrict pial and arteriole blood vessel diameters to modify cerebral vascular bed resistance in response to this signal [15, 16, 17]. The signal generation is based on an active feedback system that broadly has four main contributing pathways classified as myogenic, metabolic, biochemical, and neurogenic regulation [18, 19, 20]. The myogenic regulation is initiated when intima endothelial cells detect deviations from baseline levels of blood flow, specifically through mechanotransduction with changes in applied pressure (normal stress) and shear stress [21, 22]. The endothelial cells then translate this applied signal to activate the smooth muscle cells through various vasodilators and vasoconstrictors (also known as vasoactive substances) such as endothelial nitric oxide synthase, ion potassium channels [K^+] and reactive oxygen species [23, 24, 25]. The metabolic regulation is initiated during periods of elevated cerebral neuronal activity that brings about increased glucose utilization, oxygen consumption, and metabolites production such as carbon dioxide (CO_2), adenosine, and hydrogen ion [H^+] in the surrounding local parenchyma [26, 18]. These vasoactive metabolites then rapidly, with respect to the overall metabolic regulation, diffuse into the perivascular space to actively induce pial and arteriole smooth muscle cell relaxation through both direct interaction and by decreasing the baseline interstitial fluid pH creating a localized acidosis region [20, 26, 27]. The smooth muscle cells, surrounded by this local extracellular acidosis region, therefore have diffusion altered intracellular pH levels leading to a vasoactive response [28].

In biochemical regulation, through chemicals produced by the body such as nitric oxide or adenosine, there is considerable crossover and interdependence with myogenic and metabolic regulation. For the purposes of this classification, the authors will consider biochemical regulation to be autoregulation pathways outside of typical myogenic or metabolic response that are unique to age or disease. For example, blood brain barrier breakdown, cerebral inflammation, or ischemic injury [29]. Lastly, the neurogenic regulation of cerebral blood vessels is controlled via the autonomic nervous system. Broadly, the peripheral nervous system controls larger intracranial and pial vessel response while the central nervous system controls the smaller arterioles and capillaries [30]. Further, the parasympathetic and sympathetic nervous systems, through direct innervation, induce location-dependent vasoactive neurogenic regulation abilities that plays a role in neurovascular coupling (local cerebral autoregulation) [31, 32, 30]. From a sensory standpoint, baroreceptors, primarily located at the carotid sinuses and aortic arch, measure fluctuations in blood pressure and influence nerve signals to produce systemic cardiovascular response in the form of vascular bed and cardiac regulation [33]. Overall, these four interdependent autoregulation mechanisms work to actively maintain homeostatic human cerebral blood flow to sustain the body's essential organ.

1.1.2 Vascular Remodeling

As one of the most pronounced vascular consequences of aging, large elastic vascular stiffness increases over time [34]. Mechanistically, circumferentially-aligned functional elastin within the blood vessel wall degrade over time. This breakdown of functional elastin originates from multiple factors including pulsatile strain inducing material fatigue, age-related changes in signaling pathways, to calcification and cross-linking [35, 36, 37]. Throughout the elastin fatigue process, new elastin is generated within the blood vessels, evident by older and younger individuals having the same relative composition of elastin in the vascular wall, but the orientation and alignment experience modifications [37, 38]. In the place of the functional elastin, circumferentially-aligned collagen fibers begin to take more of the vessel pressure load, leading to an increase in overall vascular stiffness [36].

In response to vascular elastin fatigue, the body utilizes vascular remodeling principles to control blood vessel composition and morphology. Physiologically, vascular remodeling is the body's mechanism to maintain constant circumferential, axial, and wall shear stress (these three being the most sensitive directions) along the vascular tree [39]. Roughly, changes in hoop stress, wall shear stress, and axial stress will influence vascular thickness, diameter, and length, respectively [40]. This process happens quickly, in around a month's time, and can be observed across numerous pathological conditions including aneurysm formation and hypertension [41]. In the specific case of hypertension, significant vessel remodeling can be observed within two weeks [42]. Likewise, if normotension is returned, then the vessel returns to the original configuration. In aging, this process is non-reversible because the functional elastin is lost representing a lower limit of vessel compliance [41].

When considering human vascular remodeling, it is important to consider differences across arterial location and apply non-human cardiovascular aging data carefully. Regarding location, each artery with location-specific wall composition experiences varying degrees of pulsatile forces that change throughout age and lead to unique remodeling events. For example, across aging as elastic fatigue occurs, large human elastic vasculature, such as the aorta, will experience outward hypertrophic remodeling while arterioles will experience inward eutrophic/hypertrophic remodeling [43, 44, 45]. Additionally, chronic pathological conditions that alter blood flow will influence mechanical forces across the vascular bed inducing regionally-based inward/outward hypotrophic/hypertrophic remodeling [43]. Regarding non-human cardiovascular aging data, it is important to consider the cumulative vascular remodeling path when making corresponding conclusions about human data. For example, when comparing across non-human and human measurements, blood vessels often experience varying cyclic stress loads along different duration life spans that result in non-equivalent degrees of elastin fatigue. Therefore, the resultant material property changes and remodeling across non-human vascular beds are not directly analogous to human cardiovascular aging [37].

1.1.3 Quantitative Critical Review

As the brain ages, it experiences region- and diameter-specific modifications in both active and passive blood vessel material properties as well as more general changes in blood vessel morphology, arterial tree structure, and systemic cardiovascular changes, thus altering cerebrovascular flow in an age-related fashion. Additionally, beyond age-related changes, there is already considerable variability in homeostatic cerebrovascular flow and the bounds of cerebrovascular flow modification abilities across individuals. Pathological states and conditions further modify this already highly variable system obscuring whether cardiovascular alterations can be considered normal or abnormal. Establishing a more detailed fundamental age-dependent baseline to eliminate patient-specific variance is one potential strategy to separate the effects of age from patient- and pathology-specific variability. An age-dependent hemodynamic baseline has the potential to both improve our understanding of the aging cardiovascular system and pathological conditions confounded with age-related changes. With the growing prevalence of computational modeling, improved quantification of vascular aging could enhance vascular model predictions of how pathological alterations or treatment plans could impact essential hemodynamic features. This quantitative critical review works to establish a healthy baseline hemodynamic state across typical human aging, with special focus on cerebrovascular flow and cerebral autoregulation.

Beginning with the experimental foundation for age-related changes in the cerebrovascular system, quantitative evidence was compiled to provide the healthy aging basis for subsequent computational model tuning. Critical age-related observations taken into account include modifications of heart rate, cardiac output, blood pressure, flow distributions, vascular bed rarefaction, total cerebral blood flow, cerebrospinal fluid flow, atherosclerosis development, vascular stiffness, vascular thickness, tortuosity, passive/active blood vessel material properties, collateral rarefaction, pulse wave velocity, vascular tension and endothelial dysfunction. Additionally, static/dynamic autoregulation ability and CO_2 vasoreactivity along with autoregulation mechanism relative strengths are characterized. All of these changes are driven by various fundamental age-related biological mechanisms including elastin degradation due to pulsatile load, vascular remodeling, and biochemical regulation.

Throughout aging, there are additional vascular modifications that often occur concurrently with what is considered typical aging. One of the most critically important comorbidities is atherosclerosis. Atherosclerosis affects the vascular wall by increasing vascular stiffness, modifying blood flow patterns by stenosis of the affected vessels, and changes wall thickness, among other changes. Aging is difficult to disentangle from atherosclerosis since age-related changes in vascular stiffness make blood vessels more susceptible to vascular diseases such as atherosclerosis, thus creating a feedback loop [34]. Ideally, the global effect of these two vascular modifications could be handled completely independently, but practically it is challenging to separate the two. For the purposes of this quantitative critical review, adult human populations with the least degree of atherosclerosis were preferentially selected for inclusion. Additionally, adult individuals with cormorbidities that are known vascular modifiers such as diabetes, hypertension, cardiovascular disease, renal disease or cholesterol

will be predominately excluded from the following data. Overall, the selection of included data reflect, as much as possible, a healthy human adult population with ideal vascular aging. These data do not represent the 'typical' aging process, but instead an idealized population to isolate aging effects.

1.2 Age-Related Systemic Cardiovascular Changes

Globally, the cardiovascular system is entirely interconnected where one organ system's performance influences another organ system's ability to operate optimally. For example, atherosclerosis developing within systemic blood vessels requires the heart to work harder to pump equivalent blood flow due to an increase in vascular resistance. Changes in metabolic need of the brain across age by cerebral atrophy bidirectionally alters the total cerebral blood flow that supplies those territories while at the same time imposes shifting requirements to the heart. Across the body, it is clear that the systemic cardiovascular system is dynamically remodeling with age and a better understanding of these modifications and how they interact with each other could lead to insights in the aging process.

1.2.1 Heart-Related Changes

Starting with one of the most fundamental aspects of the cardiovascular system, across age, a heart rate decrease is noticed with women typically having faster resting heart rates than men [46]. Healthy adult women have heart rates following the linear relationship $HeartRate[\frac{beat}{min}] = -0.086 * age[yr] + 73.14$ while men follow the relationship $HeartRate[\frac{beat}{min}] = -0.079 * age[yr] + 68.61$ [46].

Cardiac output, the total flow circulated from the heart, is reasonably maintained throughout healthy aging after 20 years of age. There is a slight linear decrease in resting cardiac output with age following the equation[47]: $CardiacOutput_{resting}[\frac{L}{min}] = -0.045 * age[yr] + 8.344$. Typically, since cardiac output is dependent on body size, cardiac index (cardiac output / body surface area) is often reported as a way to normalize for an individual. Cardiac index at rest also decreases with age following the linear relationship [48, 49]: $CardiacIndex_{rest}[\frac{L}{min*m^2}] = -0.0133 * age[yr] + 3.5791$. While resting cardiac output/index is important to capture typical hemodynamic behavior, maximum cardiac output/index can be considered a more critical measure of cardiac aging since it determines the extent of cardiac ability. With healthy aging, maximum cardiac index goes through more substantial changes than the age-related decline of resting cardiac index [48].

Overall, these heart-related changes showcase a fundamental shift in the metabolic needs of the body combined with bidirectional structural changes to the cardiovascular system. The heart itself transforms throughout aging in terms of structure (thickness, material properties), size (weight, volume), ventricular dynamics, and composition [50, 51]. Yet, even with all of these age-related changes, the heart still maintains high efficiency, but with the loss of adaptiveness [51].

1.2.2 Systemic Blood Pressure

When looking on a population level, blood pressure as a cardiovascular metric is highly variable across individuals and is influenced by many factors including hypertension status, drug interactions, exercise, disease comorbidities, 'white coat' syndrome, body temperature, body temperature, and arterial stiffness to name a few.

Even within an individual, obtaining a mean blood pressure is not a straight forward task because there are even significant changes across very short-term (beat-to-beat), short-term (over 24 hours), and long-term (day-by-day to year-to-year) time periods [52]. For example, across 15 minutes of short-term blood pressure measurements, holding constant such variables as patient posture, respiratory variations, and time of day, systolic blood pressure has a mean variability of 4.1 mmHg ($\approx 4\%$) [53]. If these measurement variables are not adequately controlled, the short-term blood pressure variations within an individual become even more pronounced. For example, across the day, an individual can have up to a 20% drop in blood pressure when sleeping [52]. Regardless of these short-term variations within individuals, blood pressure trends happen across age for nearly all populations.

Table 1.1 showcases systolic and diastolic blood pressure for a healthy population and a more general population with more vascular risk factors across age and split by sex [46, 54]. In general, systolic blood pressure progressively increases and diastolic blood pressure decreases after 50 years old with all of these blood pressure curves following quadratic relationships with the most significant changes occurring later in life. For the differences across sex, the general trends remain consistent, but the mean male blood pressure remains higher [46]. For individuals without substantial vascular risk factors, representing our healthy population, the difference between systolic and diastolic blood pressure (pressure pulse) remains relatively constant following a positive linear relationship with advancing age [46]. For those with vascular risk factors, the pressure pulse trend remains similar to the healthy population up to 50 years old, but after 50 years of age begins to experience an amplification [54]. Consistently, without clinical blood pressure intervention, this finding is supported among populations with cardiovascular comorbidities across multiple studies [55, 56].

1.2.3 Systemic Macrovascular Flow Distributions

While there are substantial differences in blood flow distributions across individuals dependent on blood vessel anatomy, an establishment of a mean flow distribution across the entire body is critical to establish a baseline condition. By first establishing vascular territories across organs based on tissue volume and then distributing flow based on metabolic needs (following anatomical principles), a highly detailed vascular network of an average individual can be created [57]. Thus, by having a library of flow distributions across the body in such fine detail, computational models of vascular systems can be customized depending on vessels of interest.

Of interest to age-related changes beyond 20 years of age, it appears that the two major flow distributions alterations across healthy aging are to the brain [58] and kidney [59]

	Men	a	b	c	Women	a	b	c
ACCT	Systolic	0.002	-0.1262	125.72	Systolic	-0.0006	0.319	106.06
'Healthy'	Diastolic	-0.0044	0.4738	66.027	Diastolic	-0.0038	0.369	66.036
NHANES	Systolic	0.0002	0.2656	112.04	Systolic	0.0042	0.2402	99.51
'General'	Diastolic	-0.0135	1.3758	40.828	Diastolic	-0.0141	1.4776	34.136

Table (1.1) Systolic and diastolic blood pressure curve fitting across adult age (>20 years old) with sex-dependent splitting. The curve fitting takes the quadratic form: $BloodPressure[mmHg] = a * age^2[yr] + b * age[yr] + c$. The Anglo-Cardiff Collaborative Trial (ACCT) is built upon a healthy population with minimal vascular risk factors [46] while the United States National Health and Nutrition Examination Survey (NHANES) data represents a more general population complete with a typical distribution of vascular risk factors [54].

excluding cases of significant vascular modifications or pathological conditions. Specifically of interest for human cerebrovascular modeling, the ratio of flow from the ascending aorta distributing to the brain follows the negative linear relationship: $\frac{CBF}{CO} = -0.127\% * age[yr] + 22.72\%$ [58]. While the total cerebral flow distribution is lowered, along with the kidney flow distribution lowered, it appears that flow distributions to other organs and peripheral vessels are relatively preserved throughout aging [59]. This does not imply that flow to these regions remains static with age, only that the flow distributions across the body are preserved.

After determining macrovascular flow distributions, from a modeling perspective, systemic vascular resistance (total vascular resistance) and compliance are needed to properly populate boundary conditions. As the human body ages, arterial compliance decreases and vascular resistance increases. Based on invasive radial artery measurements, systemic vascular resistance follows the positive linear relationship $Resistance_{systemic}[\frac{dynes*s}{cm^5}] = 8.1 * age[yr] + 926.9$, large artery compliance follows the negative linear relationship $Compliance_{large}[\frac{mL}{mmHg}] = -0.02 * age[yr] + 2.51$, and small artery compliance follows the negative linear relationship $Compliance_{small}[\frac{mL}{mmHg}] = -0.001 * age[yr] + 0.113$ [60]. Overall, women have 16% higher systemic vascular resistance, 31% lower large artery compliance, and 45% lower small artery compliance for invasive measurements (8%, -17%, and -29% for non-invasive measurements, respectively) [60]. When measured with non-invasive means, systemic vascular resistance and large artery compliance were found to have equivalent age-related slopes [60]. Additionally, systemic vascular resistance can be highly variable within healthy populations [61]. From these total values, vascular resistance and compliance for individual arteries (branching vessels) are distributed based on blood flow distributions. Specifically, the values for branching resistance and compliance are calculated as a vascular network in parallel [62]. The total vascular compliance decreasing across age has implications

for total blood volume where a consistent age-related drop in total blood volume occurs [63].

1.2.4 Cerebral Vascular Bed Rarefaction

Over age, it has been observed that beyond the age of 30, humans experience cerebral atrophy. While total intracranial volume longitudinally remains constant, whole brain volume will shrink with ventricular volume increasing in its place [64, 65, 66]. Across a normative population of 199 subjects older than 38 years of age, not controlling for vascular comorbidities, the mean rate of total cerebral atrophy is approximately -.23 percent per year [64]. Additionally, the rate of total atrophy accelerates with advancing age following the quadratic relationship: $\%/year = -0.61 + 0.027 * age[yr] - 0.00035 * age[yr]^2$ [64]. Additionally, irrespective of neurodegenerative diseases and moderate vascular risk factors, certain brain regions may atrophy at higher rates in normal aging. These aging-related atrophy regions are primarily focused in the gray matter of the aging brain, while the white matter remains relatively fixed in volume [66]. For adults, the gray matter fraction, referenced to intracranial volume, follows the linear trend of $GrayMatter_{fraction}[\%] = 52.67 + 2.12 * I(sex) - 0.154 * age[yr]$ (where I(sex) = 1 for women and I(sex) = 0 for men) and the white matter fraction follows the quadratic trend of $WhiteMatter_{fraction}[\%] = 27.18 + 0.23 * age[yr] - 0.00288 * age^2[yr]$ [67]. When controlling for clinical hypertension and self-reported cognition changes across age, accelerated atrophy is present in the cerebral cortex (neocortex) within the parietal lobe (left planum temporale, bilateral angula and postcentral gyri), frontal lobe (left middle frontal and bilateral precentral gyri), temporal lobe (transverse temporal gyri), bilateral insular cortex, and bilateral cingulate cortex (anterior cingulate) [66]. When including individuals with hypertension and risk factors for vascular disease, typical comorbidities of an aging population, the regions of accelerated cerebral atrophy appears to include the perivascular region [64], hippocampus [65], and temporal lobe [65]. In particular, the hippocampus and temporal lobes have overlapping atrophy associated with neurodegenerative disease that drives the need for further disentanglement for patients with vascular risk factors [68, 69] while the perivascular atrophy appears to be more associated with normal aging [70].

1.2.5 Total Cerebral Blood Flow

Over normal human aging, along with cerebral brain volume atrophy, total cerebral blood flow subsequently decreases past 20 years of age [71, 72]. This decrease in total cerebral blood flow is positively correlated with the changing metabolism requirements of total neuronal activity across age. From a global perspective, as cerebral atrophy occurs across age, total neocortical neurons also subsequently decreases with density remaining constant across all regions [73]. To quantify neocortical neuron changes, the following two equations can be utilized with the former being more precise with additional information [73]:

$$Neuron\ Number = 10^9 * \exp(-3.406(+0.031\ if\ male)$$

$$+ 0.00018\text{*age[yr]}+0.579\text{*ln}(\text{V}_{cortex}[cm^3]) + 0.379 * ln(SA_{cortex}[cm^2]))$$

$$Neuron\ Number = 10^9 * \exp(3.050(+0.151\ if\ male) - 0.00145 * age[yr])$$

On average, after 20 years of age, this corresponds with a decrease in 85,000 neurons per day [73]. Over a time span of 60 years, cerebral total volume would decrease about 14% with around 8% decrease in total neurons for a healthy individual.

From a total cerebral blood flow perspective, it is critical to understand the primary metabolic need of the brain. One way to establish the age-related changes in metabolic requirements is to examine cerebral blood flow measured at the large blood vessels supplying the brain. From a healthy adult population perspective, compiled from multiple studies, total cerebral blood flow (tCBF) decreases approximately -3.4 mL/min annually [74, 71, 75]. When the effects of vascular risk factors such as diabetes, hypertension, stroke/TIA, and/or myocardial infarction are included (potentially a better metric for the general population), rate of annual tCBF change falls to approximately -4.3 mL/min [76, 77, 78]. The most important vascular comorbidities that influence tCBF, ranked from highest changes to lowest, include cerebrovascular disease, diabetes mellitus, peripheral vascular disease, hypertension, abdominal aortic aneurysm, current smoking, hyperlipidemia, and cardiovascular disease [78, 79]. While looking at change of tCBF across age, a more accurate and patient-specific approximation can be based on brain parenchymal volume [76]. This method is more accurate due to high brain volume variance among individuals (up to ≈50% for individuals of the same age) and because perfusion of parenchymal remains relatively constant throughout age [76, 72, 71, 79]. For those without vascular risk factors, the relationship between brain volume and tCBF is as follows: $tCBF[mL/min] = .59 * volume_{brain}[mL] - 6.17$ [72, 71]. For those with vascular risk factors, the equation is: $tCBF[mL/min] = .38 * volume_{brain}[mL] + 127.98$ [76].

When the brain is observed from both a global and local perspective, insights into age-related cerebral metabolic requirements can be quantified. For example, measures of glucose consumption and oxygen consumption, correlated with local cerebral blood flow, represent the energy requirements of the aging brain. Whole-brain quantification of metabolic variables, measured in adults primarily with uncorrected positron emission tomography (PET), indicates that total glucose consumption, oxygen consumption, and cerebral blood flow all significantly decrease and that oxygen extraction fraction significantly increases over age [80]. Based on a linear regression of uncorrected PET measurements, total glucose consumption, oxygen consumption, cerebral blood flow, and oxygen extraction fraction, change at annual rates of -0.6%, -0.4%, -0.5%, and +0.4%, respectively [80]. While this characterizes whole-brain changes, locally, there are regional differences in local metabolism requirements that vary in change across age [81]. If these changes of age-related metabolism are accurate, the causality of the age-related changes remain unknown; Does the aging brain require fewer resources or does disrupted resource delivery starve the brain into atrophy? For PET measurements specifically, due to the low spatial resolution, partial volume correction may be necessary in these cases of cerebral atrophy, such as in healthy aging and pathology, to

prevent measurement underestimations [82]. For example, when brain atrophy is controlled for, whole-brain mean cerebral glucose metabolism remains constant in healthy individuals across age [83, 84]. This trend also holds true for measurements of local cerebral blood flow remaining constant throughout healthy aging after the application of partial volume correction [85]. Accordingly, these findings imply that as global brain volume atrophies throughout aging, the glucose metabolism and cerebral blood flow requirements of the remaining brain volume could be holding constant. With additional evidence of neuron density remaining fixed with age [73], contingent on neuron metabolism efficiency holding constant, the loss of neurons due to atrophy would be the primary correlate for decreases of total cerebral blood flow.

1.2.6 Cerebral Venous Flow

For cerebral venous flow, it is expected that decreases in tCBF across age will be reflected in the venous output. Indeed, the decreases in venous flow across 43 years of age can be predicted from decreases in tCBF [86]. While it is known that cerebral veins experience thickening, stiffness increase, and increases in smooth muscle tone over age over age, the full cerebrovascular implications are not well understood [87, 88].

1.2.7 Cerebrospinal Fluid Flow

Cerebrospinal fluid (CSF), which resides throughout the cerebral ventricles and subarachnoid spaces, is responsible for transporting metabolic waste away from the brain, distributing nutrients, hormones, and neurotransmitters, maintaining a balance of electrolytes, and providing mechanical protection against sudden cerebral impact while under neutral buoyancy conditions [89]. In the traditional model for CSF flow, CSF is primarily generated in the choroid plexus contained within the ventricles, moves throughout the cerebral aqueduct, flows throughout the cerebral and spinal subarachnoid spaces to be finally reabsorbed into the venous system from the arachnoid villi [89, 90]. This critical system is prone to age-related changes in the form of increasing CSF volume (in the cerebral ventricles) while CSF flow rates actually decrease presumably resulting in less CSF turnover. In the cervical spine along the C2-C3 junction, CSF flow decreases with age following the equation $CSF_{cervical}[\frac{mL}{min}] = -0.1191 * age[yr] + 44.1$ [86]. Similarly decreasing is CSF flow in the cerebral aqueduct, with the ratio of change remaining constant with the cervical spine flow, following the equation: $CSF_{aqueduct}[\frac{mL}{min}] = -0.017 * age[yr] + 3.89$ [86]. Besides changes in flow rate, the shape of the CSF flow curves alter to become smoother over the cardiac cycle [86]. These changes in CSF flow over age have implications in the clearing of proteins especially important for neurological diseases [90, 86].

1.2.8 Atherosclerosis

Across age, it is very common for atherosclerosis to develop within arteries leading to the brain, specifically the aorta and carotid vasculature. While deviations in vessel diameter from atherosclerosis impact flow after significant vessel stenosis [91], atherosclerosis will also stiffen a vessel and can contribute to cerebrovascular disease [92]. Men have a higher tendency for atherosclerosis than women following the equation: % of men with atherosclerosis = $1.58{*}age[yr]{-}45.3$ [93]. Women follow a similar rate of atherosclerosis development following: % of women with atherosclerosis = $1.63 * age[yr] - 54.1$ [93]. Additionally, men typically have softer plaque formations which could have pathological implications for rupture risk based on material properties [93, 94].

1.2.9 Macrovascular Stiffness and Distensibility

Throughout the process of age-related remodeling, macrovascular stiffness increases / distensibility decreases in large elastic proximal arteries such as the aorta and carotid blood vessels. Stiffness and distensibility, in the context of blood vessel measurements, are considered closely related to each other, but not interchangeable. By definition, distensibility is defined as the inverse of the elastic modulus (a material-specific property also called Young's modulus), while stiffness represents a structure-dependent measure that incorporates both the elastic modulus and blood vessel dimensions [95]. Large elastic proximal arteries have multiple age-related alterations including fatigue-induced elastin degradation, collagen deposition at points of elastin degradation, collagen/elastin cross-linking, vascular smooth muscle cell stiffening, calcification, endothelial cell dysfunction, and inflammation, all of which contributes to vascular remodeling and, ultimately, increasing vascular stiffness with age [96, 97]. With large artery stiffness being highly variable across older individuals, levels of vascular stiffening can independently predict cardiovascular events and overall mortality risk [97, 98]. Large elastic proximal artery stiffening can lead to multiple cardiovascular cascades including increasing pulse pressure (difference between systolic and diastolic blood pressure), increasing arterial pulsatility transmission to low-resistance vascular beds such as the brain, and altered ventricular-arterial interactions [96, 97, 99].

In the human aorta, from the ascending to the abdominal aorta regions, circumferential stiffness, measured as tangential elastic modulus at physiological loading with biaxial mechanical testing, progressively increases across age [100]. Roughly, averaged across the sections of the aorta, the linear fitting of tangential elastic modulus across age leads to the following quantification: $E_{\theta\theta}[MPa] = 2.02E^{-2} * age[yrs] + 3.401E^{-1}$ (more specific quantification provided by [100]). This is supported by age-related stiffness index increases in the human abdominal aorta and common carotid artery as measured by ultrasound [101]. The primary blood vessel material property change across age is due to the substantial collagen fiber elastic modulus increase [102]. Similar to stiffness and elastic modulus changes with age, ascending aorta distensibility decrease is observed with age by magnetic resonance imaging (MRI) measurements with the greatest changes happening before 50 years old [103].

In the human carotid artery, distensibility decrease is observed once again with early life changes being the most prominent [104, 105, 106].

These is a difference in age-related stiffness response within large elastic proximal arteries that peripheral vessels do not mirror. For example, human femoral, radial, and brachial artery distensibility does not change or has less alterations with age when compared to larger proximal arteries [104, 107, 108]. This finding of age-independent stiffness in peripheral vessels is supported with mouse data where posterior cerebral arteries undergo age-dependent stiffness alterations while arterioles do not [109]. In rat cerebral arterioles though, vessel distensibility decreases with age [110]. Ultimately, further study is needed to locate the specific regions or limit of the human cardiovascular tree where arterial stiffness does and does not change significantly with age, especially in cerebral blood vessels. In the identification of age-independent stiffness regions, the classification based on vessel diameter may not necessarily be appropriate due to evidence of human middle cerebral artery stiffness alterations with age [111] paired with larger arteries such as the human femoral, radial, and brachial arteries having minimal distensibility modifications. Overall, larger elastic proximal arteries are the primary location in the human cardiovascular system that experience regional age-related vascular remodeling from circumferential wall stiffness increase.

1.2.10 Pulse Wave Velocity and Morphology

Pulse wave velocity (PWV), a measure of blood pressure wave speed between two arbitrary arterial locations [112], increases with aging and is often used as a surrogate measure of arterial stiffness. In principle, PWV can be measured across any arterial distance and within any artery / vascular pathways [112]. In particular, PWV measurement between the carotid and femoral arteries (cfPWV) is considered the gold standard in a clinical setting due to its simplified arterial length measurement and verified association with adverse cardiovascular events [113]. In fact, similar to age-related human stiffness findings, large elastic arteries have age-related PWV increases while muscular arteries have relatively constant PWVs with age, thus measurements of large elastic arteries are prioritized to capture age-related changes [114, 37].

In a population of 1455 healthy multinational subjects with no cerebrovascular risk factors and optimal to normal blood pressure ($BP \leq 120/80$ or $120/80 \leq BP < 130/85$), carotid-femoral PWV reference values are defined as a quadratic regression: $cfPWV_{optimal}[\frac{m}{s}] = 0.83E^{-3} * age^2[yr] + 5.55$ [115]. Generalized across a broader multinational population of 11,092 subjects, further quadratic fitting equations are provided for blood pressure categories ranging from normal to grade III hypertension as well as linear fitting equations for age brackets dependent on mean blood pressure [115]. In similar, but slightly lower $cfPWV$ values over age, 780 healthy participants residing in Tandil city, Argentina, with optimal to normal blood pressure, confirm age-related PWV trends [116]. In general, PWV variance and rate of increase is higher with older age, especially after 50 years of age [115, 116]. Overall, across the general population, age and mean blood pressure are both important

determinants of PWV with older age and higher mean blood pressure being associated with increased PWV [115] (gender does not play a significant role in PWV [115, 116]).

The pulse wave form, both flow or pressure, is comprised of both forward and backward waves. In the vasculature, the forward pulse wave, originating from the left ventricle, travels through the arterial system until an impedance change (such as branch points) reflects part of that forward wave into a backward pulse wave [37, 112]. The timing of these forward and backward waves modify the morphology of the pulse wave form and even have the potential to amplify aortic pressure. In younger vasculature with slower PWVs (thus, reflected waves return to the aorta slower), the backward wave often returns during the favorable time of diastole. In older vasculature with faster PWVs, the reflected backward pulse wave returns quicker during systole such that aortic pressure is amplified [37, 99]. The age-related pressure pulse amplification effect, known as augmentation, has consequences for the microvasculature due to the increasing pulsatility transferring down the arterial system and thus, increased potential for microvasculature damage that typically receives low pulsatility flow [37].

Pulse wave analysis, utilizing techniques that including identifying amplitude and timing of peaks to spectral analysis, the changing contour of the pulse wave can be quantified across aging. Pulse wave morphology analysis of an individual can be executed on multiple curves including the original pulse wave and higher order derivatives to extract characteristic metrics [117]. For example, in the original pulse wave, amplitude and timing curve characteristics such as the systolic peak, dicrotic notch, diastolic peak, crest time, reflection index, and duration of diastole can be identified, to name a few [117]. Similarly, local and global minima/maximas can be identified on the higher order derivatives [117]. Pulse wave metrics such as aortic pulse pressure, augmentation index, and augmentation pressure all increase with age while time of reflected wave and pulse pressure amplification all decrease [46, 117]. In particular, augmentation index may be one of the more sensitive metrics at younger age, while PWV may experience the most change at older age [46, 103, 118].

1.2.11 Systemic Arterial Blood Vessel Intima and Media Thickness

Arterial blood vessels, across the body, have significant age-related remodeling that results in alterations to the wall thickness of the blood vessel. Part of these age-related changes will encompass healthy vascular aging while other comorbid pathologies such as atherosclerosis can additionally influence thickness [106]. The blood vessel wall, responsible for withstanding the load of blood pressure, is comprised of the intima, media, and adventitia [119]. In terms of both age-related changes and withstanding pressure loads, the intima and media, play an important load. For example in aging, the intima-media layer thickness (IMT) is often used in the diagnosis for atherosclerosis since it is accepted that the intima layer (IT) experiences thickening as part of the atherosclerosis pathogenesis [120, 121]. Under typical physiological pressure loading conditions, both the intima and media layers (MT) take on the highest circumferential wall stress values while the adventitia protects against overstretching [122,

123, 124].

To characterize human arterial age-related healthy blood vessel thickness changes, data from MRI, ultrasound, and microscopy studies were quantitatively coalesced across the ascending aorta (AA), carotid arteries (CCA), and cerebral pial arteries. All of the following healthy populations from which data were extracted have sub-clinical, asymptomatic, or low-risk levels of atherosclerosis. Specifically, to observe age-related relationships in vascular thickness, diameter, wall thickness, and age data were extracted from studies examining human AAs [125], CCAs [106, 126], and pial arteries [127] as well as wall thickness constituent data (intima, media thickness/percentage) [128, 129, 127]. Data extraction are selectively provided based on data availability and to highlight, where appropriate, age-related changes.

Overall, across the entire range of vascular diameters (200 μm - 35 mm), media thickness (MT) and homeostatic lumen diameter follow a linear relationship ($MT[mm] = 0.059 * d[mm] - 0.025$). Specifically for pial arteries, to extract a more accurate fit due to smaller sample sizes, the linear relationship is: $MT_{pial}[\mu m] = 0.046 * d_{pial}[\mu m] + 5.55$. In terms of age-related diameter changes, the CCAs and pials have limited diameter changes, but the AAs follow the following linear relationship: $d_{AA}[mm] = 0.093 * age[yr] + 25.75$. With age-related thickness changes, the AAs and pials do not experience significant change in thickness, but the CCAs undergo age-related changes. Specifically, the CCAs undergo age-related changes in both intima thickness (IT) and media thickness (MT): $IT_{CCA}[\mu m] = 2.24 * age[yr] + 207.1$, $MT_{CCA}[\mu m] = 5.12 * age[yr] + 112.9$ with the healthy media layer changing more than the intima layer [129]. Normalizing by diameter, due to minor CCA diameter changes with age, the equations transform to: $(\frac{d}{IT})_{CCA} = -0.093 * age[yr] + 26.25$, $(\frac{d}{MT})_{CCA} = -0.248 * age[yr] + 32.11$. Of note, globally, when examining $\frac{d}{IMT}$ across many vessels including the carotid, common femoral, superficial femoral, popliteal, and brachial artery [106, 126], there appears to be a consistent age-related trend of $(\frac{d}{IMT}) = -0.075 * age[yr] + 14.35$. When controlling for arterial diameter, the data supports an age-related wall thickening pattern consistent across the vasculature [126]. In terms of vascular remodeling, this age-related characterization would be considered slightly-outward hypertrophic behavior [44].

1.3 Age-Related Cerebrovascular Changes

Specifically for cerebrovascular changes, a series of age-related alterations occur in cerebral microvascular flow distributions, tortuosity, collateral rarefaction, blood brain barrier, and endothelial dysfunction.

1.3.1 Cerebral Microvascular Flow Distributions

Once blood is traveling up the carotid and vertebral arteries, the next junction to significantly contribute to flow distributions leading to the cerebral lobes is the Circle of Willis (CoW) vascular structure. Located at the base of the brain, determined largely during embryological development, many possible anatomical variations of the CoW arise in terms of vessel

diameter and vessel existence [130]. Variations primarily exist in the posterior communicating artery, posterior cerebral artery (P1 segment), anterior cerebral artery (A1 segment), and anterior communicating artery showcasing the diversity of CoW possibilities [131]. The existence of or hypoplastic status of CoW arteries significantly alters blood flow between individuals and results in various blood routing pathways to ultimately reach cerebral territories [75, 72]. The CoW acting as a structure to counter pathological flow conditions is a fortuitous benefit to humans, but is likely not driven by evolutionary means as commonly cited [132]. Instead, the purpose of the CoW vascular structure could be to dissipate pressure across the cerebral arteries or an evolutionary mechanism to establish appropriate homeostatic flow distributions [132]. While total cerebral blood flow rates decrease with age, it appears that CoW blood flow distributions, controlling for CoW variations within a healthy population, are maintained throughout aging even with nonuniform cerebral atrophy [75].

To minimize inaccuracies in predicting flow rates within individual CoW blood vessels, diameter plays an important role. Cerebral blood vessel diameters can have significant variance across individuals with communicating arteries, such as the anterior and posterior communicating arteries, having the most variance [133]. Incoming arteries, such as the interior carotid arteries (ICAs) and vertebrals have the next highest variance with outgoing arteries, such as the second part of the anterior and posterior cerebral arteries and first part of the middle cerebral artery, having the least variance [133]. In the absence of blood flow measurements, "power-law" or "flow-splitting" techniques, based on Murray's Law, are often used to predict flow rates using diameter measurements of CoW blood vessels. In these conditions, Murray's Law would predict flow split exponential coefficient values of $n = 1.84 - 2.45$ for the CoW vessels and ICAs [134, 135] (Murray's Law for geometric topology exponential coefficient values at the CoW/ICAs are $n = 2.06$, while cerebral microvasculature has a larger variance with $n = 2.29 - 6.14$ [135, 136]). On the level of an individual, flow rates cannot always be accurately predicted based on diameter alone (with relative error of 20% at optimized empirical fitting of $Q = k * A^n$) [134], indicating the need for some blood flow measurements in computational modeling or alternate flow-splitting techniques, especially in pathological conditions [137]. While, objective flow divisions across the CoW remain constant with age, the Murray's Law geometrical and flow split exponential coefficient values decrease with age, likely due to age-related alterations in blood vessel geometry [135]. Overall, utilizing arguments derived from microvascular bed vascular scaling, whole vascular tree relationships, rather than individual bifurcations relationships, may result in more accurate flow split information [136]. For example, in cases of limited individualized flow measurements, optimization-based minimization procedures across the vascular tree of interest, when combined with flow splitting and hemodynamic constraints, can be an effective strategy for improving cerebral macrovascular flow split estimations [138]. In terms of age-related changes though, blood flow distributions throughout CoW anatomy can be assigned irrespective of age, but care must be taken in the flow split methods.

1.3.2 Cerebral Microvascular Bed Territories

Another approach for gaining insight into cerebral flow distributions is to look at the subsequent cerebral territories fed by the arteries. From a population-averaged standpoint, cerebral vascular territories have been categorized into atlases based on their major feeding artery [139]. From a patient-specific standpoint, cerebral homeostatic vascular territory identification could be measured via MRI using territorial arterial spin labeling (T-ASL) [140]. Even smaller blood vessel territories such as those fed by the branching middle cerebral artery (as well as the entire CoW) can be quantified using vessel-encoding arterial spin labeling (VE-ASL) [141]. While these homeostatic vascular territories are useful to quantify, it is also important to consider the significant extent of redundancy/collaterals within these vascular territories for cases of abnormal cerebral flow conditions such as ischemic stroke [142, 143, 144]. An additional complicating factor is that the arterial/venous composition highly varies depending on cerebral spatial location with gray matter having a distribution of up to three times more arteries than white matter and up to four times more veins [145, 146]. Ultimately, having a cerebral blood supply territory atlas that covers homeostatic vascular territories [147] as well as the total possible territorial range is ideal for abnormal flow conditions [148].

1.3.3 Cerebral Microvascular Bed Equivalent Vessel Radius and Length

For the purposes of computationally representing a vascular bed, often it is convenient to characterize the vascular bed behavior with an equivalent single vessel. To begin the characterization of the equivalent single vessel, the overall vascular bed resistance and volume are necessary. If only the starting branch of the vascular bed is known, such as in typical transcranial doppler (TCD) or MRI measurements, then, by making assumptions about consistent aspects of vascular bed structure, an approximation of vascular resistance and volume can be generated from only this starting branch geometry.

The primary assumptions for generating vascular bed structure include symmetric bifurcations down to the capillary level and that maximal blood volume will be provided to the tissue at minimum energy expenditure (also known as Murray's Law) [149]. Equations 1.1a and 1.1b represent these assumptions for vascular bed generation depicted as the relationship between parent and offspring vessel [149]. This form is particularly useful when a parent vascular radius and length are known such as in the case of clinical CoW imaging. The vascular radius and length of each generation can be approximated until the minimum of capillary radius is reached.

With the vascular bed characterized in terms of vascular radius, length and generation branch number, total vascular bed resistance and volume can be calculated using Equations 1.2a and 1.2b. At the smaller vascular radii ($\approx 300\mu m$), it is important to account for variations in viscosity [150, 151]. Lastly, utilizing the calculated vascular bed resistance and volume, a non-linear least squares problem can be solved for a single vessel equivalent

characteristics (r_{eq} and L_{eq}) using the Levenberg-Marquardt algorithm (Equations 1.3a and 1.3b). Experimental data shows that vessel diameter, measured at the level of the CoW, is correlated with its subsequent vascular territory size [152]. As expected, the equivalent single vessel representation of the vascular bed meets expectations of radius and length with respect to typical flow rates.

$$r_{offspring_i} = 2^{\frac{-i}{3}} * r_{original} \quad (1.1a) \qquad l_{offspring_i} = l_{original}/2^{\frac{i}{3}} \quad (1.1b)$$

$$R_{bed} = \sum_{i=generations} \frac{8\mu_i L_i}{\pi r_i^4 N_i} \quad (1.2a) \qquad V_{bed} = \sum_{i=generations} N_i \pi r_i^2 L_i \quad (1.2b)$$

$$R_{bed} = \frac{8\mu}{\pi} \frac{L_{eq}}{r_{eq}^4} \quad (1.3a) \qquad V_{bed} = \pi r_{eq}^2 L_{eq} \quad (1.3b)$$

1.3.4 Cerebral Microvascular Tortuosity

Cerebral age-related healthy arterial blood vessel increases in vascular resistance are partly due to increases in arterial tortuosity. Arterial tortuosity is defined overall as arteries that curve, curl, angulate, twist, loop, and/or kink [153]. Arterial tortuosity happens on an individual vessel level, not all vessels in a region will be tortuous, with tortuous vessels commonly found next to straighter vessels [154]. Various degrees of tortuosity occur across the vascular system with the aorta to capillaries having the potential to increase in tortuosity [153]. Importantly, tortuosity generation appears to start at mid-life, so observing vascular changes across a wide age-range is necessary when characterizing age-related tortuosity [154].

A possible hypothesis regarding the initiation and development of arterial tortuosity is based on mechanical instability and vascular remodeling [153]. In particular, a critical buckling pressure of an artery is based on age-related variables including vascular dimensions, material properties (wall stiffness), and loading conditions (axial tension) [153]. The acute buckling event of arteries could then develop into chronic vascular tortuosity after vascular remodeling [153].

Healthy age-related increases in human cerebral arterial tortuosity have been observed predominately in white matter arterioles [154] as well as in larger cerebral blood vessels [155]. In aged individuals ($>$ 40 years old), 8% of white matter arterioles experience severe tortuosity [154]. In contrast, preterm and young subjects ($<$ 40 years old) rarely have tortuous arterioles [154]. The stark contrast of age-related tortuous vessels in the white matter arterioles has led to the theory that the formation of blood vessel tortuosity begins in mid-life [154]. Interestingly, there exists a subset of aged individuals who do not present with significant vessel tortuosity [154], indicating a potential population in which to study tortuosity prevention through the mechanisms of personalized age-related vascular loading conditions and material properties.

1.3.5 Cerebral Microvascular Collateral Rarefaction

Of particular importance to abnormal flow conditions, which are more likely in aged individuals, are cortical/leptomeningeal collateral blood vessels. These vessels act as redundant flow structures running along the cortical surface of the brain that can reroute blood between cerebral vascular territories in need of supply when homeostasis is disrupted [156]. Their existence, similar to the CoW, significantly vary across individuals yet are highly deterministic of acute ischemic disease severity and efficacy of treatment [156]. The initial collateral vascular configuration and individual variance, has a genetic component [157, 158] while the remodeling/growth of collaterals over time has an environmental component based on changing flow conditions [159]. When analyzing the perfusion contribution of leptomeningeal collateral vessels in rats, in the case of complete middle cerebral artery (MCA) occlusion, rerouting to the distal MCA vascular territory can range from 25-100% compensation, depending on the vessel anatomy, showcasing the importance of these vessels [160]. In terms of absolute collateral flow, as evidence from mouse models, baseline flow is often much less than flow passing through the major cerebral arteries [161]. After MCA occlusion, flow within collateral vessels can increase up to 500-1000% [161].

While collateral vessels and their changes are inherently difficult to study in humans, due to the necessity of inducing abnormal flow conditions, mice are often used to study collateral changes across age. In mice, total cerebral collaterals decrease with age in both an absolute and relative sense compared against general vascular rarefaction along with an impaired ability to instigate remodeling [162]. Additionally, cardiovascular risk factors (especially hypertension) accelerate collateral rarefaction in mice [163] along with neurodegenerative diseases such as Alzheimer's [164]. On the opposing side, in mice, to maintain collaterals against age-related rarefaction, regular exercise is effective [165]. In adult mice, collaterals change through decreasing diameter, decreasing number, decreasing axial length and span, and decreasing tortuosity all resulting in increasing relative collateral resistance [162]. If this same mouse data can be extrapolated to human features [166], then age-related rarefaction of collaterals will result in the following approximate relative resistance change (compared to a baseline 27 year old individual) [162]: $RelativeCollateralResistance = 0.2748e^{0.0423*age[yr]}$. Additionally, collaterals, when compared against arterioles, experience equivalent absolute rarefaction in terms of vessel numbers, but collaterals are disproportionately lost due to a smaller starting amount [162].

Human data, though less rich, supports these mice findings, with age being a major determinate of fewer collateral vessel quantity [167, 168]. Additionally, metabolic syndrome in humans is associated with worse collateral status [169]. Of interest for cerebrovascular events is the collateral resistance between vascular territories that establish the maximum possible blood flow that can be shared among cerebral territories. By quantifying the typical leptomeningeal collateral distribution to cerebral territories, determined by vessel anatomy, the major cortical supply pathway can be further established. Based on leptomeningeal collateral number and average diameters, relative collateral resistances have been tabulated in Table 1.2 [170]. For determining absolute flow through collateral channels, of which human

	MCA-PCA	ACA-MCA	LACA-RACA	LPCA-RPCA	ACA-PCA
$R_{Relative}$	1	1.25	3.45	3.45	7.31

Table (1.2) Cerebral leptomeningeal collateral relative resistance between major vascular territories based on diameter and vessel number measurements within 10 typical brains [170]. Relative resistance is with respect to the MCA-PCA vascular connection. Symmetry applies between hemispheres. ACA = anterior cerebral artery territory, MCA = middle cerebral artery territory, PCA = posterior cerebral artery.

experimental evidence is lacking due to difficulty of measurement, if vascular anatomy is assumed then flow splits could be calculated or indirect methods could be utilized [171]. The inherent assumption in this calculation is that cortical leptomeningeal collaterals are the primary channel for rerouting of blood flow compared to micro-collateral connections on the arteriole level. Based on the degree of importance assigned to collateral existence in experimental acute ischemic stroke, it is reasonable to assume that the majority of collateral flow passes through these channels [172].

1.3.6 Blood Brain Barrier

The blood brain barrier (BBB), an essential divide between the central nervous system and circulating blood, experiences healthy age-related alterations though the consequence to BBB functionality is not well understood. One challenge in studying the BBB is that it is difficult to disentangle healthy age-related changes from disease-related changes, since normative individuals are not necessarily healthy and in both conditions the functional requirements of the brain are changing. In response to changing functional brain requirements, it is reasonable to assume that the BBB is modifying accordingly [173]. The primary known alternations to the BBB include functional alterations in leakage and convection transport, along with alterations to pericytes, astrocytes, endovascular cells, and the basement membrane [173].

As shown from dynamic contrast-enhanced MRI, modest levels of BBB leakage increase with age in both white and gray matter along with vulnerable age-related regions such as the hippocampus [174, 175]. In general, convection transport is reduced in the aging brain, such as in CSF turnover, perivascular movement, and arterial pulsations, though increased BBB leakage is an exception [173]. Other BBB anatomical age-related alterations include the reduction of pericytes, the potential reduction of astrocytes, and potential thinning of the endothelial glycocalyx layer, all of which can disrupt communication between endothelial cells and the neurovascular unit [173]. Additionally, the cerebral basement membrane thickens with age and could influence microvascular function within specific brain regions [173]. While the BBB experiences age-related changes, the consequences to blood flow disruption and subsequent cognitive function or disease pathogenesis are not yet well understood.

1.3.7 Cerebral Microvascular Endothelial Dysfunction

Endothelial cells, an essential component of autoregulatory regulation, are known to undergo age-related dysfunction in humans with implications for autoregulation ability and neuro-vascular coupling [176]. Endothelial cell dysfunction, in this context, is defined as an imbalance of oxidant, vasoregulatory, inflammatory, and thrombotic signals that endothelial cells typically provide in healthy blood vessels [177, 178, 179] (with, specifically, pro-oxidant, vasocontricting, proinflammatory, and prothrombotic signals increasing with endothelial dysfunction [178]). This imbalance in signals can have an important influence on age-related processes such as microvascular rarefaction [180] and atherosclerosis [181]. The source of age-related endothelial cell dysfunction, where cellular senescence modifies the endothelial cell phenotype [182], is theorized to originate from increased oxidative stress and inflammation [183, 178]. Important for autoregulatory vasoregulation, endothelial cells synthesize and release a vasodilator, nitric oxide (NO), which partly regulates basal tone and vasoregulation. NO bioavailability can highly influence blood vessels with 50% of basal tone in human brachial arteries being determined by NO bioavailability [181]. In endothelial dysfunction, decreased NO bioavailability becomes a hallmark feature that begins to influence basal tone and vasoregulation [177, 179].

In regards to vasoregulation, while bioavailability of the endothelium-derived vasodilator NO does not appear to affect myogenic ability [184], NO bioavailability does impact CO_2 reactivity ability [185]. To test these relationships, in age-matched populations of healthy, hypertensive, and diabetic participants, where hypertensive and diabetic conditions represent elevated endothelial dysfunction risk [186], blood pressure and end-tidal CO_2 levels are modulated with the inclusion of an external NO donor to determine the NO relevance to myogenic autoregulation and CO_2 reactivity [185, 184]. In healthy participants, an endothelium-independent NO donor reduces CO_2 reactivity ability [185]. This is directionally consistent with Figure 2.2b, where younger age (more NO bioavailability) corresponds with reduced CO_2 reactivity compared with older age. In participants with endothelial dysfunction risk, CO_2 reactivity is less sensitive than healthy participants and they are not as responsive to an endothelium-independent NO donor [184]. This data shows that modulation of NO levels has relevance for CO_2 reactivity in healthy individuals, thus implying interactions with endothelial dysfunction where endothelium-dependent NO synthesize and release is disrupted. Myogenic regulation remains consistent with and without the inclusion of external endothelium-independent NO donor across both healthy and endothelial dysfunction participants suggesting that NO has a minimal role in myogenic regulation [184] (consistent with no age-related change in static autoregulation see in Figure 2.1a).

Chapter 2

Cerebrovascular Autoregulation and Vascular Material Property Characterization

2.1 Introduction

For the behavior of cerebral autoregulation and vascular material properties, the characterization of components including myogenic static autoregulation ability, dynamic autoregulation ability, metabolic CO_2 vasoreactivity, passive tension, active tension, vascular diameter/tension bounds, and relative autoregulation contribution strength are critical to properly establish the complexity involved in intracranial dynamics. While some of the cerebral autoregulation behavior and material properties have age-dependent properties, all of the components have diameter-dependent properties based on the vascular bed location being examined. The characterization of age-dependent and diameter-dependent properties of cerebral autoregulation and vascular material properties informs cerebrovascular modeling of a specific location within a vascular bed corresponding with a particular age.

2.2 Static Autoregulation Ability

When defining cerebral autoregulation response, the most common depiction is established based on a pressure versus flow chart (Figure 2.1a) [187, 188]. The autoregulatory curve, in the pressure/flow context, can be broken into five key parts. One aspect of the autoregulation curve is the range in which autoregulation mechanisms maintain baseline cerebral blood flow over a span of systemic arterial pressure. The slope of this autoregulatory relationship, approximated as linear, is defined as S_{auto}. Beyond the autoregulatory maintenance range exists the linear slopes S_{hypo} and S_{hyper}, which characterize the flow/pressure curve in hypoperfusion and hyperperfusion states. The locations where baseline autoregulation is significantly disrupted, on both ends of the autoregulatory maintenance range, are called

the lower limit of autoregulation (LLA) and the upper limit of autoregulation (ULA). The lower limit of autoregulation, in particular, is one of the most important variables for pathology involving hypoperfusion, while the upper limit of autoregulation relates to pathological hyperperfusion [188]. Of note, this autoregulation behavior depiction is best characterized as 'static' autoregulation where autoregulatory mechanisms have been given adequate response time to reach steady-state conditions [187, 188]. Conceptually, this characterization of autoregulation does not always correspond to clinical experience due to dynamic forces present, but instead provides the mechanistic foundation of the autoregulation mechanism [187].

To appropriately characterize static autoregulation relationships, arterial blood pressure must be modified over a large range while cerebral blood flow, or a proxy, is measured. Additionally, augmentation of blood pressure (rather than spontaneous changes) can allow for larger blood pressure ranges to be measured [189]. Reliance upon pharmacological agents for the modification of blood pressure is discouraged in these measurements due to their potential interaction with autoregulatory mechanisms [188]. While autoregulatory measurements are ideally captured in large diverse populations, both with and without cardiovascular risk factors, testing of this type has only been performed in limited groups with healthy aging [190, 189, 191]. While autoregulation slopes and limits vary highly across individuals [31], population-averaged trends have been compiled based on best-available data within Table 2.1. Insufficient data exists to solidify age-related conclusions about relative static autoregulation changes, as age-related data comprises mostly of pharmacologically-driven blood pressure modifications [192], so additional studies are needed to expand upon the existing literature to exclude pharmacological interactions. Additionally, it is important to recognize that static autoregulation relationships are modified in pathological conditions so further research quantifying alterations is needed [191, 193].

Regarding the bounds of autoregulation ability, critically important for characterizing responses to acute ischemic stroke or complete vessel occlusion, an internal carotid compression experiment on human subjects is another possible experiment that can provide quantitative maximum vascular bed dilation. As the compression ratio of the internal carotid artery increases during this experiment, restricting blood flow to the brain, the subsequent autoregulation response will reach maximum myogenic vasodilation [195]. For healthy, young (late 20s), normotensive subjects with no vascular risk factors, the maximum myogenic vasodilation autoregulation bound is a 42% increase in MCA flow velocity from baseline after internal carotid artery compression [195]. Extrapolating with reasonable assumptions for transcranial doppler velocity measurements, such as circular and constant vessel cross-section [196], and sufficient distance from bifurcations at the measurement location, the approximate maximum volumetric flow rate vasodilation autoregulation bound can be considered 21% for young healthy individuals [197]. The bound of maximum vasodilation autoregulation can vary highly across individuals, at this young age, with the possible range of response spanning from 20-80% increase in MCA velocity (10-40% flow) [198]. The variability seen in vasodilation response is partly due to patient-specific differences in autoregulation ability, but could also be arising from differences in leptomeningeal collateral flow ability as flow is

	M1 Measurement [cm/s/mmHg]	tCBF Conversion [mL/min/mmHg]		Pressure Limits [mmHg]
S_{hypo}	0.75	7.86	LLA	-2.88
S_{auto}	0.02	0.23	-	-
S_{hyper}	0.91	9.55	ULA	+4.88

Table (2.1) Static autoregulation curve descriptions based on healthy population-averaged data. Slopes for autoregulation behavior zones, S_{hypo}, S_{auto}, S_{hyper}, were originally measured in the units of [cm/s/mmHg] within the M1 cerebral branch [190, 189]. The conversion to total cerebral blood flow (tCBF), with units of [mL/min/mmHg], is based on assumed arterial diameters [194] and the assumption of consistent slopes across similarly sized vessels. The lower and upper limits of autoregulation, LLA and ULA, are relative comparing to mean arterial blood pressure baseline [191]. All table metrics are based on non-pharmacological augmented blood pressure changes in healthy individuals.

shared from the non-blocked side.

2.3 Dynamic Autoregulation Ability

While static autoregulation is a convenient way to characterize expected blood flow changes over longer time scales (also known as steady state), autoregulation mechanisms are unable to immediately respond to alterations in blood flow. Therefore, there is a time delay in active blood flow response (also known as transient) that is designated as dynamic autoregulation. Conceptually, autoregulation response delay lies on a continuum that spans across the characterizations of static and dynamic autoregulation [187], but it is often convenient to separate these characterizations depending on the application or measurement technique. It is important to mention that static and dynamic autoregulation appear to be governed by the same underlying regulation mechanisms [190] even though existing indices of static and dynamic autoregulation health are not often correlated [199]. Static autoregulation can be roughly binned into response time domains greater than 30 seconds (oscillations of 0 - 0.03 Hz), while dynamic autoregulation can be binned into faster response rates (0.03 - 0.35 Hz) [187]. In general, dynamic autoregulation response is better at regulating slower changes in blood pressure and flow (low frequency) than faster ones. This means that dynamic autoregulation can be thought of a "high-pass filter" meaning that fast changing blood pressure and flow changes effectively transmit beyond the control of autoregulation mechanisms [190, 200].

Dynamic autoregulation can be characterized and visualized in multiple ways, each with their own usefulness. A prominent characterization is defining dynamic autoregulation as

a time constant that governs response rate. A time constant, in this context, dictates how fast active blood flow responses occur in response to a hemodynamic alteration which is generalizable across variable situations. In studies of healthy human participants, dynamic autoregulation time constants, in units of seconds, can be binned into regulatory mechanism: $\tau_{myogenic_{pressure}} = 6.7$ [201], $\tau_{neurogenic} = 8.3$ [201], and $\tau_{myogenic_{shear}} = 60$ [201]. In this context, a higher time constant means a longer delay for an active response, therefore myogenic pressure and neurogenic regulations are fastest, followed by slower myogenic shear regulations.

Overall, another representation of global dynamic autoregulation can be in the form of pressure/flow relationships similar to representations of static autoregulation. Figure 2.1b illustrates how faster oscillations of blood pressure and flow, within the active autoregulation region (S_{auto}), are progressively less regulated until fast enough oscillations result in essentially a passive vascular response [190]. This characterization similarly confirms that faster blood pressure and flow oscillations are not effectively regulated by autoregulation while slower oscillations are controlled (Table 2.2).

Similar to static autoregulation, insufficient data exists to produce definitive conclusions on age-related changes in dynamic autoregulation ability, though recent evidence is in support of age-related alterations both in autoregulation and cerebrovascular reactivity. In order to properly measure dynamic cerebral autoregulation, one major challenge is reproducibility using current transcranial doppler observation including transfer function analysis-(TFA), autoregulation index-, and correlation coefficient-type analysis methods [202]. While some dynamic cerebral autoregulation methods have methodological concerns that need to be taken into account, TFA gain measurement within the low frequency range (0.07 - 0.2 Hz) produces the most repeatable results [202]. Keeping these methodological considerations in mind, conclusions on human age-related changes of dynamic cerebral autoregulation have been reviewed only considering TFA gain measurements. Both TFA gain values and $\%\Delta MCA_v/\%\Delta MAP$ are seen increasing across advancing age, suggesting reductions in healthy cerebral dynamic autoregulation efficiency [203, 204]. Another study, though, showed the opposite gain relationship highlighting the need for further research [205]. While other studies do not support this finding of age-related change, lower sample sizes or small age gaps could be explanatory factors [206, 207, 208, 209]. Additionally, normalized dynamic autoregulation ability appears to be consistent across vascular territories suggesting that the brain does not have a heterogeneous dynamic autoregulation ability [210].

2.4 Cerebrovascular CO_2 Vasoreactivity

An important part of autoregulation response is metabolic autoregulation, also known as cerebrovascular CO_2 reactivity. Conceptually, from a tCBF response perspective, cerebrovascular CO_2 reactivity can be thought of as a modification to the static autoregulation curve where greater than baseline levels of CO_2 (hypercapnia) moves the lower and upper limit of autoregulation ability closer together (shrinks the pressure range where cerebral blood flow

Oscillation Frequency	0.03 Hz	0.04 Hz	0.05 Hz	0.06 Hz	0.07 Hz	0.08 Hz
S_{hypo} [cm/s/mmHg]	0.88	1.23	1.07	0.84	0.91	0.81
S_{auto} [cm/s/mmHg]	-0.02	0.02	0.28	0.37	0.53	0.56
S_{hyper} [cm/s/mmHg]	0.97	1.07	1.09	1.17	1.01	0.89
Oscillation Frequency	0.03 Hz	0.04 Hz	0.05 Hz	0.06 Hz	0.07 Hz	0.08 Hz
S_{hypo} [mL/min/mmHg]	9.19	12.85	11.18	8.77	9.51	8.46
S_{auto} [mL/min/mmHg]	-0.21	0.21	2.92	3.86	5.54	5.85
S_{hyper} [mL/min/mmHg]	10.13	11.18	11.39	12.22	10.55	9.30

Table (2.2) Dynamic autoregulation curve descriptions based on healthy population-averaged data. Slopes for S_{hypo}, S_{auto}, S_{hyper} were originally measured in the units of cm/s/mmHg within the M1 cerebral branch at varying oscillatory lower body negative pressure [190]. The conversion to tCBF mL/min/mmHg, for reference, is based on assumed arterial diameters [194] and the assumption of consistent slopes across similarly sized vessels. All table metrics are based on non-pharmacological augmented blood pressure changes in healthy individuals.

can be maintained at baseline) [211]. It is less clear what happens in lower than baseline levels of CO_2 (hypocapnia), but the static autoregulation curve could be modified in the same or opposite manner to hypercapnia [211]. This modification of the static autoregulation curve occurs because CO_2 is a contributing component to vasodilation/vasoconstriction that modifies vasomotor tone and, once active, leaves a modified range for myogenic autoregulatory response. Additional factors regulating CO_2 reactivity, beyond pH levels driven by CO_2 diffusion in the perivascular space, include state-dependent factors such as O_2 and mean arterial blood pressure (MAP), as well as the time-independent factor of age. Due to the indirect nature of this metabolic response primarily regulated through perivascular pH levels, vasoactive response is often experimentally manipulated through systemic stimuli such as modification of blood arterial partial CO_2 pressure (pCO_2) to determine autoregulation reactivity response [212]. This is due to CO_2 being able to readily pass through the

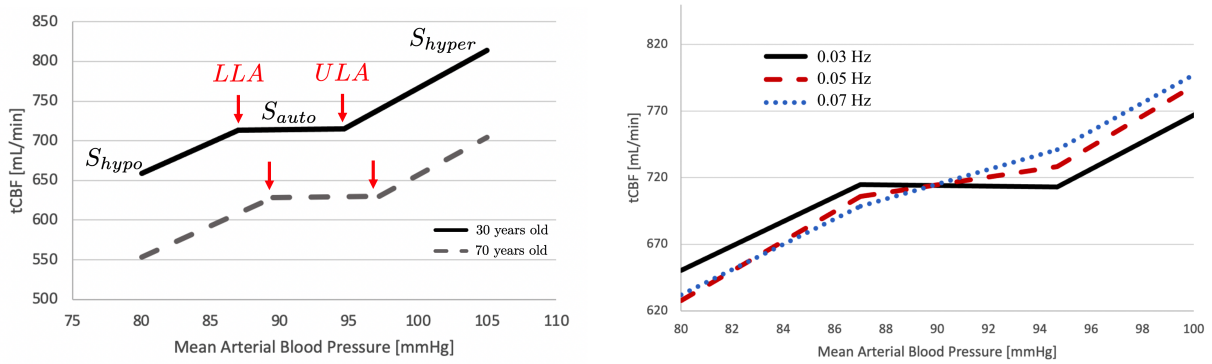

(a) Static autoregulation

(b) Dynamic autoregulation

Figure (2.1) a) Representation of static autoregulation behavior complied across healthy population-averaged measurements. While more data is needed on aged static autoregulation trends, the older population representative curve maintains relative behavior while being shifted to the right and down. To create these curves, homeostatic tCBF (section 1.2.5) was determined from population-averaged total brain volume trends [66] and slope/limit values were taken from Table 2.1. Arterial mean blood pressure was determined from Table 1.1. Age was set at 30 and 70 years of age to showcase absolute changes in static autoregulation curves while relative curve shape was maintained. b) Representation of autoregulation behavior, spanning static to dynamic, for a healthy 30 year old. To create these curves, homeostatic tCBF (section 1.2.5) was determined from population-averaged total brain volume trends [66] and slope/limit values were taken from Table 2.2. Arterial mean blood pressure was determined from Table 1.1.

blood brain barrier to affect to the local region by increasing pCO_2 [213].

To set a reference point for the healthy population-based curve defining CO_2 reactivity, measurements of tCBF alterations driven by changes in $P_{a_{CO_2}}$ levels within young adults (22 years old) were first extracted at baseline O_2 and MAP [214]. This baseline CO_2 reactivity data, equivalent in response regardless of brain region [214], were fit to a sigmoidal function presented in Figure 2.2a [215] (specifically, the variables of $tCBF_{min}$, $tCBF_{max}$, $P_{a_{mid}}$ and $k_{baseline}$ were fit in Table 2.3). The generalizable sigmoidal form (Equation 2.1) characterizes general CO_2 reactivity and includes the ability to capture changes in response to alterations in age, O_2, and hypotensive MAP. In particular, the approximate slope of the sigmoidal function (Equation 2.2) can be governed by normalized variables ($\bar{k} \in [0, 1]$) representing changes in age, O_2, and MAP (Equation 2.3a). For the primary modifiable variables, the data extraction goals of human measurements and tCBF measurements were not always possible in all conditions, but reasonable surrogates were utilized. The generalizable sigmoidal form (Equation 2.1) can also be utilized for characterizing O_2 reactivity, which is weaker than CO_2 reactivity, but still an important consideration in autoregulation response. Additionally, all CO_2 and O_2 measurements were converted to arterial partial pressures (as opposed to

end tidal values). The relationships used for conversion are as follows: $P_{a_{CO_2}}[mmHg] = 0.882 * P_{ET_{CO_2}}[mmHg] + 2.47$ and $P_{a_{O_2}}[mmHg] = 0.806 * P_{ET_{O_2}}[mmHg] + 8.3$ [214].

The change in heart rate throughout CO_2 and O_2 reactivity experiments does partially contribute to the change in tCBF. In the context of these experiments, when the influence of heart rate on tCBF is controlled for, the isolated tCBF behavior due to change in pCO_2 and pO_2 is uncovered. To control for heart rate, the influence of heart rate change on cardiac output ($CO = SV * HR$) is first quantified by canine fitting data of stroke volume slope over change in heart rate (dSV/dHR) normalized to human data ($CO[L/min] = (-2.1E^{-9} * HR^3 + 1.395E^{-6} * HR^2 - 3.53E^{-4} * HR + 0.129) * HR[beat/min]$) [216]. Then, the difference in cardiac output due to heart rate is then converted to tCBF assuming a fixed tCBF/CO ratio. When controlling for heart rate changes, tCBF alterations due to O_2 reactivity could be explained by heart rate changes alone. Likewise, the sigmoidal behavior of CO_2 reactivity becomes less sensitive when heart rate is controlled for. The fact remains that the changes in heart rate are an aspect of the CO_2 and O_2 reactivity, thus the tCBF quantification from Table 2.3 include the influence of heart rate. This investigation into heart rate changes suggests that CO_2 and O_2 reactivity mechanisms influence not just cerebral autoregulation but systemic vascular system response.

When quantifying the relationship between cerebrovascular CO_2 reactivity and age, the compilation of data utilized were collected in humans with the measurement of MCA velocity change across CO_2. In aggregate, CO_2 reactivity becomes more efficient across healthy aging (Figure 2.2b) with CO_2 reactivity under hypercapnia conditions, in particular, driving the response gain [217, 204, 218, 219, 220, 221]. While this age-related CO_2 reactivity change data relies upon MCA velocity measurements that become inaccurate surrogates of tCBF at the extremes of CO_2 measurement levels [214], this represents the best data currently available. The age-related data has been binned into hypocapnia and hypercapnia responses with $\bar{k}_{age_{hypercapnia}} = 1/(0.012 * age[yr] + 0.74)$ and $\bar{k}_{age_{hypocapnia}} = 1/(0.0036 * age[yr] + 0.92)$ (combined response is reported in Equation 2.3b). It remains plausible that CO_2 reactivity response in hypocapnia becomes less effective with age (representing a 'shift' in midpoint vasomotor tone), though experimental challenges could obscure this observation because it is more difficult to produce severe levels of hypocapnia than hypercapnia (studies with more pronounced hypocapnia tend to observe decreasing effectiveness with age [217]). Endothelial dysfunction and the decreased release of nitric oxide, which is associated with healthy aging but is most prominent in cases of hypertension or diabetes, is a primary cause of CO_2 reactivity impairment [184, 179].

In the physiological states of hypoxia and low blood pressure, the response of CO_2 reactivity is damped seemingly to favor vasodilation for oxygen delivery and maintenance of cerebral perfusion pressure. Specifically, for the interaction between O_2 levels and CO_2 reactivity, measurements in human subjects supports that acute hypoxia attenuates CO_2 reactivity [222]. While hyperoxia does not appear to significantly influence CBF [214, 223], there is limited data on the interaction with CO_2 reactivity, therefore the assumption of a linear relationship for Equation 2.3c is only relevant from baseline to hypoxic conditions. To gather data on the relationship between cerebrovascular CO_2 reactivity and hypotension,

	$tCBF_{min}$ [mL/min]	$tCBF_{max}$ [mL/min]	$P_{a_{mid}}$ [mmHg]	$k_{baseline}$
CO_2 Reactivity Fit	261.05	1391.45	49.89	8.24
O_2 Reactivity Fit	522.76	736.56	43.10	-1.00

Table (2.3) This table represents the variable fitting ($tCBF_{min}$, $tCBF_{max}$, $P_{a_{mid}}$, and $k_{baseline}$) for cerebral CO_2 and O_2 reactivity based on experimental data [214]. The baseline response is defined at 22 years old with 92 mmHg arterial partial pressure of O_2 at $1\overline{MAP}$. While CO_2 reactivity is dependent on age, O_2 and $\overline{MAP}$, there is not yet evidence that O_2 reactivity modulates in a similar fashion. While O_2 is fit to a sigmoidal function here with a low $tCBF_{max}$ limit, O_2 reactivity may be represented with an alternative function, such as a decreasing exponential, if more data is collected (as illustrated by [225]). Modifiers to k (equation 2.3a), equations 2.3b, 2.3c, and 2.3d are only relevant for CO_2 reactivity.

data from canines [224] were relied upon to capture the wide range in hypotensive MAP that would be hazardous to perform in humans. In particular, the interaction between MAP and CO_2 reactivity hints at the interaction between myogenic and metabolic autoregulatory forces. At very low MAP, myogenic forces become completely dominant over metabolic forces [224]. Combined hypocapnia and hypercapnia responses are characterized in Equation 2.3d to normalized baseline MAP relevant for hypotension ($\overline{MAP} \in [0, 1]$). Examples of the influence of O_2 and MAP on CO_2 reactivity are provided in Figure 2.2b.

$$tCBF(P_a) = tCBF_{min} + (tCBF_{max} - tCBF_{min}) / \left(1 + exp\left(\frac{-(P_a - P_{a_{mid}})}{k}\right)\right) \quad (2.1)$$

$$tCBF'(P_{a_{mid}}) = \frac{tCBF_{max} - tCBF_{min}}{4k} \quad (2.2)$$

$$k = k_{CO2_{baseline}} * \bar{k}_{age} * \bar{k}_{O_2} * \bar{k}_{MAP} \quad (2.3a)$$

$$\bar{k}_{age} = 1/(0.0077 * age[yr] + 0.83) \quad (2.3b)$$

$$\bar{k}_{O_2} = 1/(0.0113 * P_{a_{O2}}[mmHg] - 0.04) \quad (2.3c)$$

$$\bar{k}_{MAP} = 1/(1.490 * \overline{MAP} - 0.44) \quad (2.3d)$$

2.5 Passive Cerebrovascular Tension Curve Morphology

Seemingly, one of the biggest vascular alterations with age is the stiffening of passive mechanical properties. Specifically, mechanical properties of human intracranial arteries can

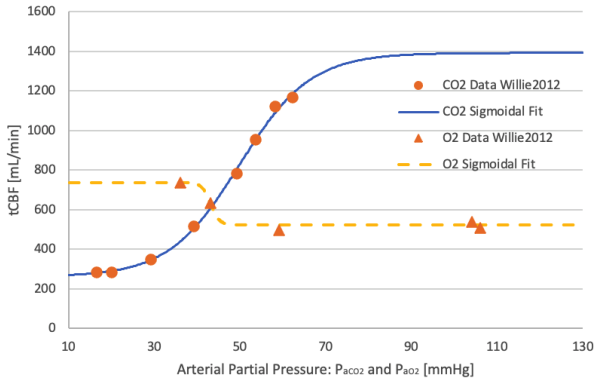

(a) CO_2 and O_2 Reactivity

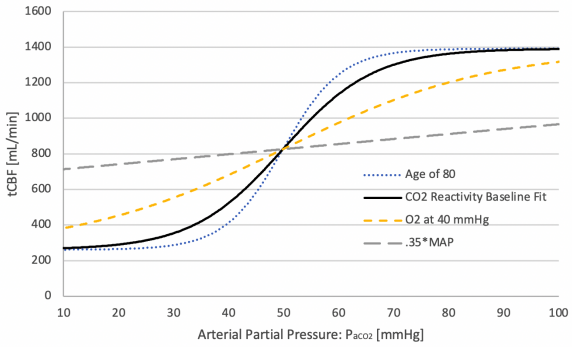

(b) Examples of CO_2 reactivity changes across age, $\overline{MAP}$ and O_2.

Figure (2.2) a) CO_2 and O_2 reactivity curves, fitted from experimental data [214], represent the baseline human response (Table 2.3). The baseline response is defined at 22 years old with 92 mmHg arterial partial pressure of O_2 at $1\overline{MAP}$. Overall, the CO_2 reactivity response is significantly more sensitive than O_2 reactivity, though CO_2 reactivity response interacts with O_2 partial pressure. b) The CO_2 reactivity curve can be modulated by multiple variables including age, $\overline{MAP}$ and O_2 (Equation 2.3a). In cases of older age, CO_2 reactivity becomes more effective, while excessive decreases of $\overline{MAP}$ or O_2 can effectively eliminate CO_2 reactivity. The example curves, with one variable modulated at a time to provide the extreme response ranges, are calculated at 80 years of age, 40 mmHg of O_2 arterial partial pressure, and $.35\overline{MAP}$.

be represented as the force required to stretch a blood vessel (circumferential tension) at different radii. The passive mechanical properties of the blood vessel are established from the composition of the vascular wall including elastin, collagen, etc. Of note, experimental human data of aging blood vessels is essential to collect because age-related fatigue of elastin is different in mice unless sufficiently matched [226].

Using pressure-inflation testing of vertebral arteries, passive tension across lumen radius can be experimentally measured over a wide range of ages [227]. While these passive tension curves give insight into vertebral vessels at a specific age, building a more generalizable form, such as an age-moderated exponential regression normalized to homeostatic radius and homeostatic tension, would allow for more extensive application. First, the mechanical behavior of individual vertebral passive tension curves [227] are well fit to exponential-type curves ($f(x) = ae^{bx}$). By then fitting the exponential coefficients, a and b to age, the age-moderated exponential regression can be established ($f(x, age) = a(age)e^{b(age)x}$). For normalization of passive tension, homeostatic tension and homeostatic radius were selected (as opposed to maximum passive tension), for better compliance with clinical and computational analysis. By using the experimentally-measured values of unstretched radius, homeostatic tension, and homeostatic circumference [227], a normalized relationship can be founded.

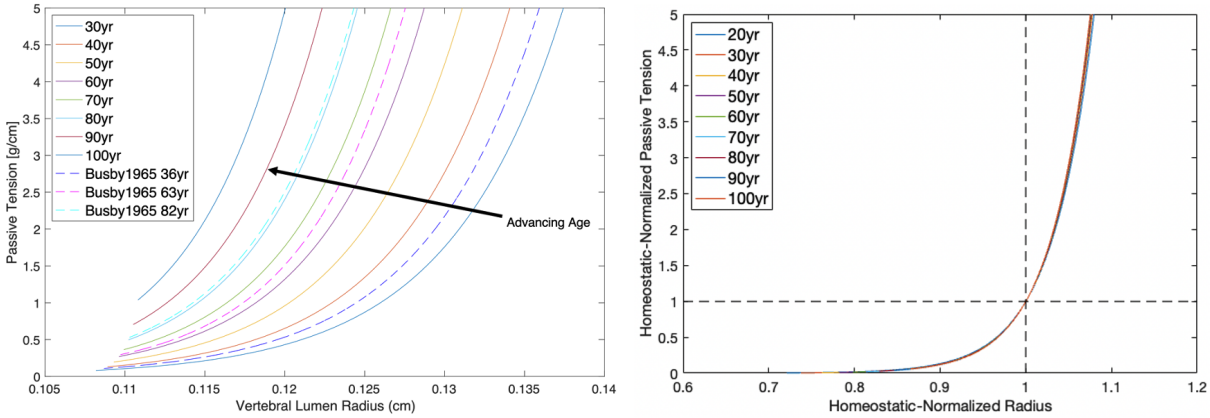

(a) Absolute human vertebral artery passive tension over age.

(b) Normalized human vertebral artery passive tension over age.

Figure (2.3) a) Calculated and experimental age-dependent absolute passive tension curves of human vertebral arteries. Data extracted and modified from [227]. Calculated curves are derived from age-moderated exponential regression. b) Calculated normalized age-independent passive tension curves across normalized lumen radius. Normalized tension and radius are with reference to the homeostatic configuration.

When passive tension is observed in absolute terms (Figure 2.3a), there are significant age effects [227]. The absolute age-dependent passive tension trend is driven primarily by the reduction of homeostatic radius with age [227]. When normalized to homeostatic tension and radius, the age-dependent effects of the passive tension curves diminish by collapsing to a single curve (Figure 2.3b). The following age-independent homeostatic-normalized tensile curve for passive tension over lumen radius, comprised of elastin, smooth muscle cells, and most importantly for tensile mechanical properties, collagen stiffness, is characterized as: $\overline{T}_{\theta\theta passive} = 6.44E^{-10} * e^{21.16*\overline{r}}$. Importantly, while the relative cerebral blood vessel passive mechanical behavior does not significantly change, absolute cerebral blood vessels morphometry goes through alterations that impacts blood flow delivery to the brain.

2.6 Active Cerebrovascular Tension Curve Morphology

The foundation of autoregulation resides in the circumferential smooth muscle cells lining arteries that have the mechanical ability to tighten or relax, thus constricting or dilating blood vessels. The active behavior of smooth muscle cells can be comprised of three distinct parts. First, the length-tension relationship of smooth muscle cells which corresponds to the ability cells to apply tension across various degrees of stretch. For example, there is an

optimal stretch length where a maximum of engaged cross-bridge formations (sarcomeres) within the muscle cell can generate force [228]. Variations of stretch away from this optimal length will diminish the possible muscle force response [228]. This represents the maximum possible force that can be generated by the smooth muscle cells at a particular stretch configuration. Second, is the degree of smooth muscle cell activation. While smooth muscle cells will have a homeostatic activation, their activation degree will be modulated based on physiologic signals [229]. Additionally, the homeostatic tone of smooth muscle cells are dependent on the size, and potentially age, of the blood vessel (section 2.8). Third, is the ratio of max smooth muscle cell (active) tension to passive blood vessel tension (section 2.9). Like homeostatic tone, the ratio of active to passive tension will change with blood vessel size and will dictate how much active deformation the blood vessel can experience.

To characterize the ability of human intracranial smooth muscle cells to apply circumferential tension (the length-tension relationship), measurements of activated wall tension must be separated from a passive vascular response throughout variations in pressure. In vitro pressure-inflation experiments can provide measurements of maximally constricted (active) and maximally dilated (passive) vascular tension to identify the bounds of vascular mechanical behavior. Specifically of interest for autoregulation, the mechanical behavior of intracranial vessels, such as human vertebral vessels, will need to be measured [230]. Experimentally, the in vitro vertebral vessels are first exposed to a smooth muscle cell activating solution that fully constricts the blood vessel across pressure-inflation. Then, the same blood vessels are pressure-inflated within a saline solution invoking only a passive response [230]. The subtraction of the entirely dilated curve from the maximally constricted curve provides the entire range of tension that vertebral smooth muscle cells can apply (Figure 2.4a).

Fitting of entirely dilated and completely passive stress/strain curves [230], were performed with physiologically-consistent exponential-type curves ($f(x) = ae^{bx}$). To generate the curve for normalized smooth muscle cell tension response, the data were first converted from stress/strain to tension/diameter. Using unpressurized vertebral diameter [231] (corrected for histology shrinkage [232]), pressured vertebral diameter [233], and vertebral thickness [230], unpressurized vertebral thickness is calculated from a hollow thick cylinder derivation assuming incompressibility and neglecting longitudinal strain (Equation 2.4). This allows for the circumferential strain/stress conversion (found in Equations 2.6 and 2.7) to tension/diameter. Normalization is relative to maximum active tension and homeostatic lumen radius (assumed to be at the curve peak). Once normalized, this relationship creates the length-tension relationship to characterize the maximum ability of sarcomeres to apply muscle force response in a particular stretch configuration. The following homeostatic-normalized curve for smooth muscle cell max possible tension over lumen radius is characterized as: $\bar{T_{\theta\theta SMC}} = -1.49E^{-6} * e^{12.71*\bar{r}} + 2.14E^{-2} * e^{4.25*\bar{r}}$ and is represented in Figure 2.4b. Of note, the length-tension relationship of human intracranial smooth muscle cells is asymmetric with the ability to apply tension diminishing quicker under stretch compared to constriction.

Thick-Walled Cylinder Equations:

Wall thickness calculations between unpressurized and pressurized configurations:

$$h_0 = -r_0 + \sqrt{h_d^2 + 2r_d h_d + r_0^2} \tag{2.4}$$

where x_0 and x_d are the unpressurized and pressurized configurations, respectively. h refers to thickness and r refers to lumen radius.

Mid-wall circumferential strain:

$$\epsilon_{\theta\theta} = \frac{(R_d + r_d) - (R_0 + r_0)}{(R_0 + r_0)} = \frac{\sqrt{r_d^2 + 2r_0 h_0 + h_0^2} + r_d}{2r_0 + h_0} - 1 \tag{2.5}$$

where x_0 and x_d are the unpressurized and pressurized configurations, respectively. h refers to thickness, r refers to lumen radius, and R refers to outer radius.

Mid-wall circumferential strain solved for r_d:

$$r_d = \frac{2r_0 + 2\epsilon_{\theta\theta} h_0 + 4\epsilon_{\theta\theta} r_0 + \epsilon_{\theta\theta}^2 h_0 + 2\epsilon_{\theta\theta}^2 r_0}{2\epsilon_{\theta\theta} + 2} \tag{2.6}$$

Mid-wall circumferential stress:

$$\sigma_{\theta\theta} = \frac{T_d}{R_d - r_d} \tag{2.7}$$

where T_d refers to tension in the pressurized configuration.

2.7 Cerebrovascular Passive and Maximum Active Vessel Diameter

With homeostatic-normalized passive tension (section 2.5) and homeostatic-normalized smooth muscle cell maximum active tension (section 2.6) curves characterized, the relative scaling of these relationships remains necessary. In particular, the scaling between passive and maximum active tension is dependent on homeostatic vessel radius and pressure.

The dependent variables of vessel radius and pressure for the passive vessel radius calculation were derived from data measured in human pial arteries [234]. Upon passive radius data extraction, a radius-moderated polynomial regression was calculated. The following equation for homeostatic human cerebral vessel passive radius is: $r_{passive}[\mu m] = (7.44E^{-7} * r_{homeostatic}[\mu m] - 7.88E^{-3}) * p^2[mmHg] + (8.58E^{-4} * r_{homeostatic}[\mu m] + 1.20) * p[mmHg] + (1.08 * r_{homeostatic}[\mu m] - 18.83)$ paired with the subsequent calculation for passive tension $T_{passive} = p_{homeostatic} * r_{passive}$.

The dependent variables of vessel radius and pressure for the maximum active vessel radius calculation were derived from data measured in human pial arteries [234]. Upon maximum active radius data extraction, a radius-moderated linear regression was calculated.

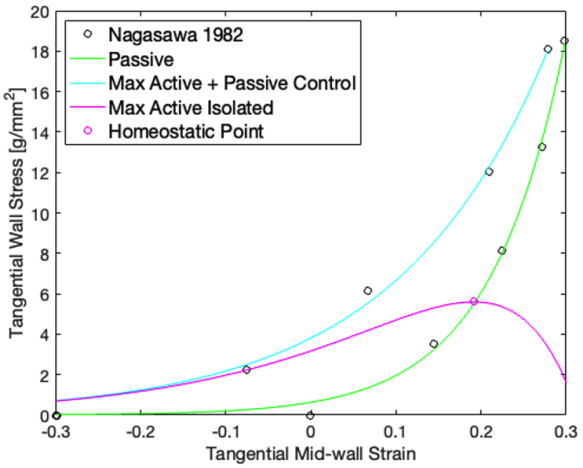

(a) Smooth muscle cell maximally activated response.

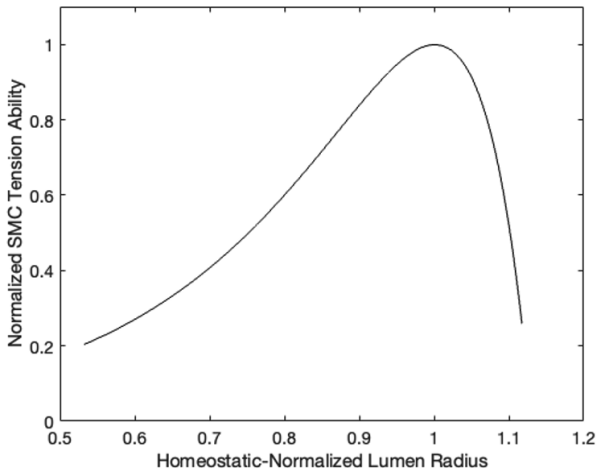

(b) SMC Curve.

Figure (2.4) a) Intracranial vertebral maximally constricted behavior, maximally dilated behavior, and isolated smooth muscle cell maximally activated response. Experimental data extracted from [230]. b) Maximum smooth muscle response relative to homeostatic lumen radius.

The following equation for homeostatic human cerebral vessel maximum active radius is: $r_{active}[\mu m] = (5.18E^{-4} * r_{homeostatic}[\mu m] + 4.87E^{-1}) * p[mmHg] + (8.41E^{-1} * r_{homeostatic}[\mu m] - 50.92)$. Together, these two equations provide the passive to maximum active tension homeostatic relationship dependent on radius and expected transmural pressure. Additionally, the absolute or relative values can be utilized depending on the application context. Importantly, when extrapolated to large blood vessels, the relationship holds reasonably well with the error for maximum active tension being 1.3% and the error for passive tension being 10.3% [230].

2.8 Active Cerebrovascular Tension Homeostatic Tone

While the maximum active to passive tension ratio in cerebrovascular arteries has established the range of possible vessel dilation and constriction, the homeostatic myogenic tone and smooth muscle cell (SMC) activation degree remain a critical aspect to characterize. The homeostatic myogenic tone in human pial arteries (lumen diameter: 200 - 1200 μm) has been clearly established as being a function of vascular radius and transmural pressure [234]. As of now, extensive myogenic tone measurements have not been taken in larger human blood

vessels, but extrapolating the linear trends of only human pial arteries would indicate that larger human blood vessels do not posses myogenic tone at homeostasis [234]. In opposition to the pial artery extrapolation, MCAs have been shown to dilate in conditions of hypoxia while maintaining relatively consistent blood pressure (negating the influence of passive vessel behavior) [235, 236]. Dilation without the influence of pressure-induced passive blood vessel behavior provides evidence that larger human cerebral blood vessels maintain some degree of myogenic tone at homeostasis. Therefore, the characterization of homeostatic tone and activation will include the combined data from human pial arteries and larger sized blood vessels.

For the large human blood vessel portion of the myogenic tone calculation, homeostatic myogenic tone ($M_{Tone} = 100 * \frac{d_{passive} - d_{homeostatic}}{d_{passive} - d_{maxActivation}}$) can be approximated from experimental data of vertebral stretch [230]. Experimental measurements of radius at passive tension and maximum active tension are interpolated at homeostatic pressure [230], and with the assumption of homeostatic vascular radius [233] and pressure [237], myogenic tone of large human vertebral vessels can be approximated as $\approx 39\%$ providing additional evidence that these vessels in fact have myogenic tone. For the small human blood vessel homeostatic myogenic tone calculation, data were extracted from pial artery experiments [234]. From these pial artery experiments, the only modification was the approximate conversion of unpressurized diameter to homeostatic diameter.

Once combined, utilizing data spanning from lumen diameter 200 - 3120 μm [234, 230], a pressure-moderated linear regression is established for lumen diameter versus homeostatic myogenic tone. The following equation for human cerebral vessel homeostatic myogenic tone is: $M_{Tone}[\%] = (-1.10E^{-5} * p[mmHg] - 1.56E^{-2}) * d_{homeostatic}[\mu m] + (2.74E^{-1} * p[mmHg] + 5.05E^{1})$. To create an internally consistent system of equations (utilizing the variables of M_{Tone}, $d_{homeostatic}$, $p_{homeostatic}$, $d_{passive}$, and d_{active}), $d_{homeostatic}$ and $p_{homeostatic}$ can both be set, while ultimately solving for $d_{passive}$ using the equations for M_{Tone} and d_{active}. $d_{passive_{alt}} = (d_{active} * M_{Tone} - 100 * d_{homeostatic})/(M_{Tone} - 100)$.

While age-related change of myogenic tone is not supported in human pial arteries [234], rat models do report age-related diminishes of myogenic tone in the MCA [238]. Human age-related changes in myogenic tone may be restricted to smaller blood vessels (100 - 400 μm diameter) where the ratio of SMCs to media area decreases with age [239]. Of note, comparisons between similarly sized rat and human blood vessel show strikingly different myogenic tones, though it appears that myogenic tone may be similar for matching artery types such as the MCA [240, 238].

2.9 Cerebrovascular Tension Scaling

Expanding upon the diameter equations of cerebrovascular vessels ($d_{passive_{alt}}, d_{active}$), relationships between passive and active circumferential tension can be formed across the vascular tree. Overall, the calculation of applied active and passive tension components is

represented from the effective pressure required to transition from one vascular diameter to another. The effective pressure calculation relies upon vascular wall assumptions, namely that collagen primarily provides tensile resistance while elastin provides equivalent tensile and compressive resistance [37]. The effective pressure required to transition from, for example, a passive vascular diameter to homeostatic diameter represents the active tension value required to overcome elastin resistance. Ultimately, expressions for circumferential tension/stress across the vascular tree can be calculated.

Starting at homeostatic diameter, the vessel wall is providing an equal and opposite force, comprised of a passive and active component, to balance transmural pressure: $T_{composite_{homeostatic}} = p_{homeostatic} * d_{homeostatic}$ (homeostatic pressure acquired from [237]). To calculate the compressive active force, applied by SMCs, required to transition from passive diameter to a smaller diameter, an equivalent pressure calculation is utilized. Specifically, the circumferential strain equation of an incompressible closed-ended cylindrical pressure vessel ($\epsilon_{\theta\theta} = \frac{pd}{4tE}(2-\upsilon)$) can be rearranged to produce an equivalent pressure force required during a diameter change. To perform the effective pressure calculation, an incremental numerical approach was utilized, due to the large diameter range calculated over, with the incremental effective pressures summed up (Equation 2.8). In this context, the effective pressure calculation was performed for both passive to homeostatic diameter and passive to maximum active diameter. Thickness at each diameter was calculated using Equation 2.4. For Young's modulus (E) in this context, the SMC active force is compressing the blood vessel from the larger passive diameter configuration to the smaller homeostatic and maximum active diameters. Since collagen fibers provide minimal resistance in non-tensile configurations, an age-related Young's modulus measured from human elastin and smooth muscle cells in thoracic and abdominal aortas will be applied ($E_{elastin}[mmHg] = 5250.4 - 22.5 * age[yr]$) [102]. The decrease in elastin modulus may be partially explained due to elastin fatigue [37] with the remodeling of functional elastin from circumferential-aligned at young age to heterogeneously-aligned in old age [38].

$$p_{effective_{homeostatic}} = \sum_{n=passive}^{homeostatic} \frac{d_{n-1} - d_n}{d_{n-1}} \frac{3Et_n}{8d_n} \tag{2.8}$$

Next, $p_{effective}$ was applied to active circumferential tension and stress components, in both the homeostatic and max active configurations, using the following equations: $T_{\theta\theta active} = p_{effective} * d_{homeostatic}$, $\sigma_{\theta\theta} = \frac{T_{\theta\theta active}}{t_{homeostatic}}$. Once active components are calculated, the difference from the composite tension value provides the passive component: $T_{homeostatic_{passive}} = T_{composite_{homeostatic}} - T_{active_{homeostatic}}$.

From here, the homeostatic circumferential tension/stress values, split into passive and active components, across the vascular tree have been established. Additionally, the range of possible circumferential tension/stress values that SMCs can apply, through the modulation of active force have been established (Figures 2.5a and 2.5b). Analytical expressions for absolute circumferential tension/stress and tension/stress active/passive ratios can be found in Table 2.4. According to these expressions, a critical point between the active and

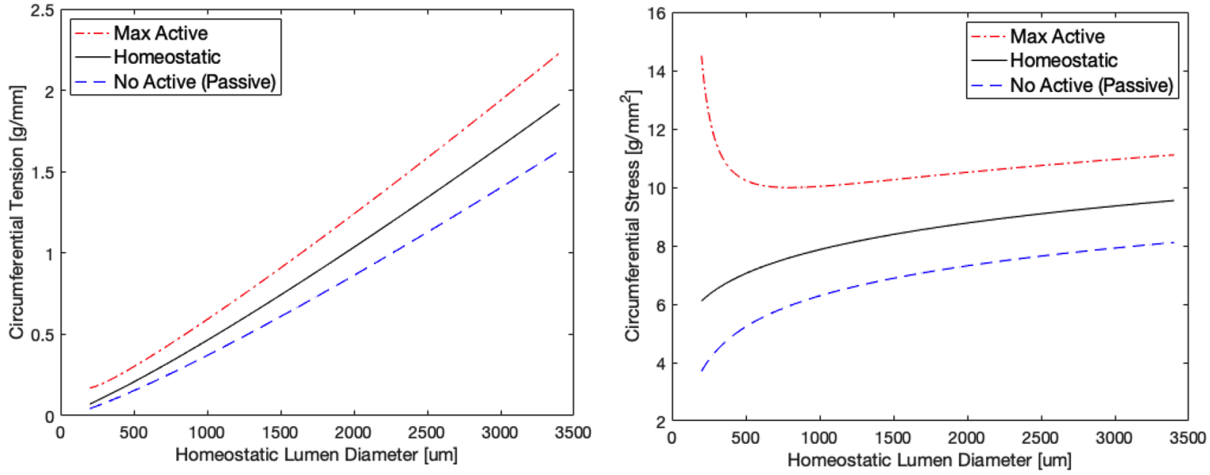

(a) Vascular circumferential tension over vascular tree

(b) Vascular circumferential stress over vascular tree

Figure (2.5) a) Vascular circumferential tension range comprising of maximum active tension (maximum active + passive), homeostatic tension (homeostatic active + passive), and no active tension (only passive). Together, these curves represent the range of possible circumferential tension values that a blood vessel, at an arbitrary diameter along the vascular tree, could experience. b) Vascular circumferential stress range comprising of maximum active stress (maximum active + passive), homeostatic stress (homeostatic active + passive), and no active stress (only passive).

passive tension/stress ratio occurs at 480 μm where, smaller than this diameter, maximum active tension ability becomes greater than passive tension ability. The role of active tension becomes more prominent at diameters below 1000 μm, while the ratio of active to passive tension remains relatively constant above 1000 μm. Specifically for human vertebral vessels, where data are minimal, maximum active (composite), passive, and maximum active (active component) stress values are within 0.75%, 45%, and -46% error, respectively, indicating at least good agreement with total vascular tension [230]. Qualitatively, data from both humans and rats indicate that the influence of active tension increases with smaller vascular diameter, matching our fitting [234, 241].

2.10 Relative Contributions of Autoregulation Mechanisms

The foundation of the overall autoregulation response is underpinned by the various contributions of the major autoregulatory mechanisms. Together, the contributions of myogenic

Vascular Circumferential Tension Fitting

$T_{\theta\theta}[\frac{g}{mm}] = a * (diameter[\mu m])^b + c$

	a	b	c
Max Active	1.75E-4	1.16	7.03E-2
Homeostatic	1.55E-4	1.16	1.69E-16
No Active (Passive)	1.11E-4	1.18	-1.67E-2

Vascular Circumferential Stress Fitting

$\sigma_{\theta\theta}[\frac{g}{mm^2}] = a * exp(b * diameter[\mu m]) + c * exp(d * diameter[\mu m])$

	a	b	c	d
Max Active	27.35	-9.02E-3	9.65	4.23E-5
Homeostatic	7.97	5.45E-5	-2.54	-1.56E-3
No Active (Passive)	6.36	7.37E-5	-3.83	-1.98E-3

Vascular Circumferential Stress and Tension Component Ratio Fittings

$\sigma_{\theta\theta_{active}}/\sigma_{\theta\theta_{passive}} = a * (diameter[\mu m])^b + c$

$T_{\theta\theta_{active}}/T_{\theta\theta_{passive}} = a * (diameter[\mu m])^b + c$

	a	b	c
Max Active	6.75E3	-1.50	3.58E-1
Homeostatic	85.02	-9.71E-1	1.47E-1

Table (2.4) Vascular circumferential tension/stress analytical fitting across homeostatic lumen diameter comprising of maximum active (maximum active + passive), homeostatic (homeostatic active + passive), and no active (only passive) configurations. Together, these curves represent the range of possible circumferential tension/stress values that a blood vessel, at an arbitrary diameter along the vascular tree, could experience. Tested and derived from data for the diameter range of 200 μm to 3400 μm at an age of 50 years old for the Young's modulus of elastin and using the equation for $r_{passive}$.

(mechanotransduction-based), metabolic (perivascular pH-based), and neurogenic mechanisms regulate the amount of active tension applied by cerebral vascular smooth muscle cells. Some of these mechanisms can be further broken down into contributing forces that can have opposite regulating effects, such as myogenic pressure-based regulation versus myogenic shear-based regulation [242, 243]. In general, metabolic and myogenic forces engage the largest changes in vascular smooth muscle cell (VSMC) activation, thus having the most potential to modify cerebral blood flow. Neurogenic activation is considered to be a more local activation of VSMCs related more to neurovascular coupling [30]. Other vascular regulation mechanisms such as baroreflex (MAP-sensitive), considered a subset of neurogenic [244], act systemically on the cardiovascular system, but can also influence cerebral SMCs directly.

While the trigger mechanisms are different for each autoregulatory mechanism, eventually the SMCs are signaled to dilate or constrict, thus modifying vascular tension and local blood flow in the vasculature. To compare all of these mechanisms across an equal footing, a first step will be to establish the bounds of which each autoregulatory mechanism can maximally modify SMC activation. The effective bounds of influence could be compared across a different metrics such as tCBF, SMC activation, active tension, or diameter range. Note that it is not trivial to convert between these metrics as scaling across them is not linear. Of these options, the bounds of SMC activation for each mechanisms represents the most consistent characteristic across diameter and age. To establish SMC activation bounds, equation 2.8 and the methods showcased in section 2.9, can be utilized to represent SMCs maximum and minimum activation limits.

To establish the maximum possible modification of flow, Poiseuille's law ($\Delta p = \frac{8\mu LQ}{\pi R^4}$) provides an approximation of expected blood flow changes in response to maximal changes in blood vessel diameter ($\Delta Q \propto \Delta R^4$). Using the maximal changes in blood vessel diameter established in section 2.7 (also representing maximal SMC activation), an approximation of maximal blood flow modifications can be established. Further, treating homeostatic diameter as the reference point, normalization for maximal dilation and compressive ranges are established (row 1 of Table 2.5). After defining the maximal blood vessel boundaries in different forms, the contribution of each autoregulatory mechanism can be referenced within this overall framework to establish relative strength.

Starting with CO_2 reactivity, to establish the bounds of autoregulatory contribution, Table 2.3 and Equation 2.1 provide the maximum changes of tCBF ($tCBF\% \in [-33.2, 92.8]$ where the first value provides tCBF percentage decreases in response to vascular compression and the second value provides tCBF percentage increases in response to vascular dilation). With normalization, the range ([-1,1]) is defined from the maximally dilated/constricted configuration to the homeostatic configuration (this does not imply symmetry). Already, based on the maximal possible tCBF changes due to vascular diameter ranges (Diameter-based Estimate), CO_2 reactivity covers nearly the entire range of possible tCBF changes, implying that CO_2 reactivity nearly has the ability to maximally activate all SMCs in the brain in both the dilatory and compressive configurations, respectively ($A \in [-1.03, .75]$). Using the data from O_2 reactivity, with smaller tCBF range $tCBF\% \in [0, 37.0]$, O_2 reactivity has less

ability to activate cerebral SMCs, with about half the ability of CO_2 reactivity in the dilatory activation, but no ability in the compressive activation ($A \in [-.54, 0]$). Of particular interest is the myogenic autoregulatory ability of SMC activation range for conditions such as acute ischemic stroke. Overall, the maximum recorded changes in tCBF in myogenic conditions (as described in section 2.2) are $tCBF\% \in [-3.2, 21]$ with higher ability in the dilatory condition. Running through the calculations to determine degree of SMC activation, this change in tCBF would imply that maximum myogenic dilatory strength comprises about one third of the possible SMC range. This suggests that cerebrovascular beds cannot be fully dilated/constricted from myogenic contributions alone, and this may extend for individual cerebral blood vessels as well. For baroreflex ability, while the mechanism of tCBF change does not actually directly influence cerebral VSMCs, the effective cerebrovascular change, actually due to cardiovascular changes, are provided for contribution reference. The bounds of baroreflex ability were established from cardiac output modifications [245] from canines with baroreceptor denervation [246]. Baroreflex activation represents an effective characterization since it doesn't actually influence cerebral autoregulatory mechanisms directly.

Regarding the neurogenic autoregulatory mechanism, comprised of sympathetic (adrenergic) and parasympathetic (cholinergic) forces [31], the primary influence of activation occurs within the typical autoregulation pressure bounds (homeostatic maintenance) [247]. Thus, only acting within the homeostatic maintenance range of autoregulation, neurogenic mechanism can only induce small flow deviations within local areas.

Beyond cerebral autoregulation, cerebrovascular reactivity [204, 217] and cardio baroreflex [248] also show healthy age-related changes while neurovascular coupling remains unmodified [204]. Specifically with cererovascular reactivity, advancing aging is associated with a diminished vasoconstriction response to hypocapnia and enhanced vasodilation response to hypercapnia [217].

	tCBF% Range	tCBF Range Normalized	d% Range	d Range Normalized	SMC Activation Range / T Range Normalized
Diameter-based Estimate (Reference)	-	$tCBF \in [-1, 1]$	$d_{vert}\% \in [-12.2, 17.2]$	$d \in [-1, 1]$	$A \in [-1, 1]$
CO_2 Reactivity	$tCBF\% \in [-33.2, 92.8]$	$tCBF \in [-0.82, 1.05]$	$d_{vert}\% \in [-9.59, 17.83]$	$d \in [-0.78, 1.04]$	$A \in [-1.03, 0.75]$
O_2 Reactivity	$tCBF\% \in [0, 37.0]$	$tCBF \in [0, 0.42]$	$d_{vert}\% \in [0, 8.19]$	$d \in [0, 0.48]$	$A \in [-0.54, 0]$
Myogenic	$tCBF\% \in [-3.2, 21]$	$tCBF \in [-0.08, 0.24]$	$d_{vert}\% \in [-0.81, 4.88]$	$d \in [-0.07, 0.28]$	$A \in [-0.33, 0.06]$
Baroreflex_{eff}	$tCBF\% \in [-2.9, 10.3]$	$tCBF \in [-0.07, 0.12]$	$d_{vert}\% \in [-0.73, 2.48]$	$d \in [-0.06, 0.14]$	$A \in [-0.18, 0.05]$

Table (2.5) Relative contribution of autoregulatory mechanisms referenced to maximal possible change as defined by limits in blood vessel diameter. All values provided are based on calculations for vertebral-sized blood vessels (3400 μm diameter). The diameter-based estimation, by definition, represents the maximum and minimum possible diameters of the blood vessel as governed by the strength limits of SMCs. The diameter-based estimate will act as the reference for all other comparisons. tCBF ranges of the diameter-based estimations are approximated using Poiseuille's law. SMC activation (represented by 'A'), is assumed to be linearly proportional to active tension values. For tCBF and diameter values, the first value in each cell represents decreases while the second value in each cell represents increases. For SMC activation, the first value in each cell represents dilatory behavior while the second value in each cell represents compressive behavior. Gray cells represent the original measures used to define the bounds of each type of autoregulatory mechanism. White cells are calculated based off of the respective gray cells for each autoregulatory mechanism.

Chapter 3

1D Blood Vessel Mathematical Formulation

3.1 Introduction

Overall for the cerebrovascular model design, a one dimensional (1D) deformable vascular network of blood vessels is coupled to a lumped parameter network to capture systemic blood flow behavior. To focus on cerebral hemodynamics, the 1D vessel network has nearly complete coverage of vessels leading from the heart to the major brain blood vessels. Further, a lumped parameter model (described in chapter 4), with multiple outlets to represent downstream cerebral vascular beds and intracranial dynamics is coupled to the 1D vascular network.

The 1D vascular network aspect of the model was chosen because deformable vessels excel at pulse wave propagation, capturing bulk fluid behavior and blood redistribution with relatively quick computation times. Additionally, there is significant flexibility in the design the vascular model facilitating the ability to rapidly-prototype arterial systems or work towards building patient-specific arterial systems.

The 1D deformable vascular network is governed by reduced-order Navier-Stokes equations where incompressible, newtonian fluid with impermeable and axisymmetric vessels is assumed (section 3.3 and 3.4). A constitutive relationship is governed by Laplace's law with the assumption of linear, elastic, isotropic blood vessel wall material properties (section 3.6). The 1D governing partial differential equations (PDEs) are solved using finite volume numerical methods and characteristic analysis to facilitate propagating pulse waves (section 3.8 and 3.9).

3.2 General Definition and Assumptions

To characterize reduced-order blood vessel area, blood velocity, and blood pressure (A, u, p) within flexible blood vessels, governing equations derived from the principles of conserva-

tion of mass and conservation of momentum are paired with a constitutive equation of the vessel wall material properties [249]. Specifically, non-linear 1D equations of blood flow and pressure are applied to impermeable and deformable tubes with the assumption of fluid incompressibility and Newtonian behavior [249, 250]. Figure 3.1 represents a generalized compliant 1D blood vessel, while Figure 3.2 represents the 1D reduced-order blood vessel.

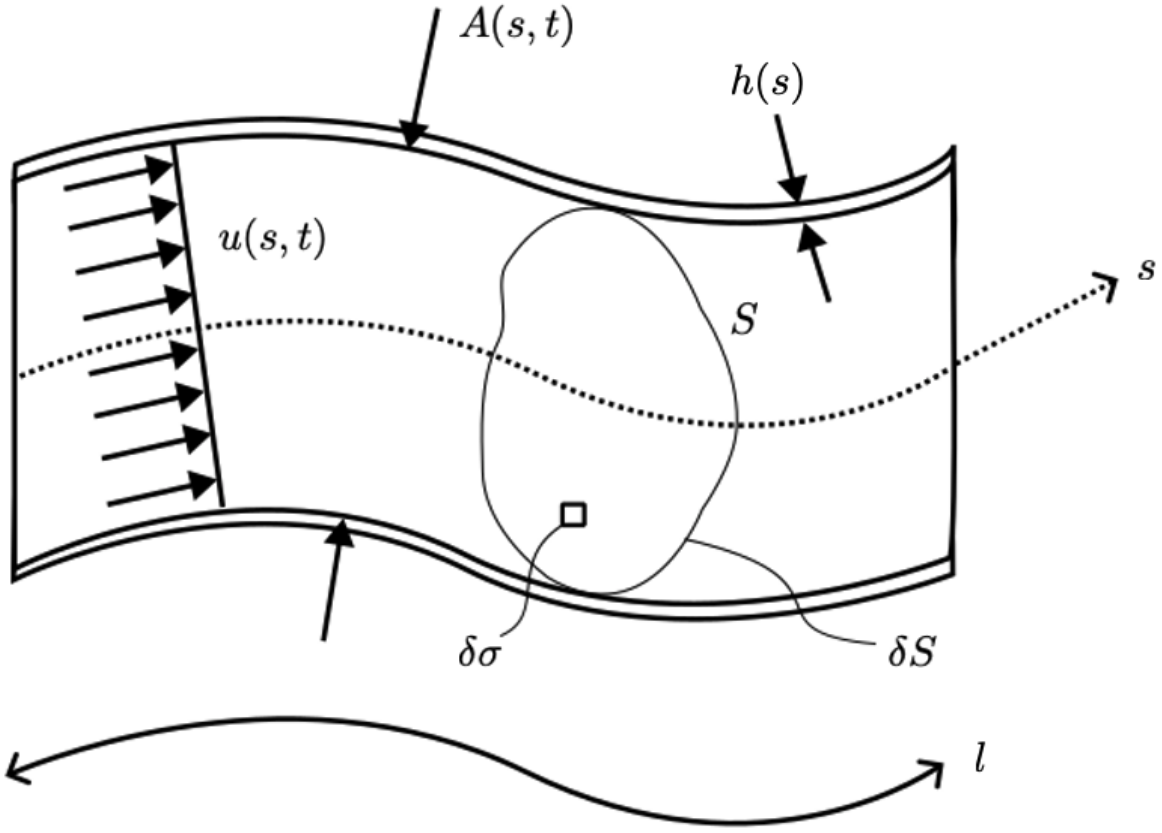

Figure (3.1) Generalized compliant 1D blood vessel representation. s represents blood vessel curvature, t represents changes in time, S represents generalized cross-section, σ represents infinitesimal area of S, u represents cross-sectional fluid velocity, A represents cross-sectional area, h represents cross-sectional thickness, and l represents length of the blood vessel. Figure recreated from [250].

Assumptions of the 1D blood vessel model include incompressibility, Newtonian fluid, constant cross-sectional material properties, uniform flow profile, and small changes in local curvature. An incompressible and Newtonian fluid implies that ρ and μ are constant. While the assumption of a uniform flow profile that neglects the viscosity of the fluid is required, the difference in momentum from this assumption is accounted for with a momentum flux correction factor (section 3.4). The assumption regarding the local curvature, s, is defined

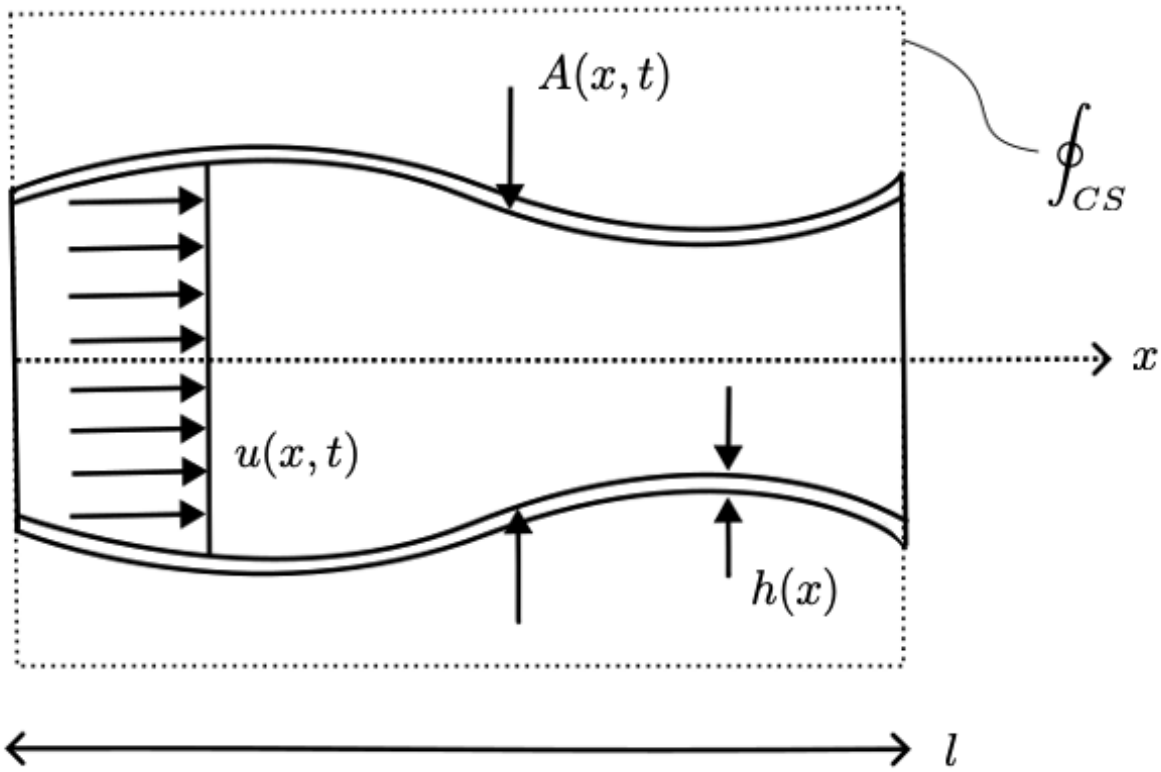

Figure (3.2) 1D reduced-order blood vessel representation. x represents the 1D-axis of the blood vessel, and $\oint_{CS}$ represents the control surface of the blood vessel. Figure recreated from [250].

such that changes are small enough everywhere such that the axial direction can be described by cartesian coordinate x. As long as there is enough grid points along the axial discretization, this can be considered a reasonable assumption.

Definition of independent variables:
$A(x,t) = \int_S d\sigma$ (area of cross-section S)
$u(x,t) = \frac{1}{A}\int_S \hat{u} d\sigma$ (average velocity over a cross section)
$p(x,t) = \frac{1}{A}\int_S \hat{p} d\sigma$ (internal pressure over cross section)
where $\hat{u}(x,\sigma,t)$, $\hat{p}(x,\sigma,t)$ are constant within the cross-section.

3.3 Conservation of Mass Formulation

Following conservation of mass principles, the following equation can be derived for the fluid within a 1D vessels (following from Figure 3.2) [249]. This formulation assumes no seepage

through the side walls.

$$\rho\frac{dV(t)}{dt} + \rho Q(l,t) - \rho Q(0,t) = 0$$

$$V(t) = \int_0^l A(x,t)dx$$

$$Q(l,t) - Q(0,t) = \int_0^l \frac{\partial Q(x,t)}{\partial x}dx$$

$$\rho\frac{d}{dt}\int_0^l A(x,t)dx + \rho\int_0^l \frac{\partial Q(x,t)}{\partial x}dx = 0$$

Assume that l is independent of time:

$$\rho\int_0^l \left[\frac{\partial A(x,t)}{\partial t} + \frac{\partial Q(x,t)}{\partial x}\right]dx = 0$$

l is not specified, thus making the control volume arbitrary.

1D Conservation of Mass:

$$\frac{\partial A(x,t)}{\partial t} + \frac{\partial Q(x,t)}{\partial x} = \frac{\partial A(x,t)}{\partial t} + \frac{\partial [u(x,t)A(x,t)]}{\partial x} = 0$$

3.4 Conservation of Momentum Formulation

Following conservation of momentum principles, the following equation can be derived for the fluid within a 1D vessels (following from Figure 3.2) [249]. This formulation assumes no flux through the side walls.

$$\sum \vec{F}_{CV} = \frac{d}{dt}\int_{CV} \rho\vec{v}\,dV + \oint_{CS} \rho\vec{v}(\vec{v}\cdot\vec{n})dA$$

x-direction:

$$\sum F_x = \frac{d}{dt}\int_{CV} \rho u dV + \oint_{CS} \rho u(\vec{v}\cdot\vec{n})dA$$

To simplify the inlet and outlet ($\vec{v} \parallel \vec{n}$), 1D principles assumptions include that v is constant across the inlet/outlet surface, and that ρ is constant (Figure 3.3).
Inlet: $\vec{v}\cdot\vec{n} = -v$
Outlet: $\vec{v}\cdot\vec{n} = v$

$$\oint_{CS} \rho \overrightarrow{v}(\overrightarrow{v} \cdot \overrightarrow{n}) dA = \sum_{out} \rho v A \overrightarrow{v} - \sum_{in} \rho v A \overrightarrow{v}$$

$$\sum \overrightarrow{F}_{CV} = \sum \overrightarrow{F}_{body} + \sum \overrightarrow{F}_{pressure} + \sum \overrightarrow{F}_{viscous} + \sum \overrightarrow{F}_{other}$$

$$\sum F_x^{LHS} = \sum F_{xgravity} + \sum F_{xpressure} + \sum F_{xviscous} + \sum F_{xother}$$

$$F_x^{LHS} = \frac{d}{dt} \int_0^l \rho u(x,t) A(x,t) dx + [\alpha(l,t) \rho Q(l,t) u(l,t)]_{x=l} - [\alpha(0,t) \rho Q(0,t) u(0,t)]_{x=0}$$

Due to the constant inlet/outlet velocity simplification (a consequence of the reduced-order averaging), $\alpha(x,t)$ represents a momentum flux correction factor to compensate for the difference in momentum expected from a typical flow profile and estimated blunt case [251]. Since blood vessels actually have parabolic flow profiles, the alpha term here acts as a momentum flux correction term to approximate for the momentum difference lost between the real flow profiles of the vessel and the blunt approximation. The Table 3.1 provides typical values for α.

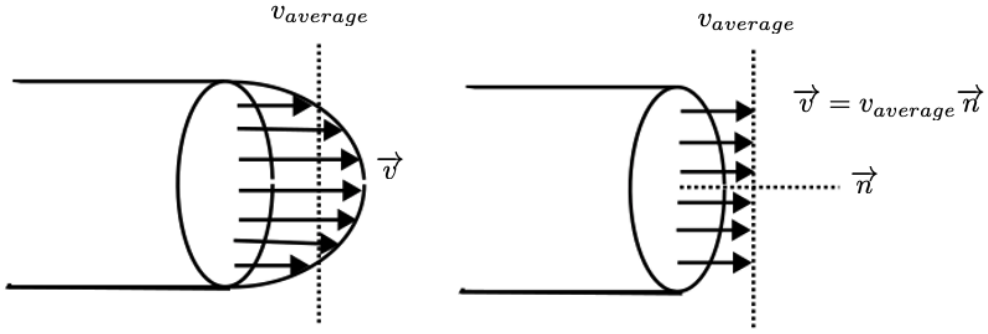

(a) Non-uniform outlet. (b) Equivalent 1D outlet.

Figure (3.3) Flow profile assumption of 1D blood vessel formulation.

$$\alpha = \frac{MF_{actual}}{MF_{equivalent}} = \frac{1}{A} \int_A \left(\frac{u}{v_{avg}} \right)^2 dA \geq 1$$

$$\alpha(x,t) = \frac{\int_S \hat{u}^2(x,\sigma,t) d\sigma}{A(x,t) u^2(x,t)}$$

The left side of the following equation represents the true momentum flux, while the right side of the equation represents the 1D approximation of momentum flux [251].

Flow Profile Type:	α
1D Uniform Flow (Plug Flow)	1
1D Fully Developed Laminar Pipe Flow (Poiseuille Flow)	4/3
1D Fully Developed Turbulent Pipe Flow	≈ 1.02

Table (3.1) Values of momentum flux correction factor α

$$\int_{A_C} \rho \overrightarrow{v}(\overrightarrow{v} \cdot \overrightarrow{n}) dA_C = \alpha \dot{m} \overrightarrow{v}_{avg}$$

$$\alpha = \frac{\int_{A_C} \rho v(\overrightarrow{v} \cdot \overrightarrow{n}) dA_C}{\dot{m} v_{avg}} = \frac{\int_{A_C} v(\overrightarrow{v} \cdot \overrightarrow{n}) dA_C}{v_{avg} A_C v_{avg}} = \frac{1}{A_C} \int_{A_C} \left(\frac{v}{v_{avg}} \right)^2 dA_c \geq 1$$

For the right hand side of the 1D momentum force balance, the pressure force (gauge pressure), side wall pressure force, and friction force per unit length (viscous component) are considered. The side wall pressure force and frictional force are further covered in subsections 3.4.1 and 3.4.2, respectively.

$$F_x^{RHS} = [p(x,t)A(x,t)]_{x=0} - [p(x,t)A(x,t)]_{x=l} + \int_0^l \int_{\partial S} \hat{p}(x,\sigma,t) n_x ds dx + \int_0^l f dx$$

Subsection 3.4.1 concludes that the side wall pressure force can be represented as: $\int_0^l \int_{\partial S} \hat{p}(x,\sigma,t) n_x ds dx = \int_0^l p(x,t) \frac{\partial A(x,t)}{\partial x} dx$

Combining the left hand side and right hand side of the conservation of momentum formulation ($F_x^{LHS} = F_x^{RHS}$) results in the following:

$$\frac{d}{dt} \int_{x_1}^{x_2} \rho u(x,t) A(x,t) dx + [\alpha(x_2,t) \rho Q(x_2,t) u(x_2,t)]_{x=x_2} - [\alpha(x_1,t) \rho Q(x_1,t) u(x_1,t)]_{x=x_1}$$

$$= [p(x_1,t)A(x_1,t)]_{x=x_1} - [p(x_2,t)A(x_2,t)]_{x=x_2} + \int_{x_1}^{x_2} p(x,t) \frac{\partial A(x,t)}{\partial x} dx + \int_{x_1}^{x_2} f dx$$

Further simplified:

$$\frac{d}{dt} \int_{x_1}^{x_2} \rho u(x,t) A(x,t) dx + \int_{x_1}^{x_2} \frac{\partial [\alpha(x,t) \rho Q(x,t) u(x,t)]}{\partial x} dx = - \int_{x_1}^{x_2} \frac{\partial [p(x,t) A(x,t)]}{\partial x} dx$$

$$+ \int_{x_1}^{x_2} p(x,t) \frac{\partial A(x,t)}{\partial x} dx + \int_{x_1}^{x_2} f dx$$

$$\frac{-\partial[p(x,t)A(x,t)]}{\partial x} = -p(x,t)\frac{\partial A(x,t)}{\partial x} - A(x,t)\frac{\partial p(x,t)}{\partial x}$$

Assume that ρ is constant and l, also known as $(x_2 - x_1)$, is independent of time:

$$\rho \int_{x_1}^{x_2} \left\{ \rho \frac{\partial Q(x,t)}{\partial t} + \rho \frac{\partial[\alpha(x,t)Q(x,t)u(x,t)]}{\partial x} \right\} dx$$
$$= \int_{x_1}^{x_2} \left\{ \frac{-\partial[p(x,t)A(x,t)]}{\partial x} + p(x)\frac{\partial A(x,t)}{\partial x} + f \right\} dx$$

This formulation is satisfied for arbitrary length l, also known as $(x_2 - x_1)$, and thus can be satisfied when integrads are equal.

1D Conservation of Momentum (in Q, A format):

$$\frac{\partial Q(x,t)}{\partial t} + \frac{\partial[\alpha(x,t)Q(x,t)u(x,t)]}{\partial x} = \frac{-A(x,t)}{\rho}\frac{\partial p(x,t)}{\partial x} + \frac{f}{\rho}$$

The Q, A format is not the ideal form for the 1D momentum equation, and the preference is to write it in terms of (A,u). This can be achieved through the further manipulations of partial derivatives [249]. Once a flow profile is assumed for α, it becomes constant value for these derivations.

$$\frac{\partial(uA)}{\partial t} + \frac{\partial(\alpha A u^2)}{\partial x} + \frac{A}{\rho}\frac{\partial p}{\partial x} = \frac{f}{\rho}$$

$$A\frac{\partial u}{\partial t} + u\frac{\partial A}{\partial t} + \cancel{Au^2\frac{\partial \alpha}{\partial x}} + \alpha u^2\frac{\partial A}{\partial x} + 2u\alpha A\frac{\partial u}{\partial x} + \frac{A}{\rho}\frac{\partial p}{\partial x} = \frac{f}{\rho}$$

$$\frac{\partial u}{\partial t} + \frac{u}{A}\frac{\partial A}{\partial t} + \frac{\alpha u^2}{A}\frac{\partial A}{\partial x} + 2u\alpha\frac{\partial u}{\partial x} + \frac{1}{\rho}\frac{\partial p}{\partial x} = \frac{f}{\rho A}$$

Utilizing the conservation of mass:

$$\frac{u}{A}\frac{\partial A}{\partial t} = -\frac{\partial(uA)}{\partial x}\frac{u}{A} = -\frac{u^2}{A}\frac{\partial A}{\partial x} - u\frac{\partial u}{\partial x}$$

$$\frac{\partial u}{\partial t} - \frac{u^2}{A}\frac{\partial A}{\partial x} - u\frac{\partial u}{\partial x} + \frac{\alpha u^2}{A}\frac{\partial A}{\partial x} + 2u\alpha\frac{\partial u}{\partial x} + \frac{1}{\rho}\frac{\partial p}{\partial x} = \frac{f}{\rho A}$$

1D Conservation of Momentum (in u, A format):

$$\frac{\partial u(x,t)}{\partial t} + (\alpha - 1)\frac{u^2(x,t)}{A(x,t)}\frac{\partial A(x,t)}{\partial x} + (2\alpha - 1)u(x,t)\frac{\partial u(x,t)}{\partial x} + \frac{1}{\rho}\frac{\partial p(x,t)}{\partial x} = \frac{f}{\rho A(x,t)}$$

3.4.1 Axisymmetric Side-Wall Pressure Force

To determine if an axisymmetric blood vessel is an appropriate assumption for 1D modeling, the following section compares non-symmetric and axisymmetric side-wall pressure force [252].

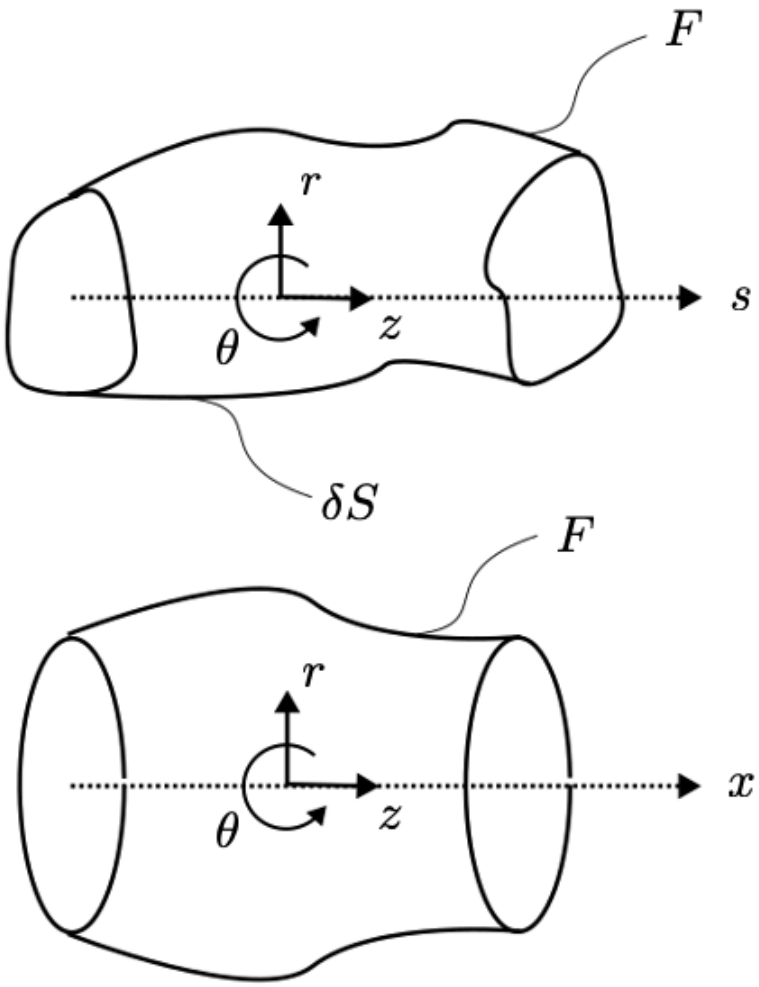

Figure (3.4) Axisymmetric assumption for a 1D blood vessel representation. Top part of the figure represents a generalized blood vessel, while the bottom part of the figure represents an axisymmetric blood vessel

The definition of axisymmetric means that the blood vessel geometry has no dependence on θ (figure 3.4). The surface representation of axisymmetric: $F(r, z) = r - f(z) = 0$ which simplifies to $f(z) = r$. This surface is saying that anywhere along z, there is a consistent radius value in all θ directions. r can change along z, but it does so in an axisymmetric

fashion. An example equation includes one for a cylinder: $x^2 + y^2 = R^2$ or for a cone: $x^2 + y^2 = a^2z^2$ or an expanding cylinder: $f(z) = az + b = r$. f(z) becomes more complex for blood vessels.

$$\nabla F(r,z) = \frac{\partial F}{\partial r}\hat{e}_r + \frac{\partial F}{\partial z}\hat{e}_z = \hat{e}_r - \frac{\partial F}{\partial z}\hat{e}_z$$

Looking at the inward normal:

$$\hat{n} = \frac{-\nabla F}{||\nabla F||} = \frac{1}{\sqrt{1+(\frac{\partial f}{\partial z})^2}}\left(-\hat{e}_r + \frac{\partial f}{\partial z}\hat{e}_z\right)$$

$$f_p(\overrightarrow{x}) = \int_0^l \int_{\partial S} \hat{p}(x,\sigma,t) n_x ds dz = \int_0^l \int_{\partial S} \hat{p}\left[\frac{1}{\sqrt{1+(\frac{\partial f}{\partial z})^2}}\left(-\hat{e}_r + \frac{\partial f}{\partial z}\hat{e}_z\right)\right] ds dZ$$

The first term in the following equation can be dropped out because the integral is only considering the z direction.

$$f_p(\overrightarrow{x}) = \int_0^l \int_{\partial S} \hat{p}\left[\frac{-1}{\sqrt{1+(\frac{\partial f}{\partial z})^2}}\hat{e}_r\right] ds dZ + \int_0^l \int_{\partial S} \hat{p}\left[\frac{\frac{\partial f}{\partial z}}{\sqrt{1+(\frac{\partial f}{\partial z})^2}}\hat{e}_z\right] ds dZ$$

$$f_{p_z}(\overrightarrow{x}) = \int_0^l \hat{p}\frac{\frac{\partial f}{\partial z}}{\sqrt{1+(\frac{\partial f}{\partial z})^2}} \int_{\partial S} ds dZ$$

Utilizing an example surface with a circular cross-section such as: $A_s(z) = \pi r^2 = \pi f^2(z)$ where $\frac{\partial A_s}{\partial z} = 2\pi f(z)\frac{\partial f}{\partial z}$, substitutions can be made.

$$f_{p_z}(\overrightarrow{x}) = \int_0^l p\frac{2\pi f(z)\frac{\partial f}{\partial z}}{\sqrt{1+(\frac{\partial f}{\partial z})^2}} dZ = \int_0^l \frac{p\frac{\partial A_s}{\partial z}}{\sqrt{1+(\frac{\partial f}{\partial z})^2}} dZ$$

If $\frac{\partial f}{\partial z} << 1$, then $\sqrt{1+(\frac{\partial f}{\partial z})^2} \approx 1$

$$f_{p_z}(\overrightarrow{x}) = \int_0^l p(x,t)\frac{\partial A(x,t)}{\partial x} dx$$

In summary, the axisymmetric assumption is valid if radius does not change rapidly relative to changes in local curvature. In conditions such as an aneurysm, this assumption wouldn't apply.

3.4.2 Frictional Term

To examine the frictional term in more detail, shear stress from the flow profile is considered.

$$f(x,t) = 2\pi r\tau = 2\pi r\mu \frac{du}{dr}\bigg|_{r=R}$$

To characterize the flow profile (how blood velocity changes with radius) within the blood vessel, the following form is assumed [253]:

$$u(r,x,t) = \frac{\gamma+2}{\gamma} u_{avg}(x,t)\left[1-\left(\frac{r}{R}\right)^{\gamma}\right]$$

$$f(x,t) = 2\pi R\mu\left(\frac{\gamma+2}{\gamma}\right) u\left(\frac{-\gamma}{R}\right) = -2\pi\mu(\gamma+2)u$$

In a typical blood vessel flow profile, $\gamma = 2$ and $\alpha = 4/3$. In a blunt profile, $\gamma = 9$ and $\alpha \approx 1.1$ (Table 3.1). Note that α becomes constant once a flow profile is assumed. A conversion between γ and α can be based on profile assumptions:

$$\gamma = \frac{2-\alpha}{\alpha-1}$$

$$f = \frac{-2\alpha}{\alpha-1}\mu\pi u$$

Importing the frictional term into the 1D conservation of momentum equation leads to:

$$\frac{\partial(uA)}{\partial t} + \frac{\partial(\alpha A u^2)}{\partial x} + \frac{A}{\rho}\frac{\partial p}{\partial x} = \frac{f}{\rho} = \frac{-2\alpha}{\alpha-1}\frac{\mu\pi u}{\rho}$$

Expand and divide by A:

$$\frac{\partial u}{\partial t} + \frac{u}{A}\frac{\partial A}{\partial t} + \alpha\frac{u^2}{A}\frac{\partial A}{\partial x} + \alpha\frac{\partial u^2}{\partial x} + \frac{1}{\rho}\frac{\partial p}{\partial x} = \frac{-2\alpha}{\alpha-1}\frac{\mu\pi u}{\rho A}$$

Modifying the conservation of mass equations allows for further substitution:

$$\frac{u}{A}\left(\frac{\partial A}{\partial t} + \frac{\partial(uA)}{\partial x}\right) = 0$$

$$\frac{u}{A}\frac{\partial A}{\partial t} = -\frac{u^2}{A}\frac{\partial A}{\partial x} - u\frac{\partial u}{\partial x}$$

Inserting the conservation of mass substitution back into the conservation of momentum equation:

$$\frac{\partial u}{\partial t} - \frac{u^2}{A}\frac{\partial A}{\partial x} - u\frac{\partial u}{\partial x} + \alpha\frac{u^2}{A}\frac{\partial A}{\partial x} + \alpha\frac{\partial u^2}{\partial x} + \frac{1}{\rho}\frac{\partial p}{\partial x} = \frac{-2\alpha}{\alpha-1}\frac{\mu\pi u}{\rho A}$$

1D Conservation of Momentum (in u, A format):

$$\frac{\partial u}{\partial t} + (\alpha - 1)\frac{u^2}{A}\frac{\partial A}{\partial x} + (2\alpha - 1)u\frac{\partial u}{\partial x} + \frac{1}{\rho}\frac{\partial p}{\partial x} = \frac{-2\alpha}{\alpha - 1}\frac{\mu\pi u}{\rho A}$$

3.5 Conservation of Mass and Momentum Equations - Alternative Navier-Stokes Derivation

The 1D governing equations of mass and momentum can alternatively be derived from 3D Navier-Stokes [254]. Similar assumptions of constant blood viscosity (independent of vessel radius), incompressibility, homogeneous, laminar, and Newtonian fluid of low Reynolds's number in an axisymmetric geometry are applied. Cylindrical coordinates (r, θ, x) with x along the local vessel axial direction are utilized. Velocity in circumferential direction is assumed to be zero (to eliminate dependency on θ within model).

Conservation of Mass:

$$\cancel{\frac{\partial \rho}{\partial t}} + \frac{1}{r}\frac{\partial}{\partial r}(\rho r u_r) + \cancel{\frac{1}{r}\frac{\partial(\rho u_\theta)}{\partial \theta}} + \frac{\partial(\rho u_x)}{\partial x} = 0$$

$$\frac{1}{r}\frac{\partial}{\partial r}(r u_r) + \frac{\partial(u_x)}{\partial x} = 0$$

Navier-Stokes θ-Direction:
Axisymmetric flow means that $0 = 0$.

Navier-Stokes r-Direction:

$$\rho\left(\frac{\partial u_r}{\partial t} + u_r\frac{\partial u_r}{\partial r} + \cancel{\frac{u_\theta}{r}\frac{\partial u_r}{\partial \theta}} + u_x\frac{\partial u_r}{\partial x} - \cancel{\frac{u_\theta^2}{r}}\right)$$
$$= -\frac{\partial p}{\partial r} + \mu\left[\frac{1}{r}\frac{\partial}{\partial r}\left(r\frac{\partial u_r}{\partial r}\right) + \cancel{\frac{1}{r^2}\frac{\partial^2 u_r}{\partial \theta^2}} + \frac{\partial^2 u_r}{\partial x^2} - \frac{u_r}{r^2} - \cancel{\frac{2}{r^2}\frac{\partial u_\theta}{\partial \theta}}\right] + \cancel{\rho g_r}$$

Further simplified:

$$\frac{\partial u_r}{\partial t} + u_r\frac{\partial u_r}{\partial r} + u_x\frac{\partial u_r}{\partial x} + \frac{1}{\rho}\frac{\partial p}{\partial r} = \upsilon\left[\frac{\partial^2 u_r}{\partial r^2} + \frac{1}{r}\frac{\partial u_r}{\partial r} + \frac{\partial^2 u_r}{\partial x^2} - \frac{u_r}{r^2}\right]$$

Navier-Stokes x-Direction:

$$\rho\left(\frac{\partial u_x}{\partial t} + u_r\frac{\partial u_x}{\partial r} + \cancel{\frac{u_\theta}{r}\frac{\partial u_x}{\partial \theta}} + u_x\frac{\partial u_x}{\partial x}\right) =$$

$$-\frac{\partial p}{\partial x}+\mu\left[\frac{1}{r}\frac{\partial}{\partial r}\left(r\frac{\partial u_x}{\partial r}\right)+\frac{1}{r^2}\cancel{\frac{\partial^2 u_x}{\partial \theta^2}}+\frac{\partial^2 u_x}{\partial x^2}\right]+\cancel{\rho g_x}$$

Further simplified:

$$\frac{\partial u_x}{\partial t}+u_r\frac{\partial u_x}{\partial r}+u_x\frac{\partial u_x}{\partial x}+\frac{1}{\rho}\frac{\partial p}{\partial x}=\upsilon\left[\frac{\partial^2 u_x}{\partial r^2}+\frac{1}{r}\frac{\partial u_x}{\partial r}+\frac{\partial^2 u_x}{\partial x^2}\right]$$

Dimensional Analysis:
The purpose of dimensional analysis is to get non-dimensional representation terms such that:

$r=\bar{R}r^*$ where $\bar{R}$ represents characteristic inner vessel radius

$x=\lambda x^*$ where λ represents characteristic length. $\lambda=\frac{\bar{R}U_{x_o}}{U_{r_o}}$ where U_{x_o} represents characteristic axial velocities and U_{r_o} represents characteristic radial velocities

$$u_x=U_{x_o}u_x^*$$

$$u_r=U_{r_o}u_r^*$$

$$t=\frac{\lambda}{U_{x_o}}t^*$$

$$p=\rho U_{x_o}^2 p^*$$

Navier-Stokes r-Direction Non-Dimensional:

$$-\frac{\partial p^*}{\partial r^*}=\frac{U_{r_o}^2}{U_{x_o}^2}\left[\frac{\partial u_r^*}{\partial t^*}+u_r^*\frac{\partial u_r^*}{\partial r^*}+u_x^*\frac{\partial u_r^*}{\partial x^*}-\frac{\upsilon}{\bar{R}U_{r_o}}\left(\frac{\partial^2 u_r^*}{\partial r^{*2}}+\frac{1}{r^*}\frac{\partial u_r^*}{\partial r^*}-\frac{u_r^*}{r^{*2}}+\frac{U_{r_o}^2}{U_{x_o}^2}\frac{\partial^2 u_r^*}{\partial x^{*2}}\right)\right]$$

Assume that the radial velocity is small compared to axial velocity: $\left(\frac{U_{r_o}^2}{U_{x_o}^2}\to 0\right)$

Assume that pressure is constant across the vessel cross-section meaning that r^* is independent of x^* $\left(\frac{\partial p^*}{\partial r^*}=0\right)$

Navier-Stokes x-Direction Non-Dimensional:

$$\frac{\partial u_x^*}{\partial t^*}+u_r^*\frac{\partial u_x^*}{\partial r^*}+u_x^*\frac{\partial u_x^*}{\partial x^*}+\frac{\partial p^*}{\partial x^*}=\frac{\lambda\upsilon}{U_{x_o}\bar{R}^2}\left[\frac{\partial^2 u_x^*}{\partial r^{*2}}+\frac{1}{r^*}\frac{\partial u_x^*}{\partial r^*}+\frac{U_{r_o}^2}{U_{x_o}^2}\frac{\partial^2 u_x^*}{\partial x^{*2}}\right]$$

Conservation of Mass:

$$\frac{\partial(r^* u_x^*)}{\partial x^*} + \frac{\partial(r^* u_r^*)}{\partial r^*} = 0$$

Conservation of Momentum:

$$\frac{\partial(r^* u_x^*)}{\partial t^*} + \frac{\partial(r^* u_r^* u_x^*)}{\partial r^*} + \frac{\partial(r^* u_x^{*2})}{\partial x^*} + \frac{\partial(r^* p^*)}{\partial x^*} = \frac{\lambda \upsilon}{U_{x_o} \bar{R}^2} \frac{\partial}{\partial r^*} \left(r^* \frac{\partial u_x^*}{\partial r^*} \right)$$

3.6 Pressure-Area Relationship and Distensibility (Constitutive Relationship)

In the 1D blood vessel formulation, and in order to have pulse wave formation, distensibility of the blood vessel wall is required. Essentially, distensibility means the capability of the blood vessel wall to dilate or compress. The distensibility of the blood vessel wall originates with the media mechanical properties.

The governing equations of mass and momentum conservation provide two equations with three unknowns: $A(x,t), u(x,t), p(x,t)$. The constitutive relationship closes the system by defining relationship between sectional pressure and area. $p = fn(A, x, t)$. Specifically, distensibility is defined as: $D = \frac{1}{A(x,t)} \frac{dA(x,t)}{dp(x,t)}$.

3.6.1 First p-A Model: Linear Constant

When designing the pressure-area relationship, the most basic definition is a linear pressure-area constitutive relation that utilizes a constant γ. In this formulation, A_0 references to a reference area at p_0.

$$(p - p_0) = \gamma(A - A_0)$$

3.6.2 Second p-A Model: Laplace Law

Increasing in complexity and widely used in cerebrovascular modeling, a tube law based on Laplace Law can be utilized for the constitutive relationship [255, 253, 256]. This tube law is built considering an indefinitely long open-ended cylinder (circular lumen) at all internal pressures with an arterial wall that is a linear, elastic, isotropic material with a small thickness compared to the vessel radius ($h << R$) (Figure 3.5). Structural arterial properties are considered constant at a section. External forces applied to the arterial wall are reduced to stresses in the circumferential direction. Laplace Law is valid when $\frac{t}{r} << \frac{\Delta p}{p_0}$ which starts to break down in small vessels below $500 \mu m$.

Following a balance of forces:

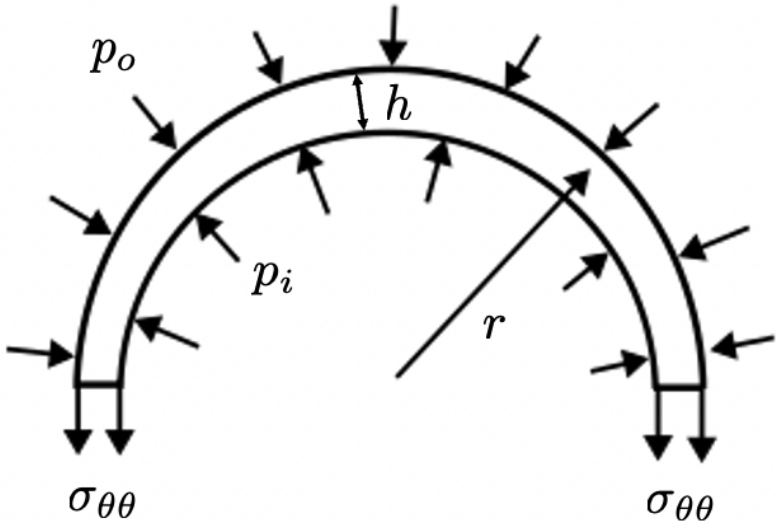

Figure (3.5) Cross-sectional representation of a linear, elastic, isotropic blood vessel with thickness for the application of Laplace Law.

$$2\sigma_\theta(hL) = (p_i - p_o)(2\pi rL)$$

$$\sigma_{\theta\theta} = \frac{(p_i - p_o)r_i}{h}, \sigma_{rr} = -(p_i - p_o)$$

Further, for an indefinitely long open-ended cylinder, ϵ_z is zero (plane strain). Assuming constant thickness, there is not an ϵ_r. The assumption of incompressibility applies to Poisson's ratio ($\upsilon = \frac{1}{2}$). Assume that radial stress is negligible compared to the hoop and axial stresses ($\sigma_{\theta\theta} >> \sigma_{rr}$) since $\frac{r_i}{h} >> 1$.

By the definition of circumferential stress in an indefinitely long open-ended cylinder:

$$\sigma_{\theta\theta} = \frac{E}{1 - \upsilon^2}(\epsilon_{\theta\theta} + \upsilon\epsilon_{zz})$$

where E is Young's modulus.

$$\epsilon_{\theta\theta} = \frac{2\pi r_i - 2\pi r_o}{2\pi r_o}$$

ϵ_{zz} not considered in indefinitely long cylinder and $\epsilon_{rr} = 0$ with constant thickness approximation.

Combining the equations for circumferential stress and strain:

$$\frac{(p_i - p_o)r_i}{h} = \frac{E}{1-\upsilon^2}\frac{2\pi r_i - 2\pi r_o}{2\pi r_o}$$

To match with the conservation of mass and momentum governing equations, radius is substituted into area:

$$A_i = \pi r_i^2, A_o = \pi r_o^2$$

$$\Delta p = \frac{h}{r_i}\frac{E}{1-\upsilon^2}\frac{r_i - r_o}{r_o} = \frac{hE\sqrt{\pi}}{\sqrt{A}}\frac{1}{1-\upsilon^2}\frac{\frac{\sqrt{A}}{\sqrt{\pi}} - \frac{\sqrt{A_o}}{\sqrt{\pi}}}{\frac{\sqrt{A_o}}{\sqrt{\pi}}}$$

$$\Delta p = \frac{hE\sqrt{\pi}}{1-\upsilon^2}\left(\frac{1}{\sqrt{A_o}} - \frac{1}{\sqrt{A}}\right)$$

Laplace Law Constitutive Equation:

$$p = p_o + \frac{hE\sqrt{\pi}}{1-\upsilon^2}\left(\frac{1}{\sqrt{A_o}} - \frac{1}{\sqrt{A}}\right) \tag{3.1}$$

Occasionally, it is convenient to assume that $\frac{r_i}{r_o} = 1$ in the denominator term [250], then:

$$\Delta p = \frac{h}{r_o}\frac{E}{1-\upsilon^2}\frac{r_i - r_o}{r_o} = \frac{hE\sqrt{\pi}}{1-\upsilon^2}\left(\frac{\sqrt{A} - \sqrt{A_o}}{A_o}\right)$$

3.6.3 Third p-A Model: Viscoelastic Voigt Model

More complex constitutive equations with viscoelastic properties, such as the Voigt-style model (Figure 3.6), have also been used to study cerebrovascular pulse wave modeling [257].

The force balance within the Voigt-style model is: $F = \mu u + \eta \dot{u}$ with initial condition $u(0) = 0$.

$$\sigma_{\theta\theta} = \frac{1}{1-\upsilon^2}[\mu\epsilon_{\theta\theta} + \eta\dot{\epsilon}_{\theta\theta}]$$

$$\sigma_{\theta\theta} = \frac{(p_i - p_o)r_i}{h}, \epsilon_{\theta\theta} = \frac{2\pi r_i - 2\pi r_o}{2\pi r_o}, \dot{\epsilon}_{\theta\theta} = \frac{\partial r_i}{\partial t}\frac{1}{r_o}$$

$$\frac{(p_i - p_o)r_i}{h} = \frac{1}{1-\upsilon^2}\left[\mu\frac{r_i - r_o}{r_o} + \eta\frac{\partial r_i}{\partial t}\frac{1}{r_o}\right]$$

$$\frac{\partial r_i}{\partial t}\frac{1}{r_o} = \frac{\partial(\frac{\sqrt{A_i}}{\sqrt{\pi}})}{\partial t}\frac{\sqrt{\pi}}{\sqrt{A_o}} = \frac{1}{2}\frac{1}{\sqrt{A_i}\sqrt{A_o}}\frac{\partial A_i}{\partial t}$$

$$\frac{(p_i - p_o)\sqrt{A_i}}{\sqrt{\pi}h} = \frac{1}{1-\upsilon^2}\left[\mu\left(\frac{\sqrt{A_i} - \sqrt{A_o}}{\sqrt{A_0}}\right) + \eta\left(\frac{1}{2}\frac{1}{\sqrt{A_i}\sqrt{A_o}}\frac{\partial A_i}{\partial t}\right)\right]$$

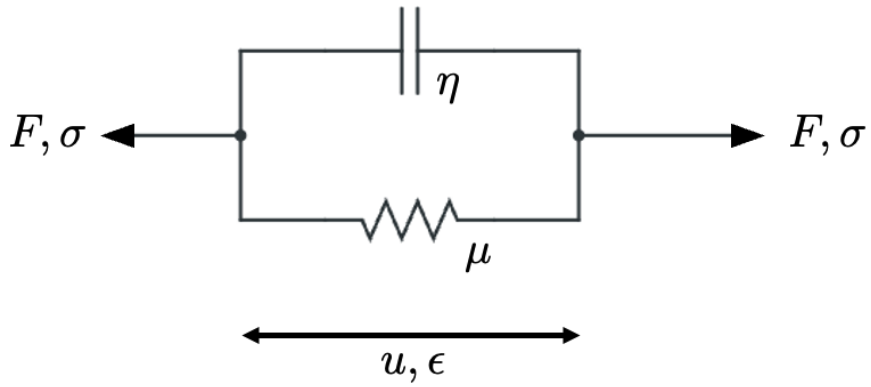

Figure (3.6) Viscoelastic Voigt model constitutive equation representation.

Viscoelastic Voigt Model Constitutive Equation:

$$\Delta p = \frac{\sqrt{\pi}h\mu}{1-\upsilon^2}\left(\frac{1}{\sqrt{A_o}} - \frac{1}{\sqrt{A}}\right) + \frac{\sqrt{\pi}h\eta}{2(1-\upsilon^2)}\left(\frac{1}{A_i\sqrt{A_o}}\right)\frac{\partial A_i}{\partial t}$$

In this final representation, the first term represents the elastic portion of the equation (Young's modulus) and the second term represents the viscous portion of the equation (wall viscosity).

3.6.4 Fourth p-A Model: Viscoelastic Kevin Body Model

An alternative form of the viscoelastic constitutive equation is the Kevin Body model (Figure 3.7) [258, 21].The model is composed of Kelvin-Voight solid and spring in series. The linear spring is defined such that instantaneously a deformation is proportional to the load $F = \mu u$. The dashpot is defined such that a velocity proportional to the load is produced at any instant $F = \eta\dot{u}$.

There are four governing equations for this setup:
1) $u = u_1 + u_1'$
2) $F = F_e + F_v$
3) $F_e = \mu_e u$
4) $F_v = \eta\dot{u}_1 = \mu_v u_1'$

Steady version:

$$F = \mu_e u + \mu_v u_1' = (\mu_e + \mu_v)u - \mu_v u_1$$

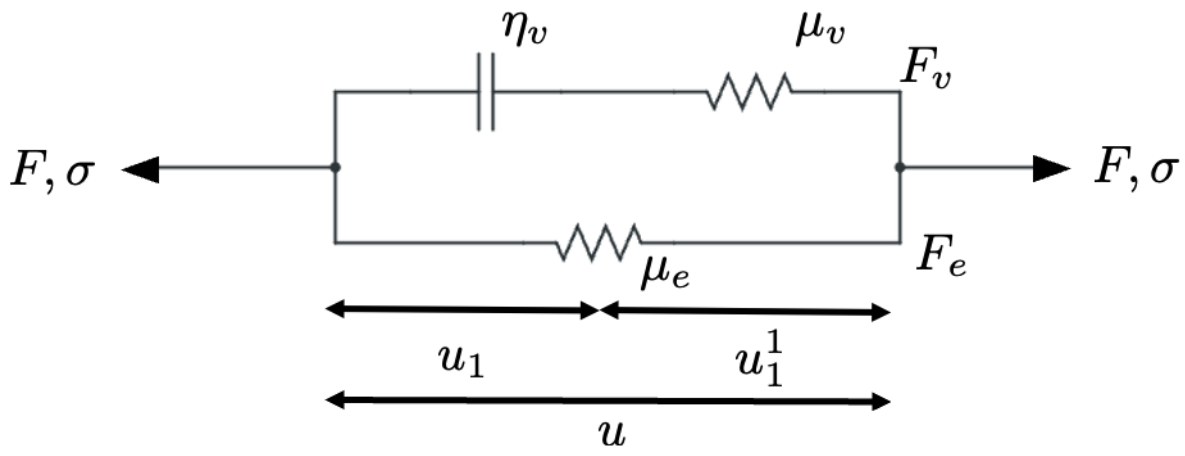

Figure (3.7) Viscoelastic Kelvin Body model constitutive equation representation.

Time-dependent version:

$$F + \frac{\eta}{\mu_v}\dot{F} = (\mu_e + \mu_v)u - \mu_v u_1 + \frac{\eta}{\mu_v}(\mu_e - \mu_v)\dot{u} - \eta\dot{u}_1$$

1D representation:

$$F + \frac{\eta}{\mu_v}\dot{F} = \mu_e u + \eta(1 + \frac{\mu_e}{\mu_v})\dot{u}$$

is equivalent to $F + \tau_\epsilon \dot{F} = E_R(u + \tau_\sigma \dot{u})$ where $\tau_\epsilon = \frac{\eta}{\mu_v}$ (the relaxation time for constant strain), $\tau_\sigma = \frac{\eta}{\mu_e}(1 - \frac{\mu_e}{\mu_v})$ (the relaxation time for constant stress), and $E_R = \mu_e$.

3D representation:

$$\sigma_{\theta\theta} + \tau_e \dot{\sigma}_{\theta\theta} = \frac{E_R}{1 - \upsilon^2}(\epsilon_{\theta\theta} + \tau_\theta \dot{\epsilon}_{\theta\theta})$$

$$\sigma_{\theta\theta} = \frac{(p_i - p_o)r_i}{h}, \dot{\sigma}_{\theta\theta} = \frac{\partial(p_i r_i)}{\partial t}\frac{1}{h}$$

$$\epsilon_{\theta\theta} = \frac{r_i - r_o}{r_o} = \frac{\sqrt{A_i} - \sqrt{A_o}}{\sqrt{A_o}}, \dot{\epsilon}_{\theta\theta} = \frac{1}{2}\frac{1}{\sqrt{A_i}\sqrt{A_o}}\frac{\partial A_i}{\partial t}$$

$$\frac{(p_i - p_o)r_i}{h} + \tau_\epsilon \frac{\partial(p_i r_i)}{\partial t}\frac{1}{h} = \frac{\mu_e}{1 - \upsilon^2}\left[\left(\frac{\sqrt{A_i} - \sqrt{A_o}}{\sqrt{A_o}}\right) + \tau_\theta\left(\frac{1}{2}\frac{1}{\sqrt{A_i}\sqrt{A_o}}\frac{\partial A_i}{\partial t}\right)\right]$$

$$(p_i - p_o) + \frac{\tau_\epsilon}{\sqrt{A_i}}\frac{\partial(p_i\sqrt{A_i})}{\partial t} = \frac{\sqrt{\pi}h\mu_e}{1 - \upsilon^2}\left(\frac{\sqrt{A_i} - \sqrt{A_o}}{\sqrt{A_i}\sqrt{A_o}} + \frac{\tau_\theta}{2A_i\sqrt{A_o}}\frac{\partial A_i}{\partial t}\right)$$

Viscoelastic Kevin Body Constitutive Equation:

$$\Delta p + \tau_\epsilon \frac{\partial p_i}{\partial t} = \frac{\sqrt{\pi} h \mu_e}{1-\upsilon^2}\left(\frac{1}{\sqrt{A_o}} - \frac{1}{\sqrt{A_i}}\right) + \left(\frac{\tau_\sigma \sqrt{\pi} h \mu_e}{2A_i\sqrt{A_o}(1-\upsilon^2)} - \frac{p_i \tau_\epsilon}{2A_i}\right)\frac{\partial A_i}{\partial t}$$

3.7 Conservative versus Non-Conservative Governing Equation Form

When solving a series of hyperbolic partial differential equations (PDEs) numerically, the form of the equation matters. Specifically, equation forms can be classified as conservative or non-conservative. Mathematically, conservative and non-conservative expressions are the same, but they are non-equivalent in discrete form and are selectively used depending on the solving methods. For example, numerical finite volume methods require the use of a conservative scheme (Section 3.8) while characteristic analysis requires the non-conservative form (Section 3.9). With a numerical analysis, non-conservative form could lead to a reasonable, but incorrect solution. With a characteristic analysis, the use of the non-conservative scheme allows for the calculation of characteristic variables along the boundary conditions [259, 260]. Below are the various conservative and non-conservative forms of the conservation of mass and momentum 1D governing equations.

Conservation of Mass Conservative Form Q,A:

$$\frac{\partial A}{\partial t} + \frac{\partial Q}{\partial x} = 0$$

Conservation of Momentum Conservative Form Q,A:

$$\frac{\partial Q}{\partial t} + \alpha \frac{\partial}{\partial x}\left(\frac{Q^2}{A}\right) + \frac{A}{\rho}\frac{\partial P}{\partial x} = \frac{f}{\rho}$$

Conservation of Mass Non-conservative Form Q,A:

$$\frac{\partial A}{\partial t} + \frac{\partial Q}{\partial x} = 0$$

Conservation of Momentum Non-conservative Form Q,A:

$$\frac{\partial Q}{\partial t} + \frac{2\alpha Q}{A}\frac{\partial Q}{\partial x} - \frac{\alpha Q^2}{A^2}\frac{\partial A}{\partial x} + \frac{A}{\rho}\frac{\partial P}{\partial x} = \frac{f}{\rho}$$

Conservation of Mass Conservative Form u,A:

$$\frac{\partial A}{\partial t} + \frac{\partial (uA)}{\partial x} = 0 \tag{3.2}$$

Conservation of Momentum Conservative Form u,A:

$$\frac{\partial(uA)}{\partial t} + \alpha\frac{\partial(u^2A)}{\partial x} + \frac{A}{\rho}\frac{\partial P}{\partial x} = \frac{f}{\rho}$$

$$\frac{\partial u}{\partial t} + (\alpha-1)\frac{u^2}{A}\frac{\partial A}{\partial x} + (2\alpha-1)u\frac{\partial u}{\partial x} + \frac{1}{\rho}\frac{\partial p}{\partial x} = \frac{-2\alpha}{\alpha-1}\frac{\mu\pi u}{\rho A}$$

For the conservative form, it is helpful to make some assumptions regarding the value of α. For the LHS, $\alpha \approx 1$, while for the RHS, $\alpha = 1 + \epsilon$. To put the value of α in context, the majority of blood vessels have blunt flow profiles so α is close to 1.

$$\frac{\partial u}{\partial t} + \frac{\partial\left(\frac{1}{2}u^2 + \frac{p}{\rho}\right)}{\partial x} = \frac{-2\alpha}{\alpha-1}\frac{\mu\pi u}{\rho A} \tag{3.3}$$

Conservation of Mass Non-conservative Form u,A:

$$\frac{\partial A}{\partial t} + u\frac{\partial A}{\partial x} + A\frac{\partial u}{\partial x} = 0 \tag{3.4}$$

Conservation of Momentum Non-conservative Form u,A:

$$\frac{\partial u}{\partial t} + (\alpha-1)\frac{u^2}{A}\frac{\partial A}{\partial x} + (2\alpha-1)u\frac{\partial u}{\partial x} + \frac{1}{\rho}\frac{\partial P}{\partial x} = \frac{f}{\rho A}$$

$$\frac{\partial u}{\partial t} + (\alpha-1)\frac{u^2}{A}\frac{\partial A}{\partial x} + (2\alpha-1)u\frac{\partial u}{\partial x} + \frac{1}{\rho}\frac{\partial p}{\partial x} = \frac{-2\alpha}{\alpha-1}\frac{\mu\pi u}{\rho A} \tag{3.5}$$

3.8 1D Governing Equation Solve - Finite Volume Methods

In solving the 1D governing PDEs (Equations 3.1, 3.2 and 3.3) for the unknown variables of velocity, area, and pressure (u, A, p), finite volume numerical methods provides an appropriate solution. The advantages of finite volume methods include unstructured meshes, conservative discretization, and, importantly, strong compatibility with pulse wave calculations [253, 261].

In terms of discretization, solving methods will incorporate a combination of the second order accurate finite volume method for space discretization and explicit Adams-Bashforth scheme for time integration (Equations 3.6, 3.7, 3.8, and Figure 3.8). The second order accuracy of the finite volume method refers to the accuracy of discretization from the Taylor series expansion. Ultimately, the combination of a space discretization and time integration is considered a predictor-corrector method. Predictor-corrector methods first take values already known and extrapolate them, then use a corrector equation to correct the solution. Finite volume characteristics method computes intermediate solutions of $(u, A, p)_{i\pm1/2}$ in

a predictor stage along the cell walls using a characteristic analysis. An explicit Adams-Bashforth time integrator recovers the solution in a corrector stage (Forward Euler is used for the first time step).

To maintain numerical stability throughout the solve, the use of the Courant-Friedrichs-Lewy (CFL) condition is necessary:

$$C = \frac{u\Delta t}{\Delta x} \leq C_{max}$$

For an explicit solve, $C_{max} = 1$, where u is the magnitude of the blood velocity.

Time Integration Steps: Two-Step Adams-Bashforth:

$$y_{n+2} = y_{n+1} + \frac{3}{2}\Delta t f(t_{n+1}, y_{n+1}) - \frac{1}{2}\Delta t f(t_n, y_n)$$

Discretized Conservation of Mass:

$$\frac{A_i^{n+2} - A_i^{n+1}}{\Delta t} + \frac{3}{2}\left[\frac{(uA)_{i+1/2}^{n+1} - (uA)_{i-1/2}^{n+1}}{\Delta x}\right] - \frac{1}{2}\left[\frac{(uA)_{i+1/2}^{n} - (uA)_{i-1/2}^{n}}{\Delta x}\right] = 0 \tag{3.6}$$

Discretized Conservation of Momentum:

$$\begin{aligned}\frac{u_i^{n+2} - u_i^{n+1}}{\Delta t} + \frac{3}{2}&\left[\frac{\left[\frac{1}{2}(u_{i+1/2}^{n+1})^2 + \frac{(p_{i+1/2}^{n+1})}{\rho}\right] - \left[\frac{1}{2}(u_{i-1/2}^{n+1})^2 + \frac{(p_{i-1/2}^{n+1})}{\rho}\right]}{\Delta x}\right] \\ -\frac{1}{2}&\left[\frac{\left[\frac{1}{2}(u_{i+1/2}^{n})^2 + \frac{(p_{i+1/2}^{n})}{\rho}\right] - \left[\frac{1}{2}(u_{i-1/2}^{n})^2 + \frac{(p_{i-1/2}^{n})}{\rho}\right]}{\Delta x}\right] = \\ &\frac{3}{2}\left[\left(\frac{-2\alpha}{\alpha - 1}\right)\frac{\mu\pi u_i^{n+1}}{\rho A_i^{n+1}}\right] - \frac{1}{2}\left[\left(\frac{-2\alpha}{\alpha - 1}\right)\frac{\mu\pi u_i^{n}}{\rho A_i^{n}}\right]\end{aligned} \tag{3.7}$$

Discretized Constitutive Equation:

$$p_i^{n+2} = p_o + \frac{hE\sqrt{\pi}}{(1 - \upsilon^2)}\left(\frac{1}{\sqrt{A_o}} - \frac{1}{\sqrt{A_i^{n+2}}}\right) \tag{3.8}$$

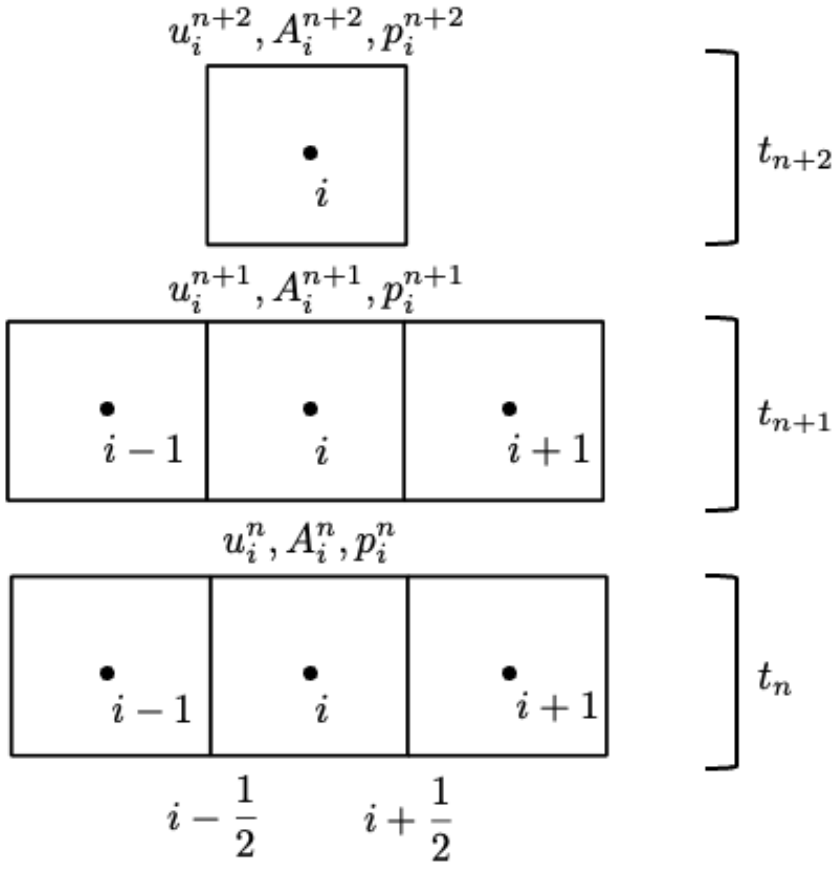

Figure (3.8) Framework for a 2nd order finite volume and adams-bashforth discretization scheme. i refers to spatial discretization while t refers to temporal discretization.

3.9 Pulse Wave Formulation - Characteristic Analysis

In solving for the boundary conditions of a hyperbolic PDE system, a characteristic analysis provides an appropriate solution by separating propagating waves into incoming and outgoing waves [253, 254]. Characteristic analysis is used for solving hyperbolic systems in the context of wave transfer (hyperbolic PDE systems with initial values are also known as the Riemann problem). Specifically, a characteristic analysis reduces the PDEs to a family of ordinary differential equations (ODEs) on some suitable hypersurface. This hypersurface is a series of curves along which the PDE becomes an ODE. The ODE can ultimately be solved along these curves. Importantly, the non-conservative form of the governing equations (Equations 3.1, 3.4 and 3.5) are used for characteristic analysis.

To begin the characteristic analysis, it is ideal to get the governing equations in a stan-

dardized format. The typical characteristic 1D conservative form is:

$$\frac{\partial \bar{u}}{\partial t} + \frac{\partial}{\partial x}[\bar{F}(\bar{u})] = \bar{S}(\bar{u})$$

The typical characteristic 1D non-conservative quasi-linear form is as follows:

$$\frac{\partial \bar{u}}{\partial t} + \bar{H}(\bar{u})\frac{\partial \bar{u}}{\partial x} = \bar{S}(\bar{u}) \tag{3.9}$$

where $\bar{H}(\bar{u}) = \frac{\partial \bar{F}}{\partial \bar{u}}$ represents the jacobian.

1st Order Hyberbolic Classification:

$\frac{\partial \bar{u}}{\partial t} + \bar{H}(\bar{u})\frac{\partial \bar{u}}{\partial x} = \bar{S}(\bar{u})$ is hyperbolic if there is a matrix function $\bar{P}$ such that

$$\bar{P}\bar{H}\bar{P^{-1}} = \Lambda(t,x) = \begin{pmatrix} \lambda_1(t,x) & ... & 0 \\ ... & ... & ... \\ 0 & ... & \lambda_d(t,x) \end{pmatrix}$$

is diagonal with real eigenvalues and the matrix norms of $\bar{P}$ and $\bar{P^{-1}}$ are bounded in x and t for $x \in \mathbb{R}, t \geq 0$.

Characteristic Analysis:

Starting from the u,A non-conservative governing equations:

$$\frac{\partial A}{\partial t} + u\frac{\partial A}{\partial x} + A\frac{\partial u}{\partial x} = 0$$

$$\frac{\partial u}{\partial t} + (\alpha - 1)\frac{u^2}{A}\frac{\partial A}{\partial x} + (2\alpha - 1)u\frac{\partial u}{\partial x} + \frac{1}{\rho}\frac{\partial P}{\partial x} = \frac{f}{\rho A}$$

For the LHS, $\alpha \approx 1$, while for the RHS, $\alpha = 1 + \epsilon$.

$$p_i = p_o + \frac{hE\sqrt{\pi}}{1 - \upsilon^2}(\frac{1}{\sqrt{A_o}} - \frac{1}{\sqrt{A}}) = p_o + p_{elastic}$$

For simplifications:

$$\beta(x) = \frac{hE\sqrt{\pi}}{1 - \upsilon^2}$$

$$\frac{\partial p}{\partial x} = \frac{\partial p_o}{\partial x} + \frac{\partial p_{elastic}}{\partial x} = \cancel{\frac{\partial p_o}{\partial x}} + \frac{\partial p_{elastic}}{\partial \beta}\cancel{\frac{\partial \beta}{\partial x}} + \frac{\partial p_{elastic}}{\partial A_o}\cancel{\frac{\partial A_o}{\partial x}} + \frac{\partial p_{elastic}}{\partial A}\frac{\partial A}{\partial x} = \frac{\partial p_{elastic}}{\partial A}\frac{\partial A}{\partial x}$$

Put conservation of mass and conservation of momentum into matrix form:

$$\frac{\partial A}{\partial t} + u\frac{\partial A}{\partial x} + A\frac{\partial u}{\partial x} = 0$$

$$\frac{\partial u}{\partial t} + u\frac{\partial u}{\partial x} + \frac{1}{\rho}\frac{\partial p_{elastic}}{\partial A}\frac{\partial A}{\partial x} = \left(\frac{-2\alpha}{\alpha - 1}\right)\frac{\mu\pi u}{\rho A}$$

In conforming to Equation 3.9, $\bar{U} = \begin{pmatrix} A \\ u \end{pmatrix}$, $\bar{H} = \begin{pmatrix} u & A \\ \frac{1}{\rho}\frac{\partial p_e}{\partial A} & u \end{pmatrix}$, $\bar{S} = \begin{pmatrix} 0 \\ \left(\frac{-2\alpha}{\alpha-1}\right)\frac{\mu\pi u}{\rho A} \end{pmatrix}$

$$\frac{\partial \begin{pmatrix} A \\ u \end{pmatrix}}{\partial t} + \begin{pmatrix} u & A \\ \frac{1}{\rho}\frac{\partial p_{elastic}}{\partial A} & u \end{pmatrix}\frac{\partial \begin{pmatrix} A \\ u \end{pmatrix}}{\partial x} = \begin{pmatrix} 0 \\ \left(\frac{-2\alpha}{\alpha-1}\right)\frac{\mu\pi u}{\rho A} \end{pmatrix}$$

Focus on the eigenvalues of $\bar{H}(\bar{U})$:

$$\left|\begin{pmatrix} u-\lambda & A \\ \frac{1}{\rho}\frac{\partial p_{elastic}}{\partial A} & u-\lambda \end{pmatrix}\right| = (u-\lambda)(u-\lambda) - \frac{A}{\rho}\frac{\partial p_{elastic}}{\partial A}$$

$$= (u-\lambda)(u-\lambda) - \frac{A}{\rho}\frac{\beta}{2A^{3/2}} = (u-\lambda)(u-\lambda) - \frac{\beta}{2\rho\sqrt{A}} = 0$$

$$\lambda = u \pm \sqrt{\frac{\beta}{2\ \rho\sqrt{A}}} = u \pm c$$

where c represents the pulse wave speed of the system.

$\lambda_{forward} = \lambda_f = u + c, \lambda_{backward} = \lambda_b = u - c$

With distinct eigenvalues in $\bar{H}$, there exists a set of right and left eigenvectors such that:

$$\bar{L}\bar{H} = \bar{\Lambda}\bar{L}$$

$$\bar{H} = \bar{L}^{-1}\bar{\Lambda}\bar{L}$$

$\bar{L} = \delta \begin{pmatrix} \frac{c}{A} & 1 \\ \frac{-c}{A} & 1 \end{pmatrix}$ where δ is an arbitrary scaling factor

$$\bar{\Lambda} = \begin{pmatrix} \lambda_f & 0 \\ 0 & \lambda_b \end{pmatrix}$$

Multiply Equation 3.9 by the left eigenvector $\bar{L}$.

$$\bar{L}\frac{\partial \bar{U}}{\partial t} + \bar{L}\bar{H}\frac{\partial \bar{U}}{\partial x} = \bar{L}\bar{S}$$

$$\bar{L}\frac{\partial \bar{U}}{\partial t} + \bar{\Lambda}\bar{L}\frac{\partial \bar{U}}{\partial x} = \bar{L}\bar{S}$$

Introduce a change of variables based on a characteristic or Riemann-type analysis:

$\frac{\partial \bar{W}}{\partial \bar{U}} = \bar{L}$ where $\bar{W} = \begin{pmatrix} W_f \\ W_b \end{pmatrix}$

After the substitution:

$$\frac{\partial \bar{W}}{\partial t} + \bar{\Lambda}\frac{\partial \bar{W}}{\partial x} = \bar{L}\bar{S}$$

Using the definition of a material derivative:

$$\frac{D\bar{W}(\hat{x}(t),t)}{Dt} = \frac{\partial \bar{W}}{\partial t} + \frac{\partial \hat{x}}{\partial t}\bar{I}\nabla\bar{W} = \frac{\partial \bar{W}}{\partial t} + \frac{\partial \hat{x}}{\partial t}\bar{I}\frac{\partial \bar{W}}{\partial \hat{x}} = \frac{\partial \bar{W}}{\partial t}$$

Choose a characteristic path such that: $\bar{\Lambda} = \frac{\partial \hat{x}}{\partial t}\bar{I}$

This implies that: $C_f : \frac{\partial \hat{x}_f}{\partial t} = \lambda_f$ and $C_b : \frac{\partial \hat{x}_b}{\partial t} = \lambda_b$ (Figure 3.9).

$$\frac{\partial \bar{W}}{\partial \bar{U}} = \bar{L}, \partial\bar{W} = \partial\bar{U}\bar{L}$$

$$\partial \begin{pmatrix} W_f \\ W_b \end{pmatrix} = \partial \begin{pmatrix} A \\ u \end{pmatrix} \delta \begin{pmatrix} \frac{c}{A} & 1 \\ \frac{-c}{A} & 1 \end{pmatrix}$$

$$W_f = \int_{A_o}^{A} \frac{\delta c}{A} dA + \int_{u_o}^{u} \delta du = \delta\left(u - u_o + \int_{A_o}^{A} \frac{c}{A} dA\right)$$

$$W_b = \int_{A_o}^{A} \frac{-\delta c}{A} dA + \int_{u_o}^{u} \delta du = \delta\left(u - u_o - \int_{A_o}^{A} \frac{c}{A} dA\right)$$

The characteristic variables are calculated as:

$$W_{f,b} = \delta\left(u - u_o \pm 4\left(\sqrt{\frac{\beta}{2\rho\sqrt{A}}} - \sqrt{\frac{\beta}{2\rho\sqrt{A_o}}}\right)\right) \tag{3.10}$$

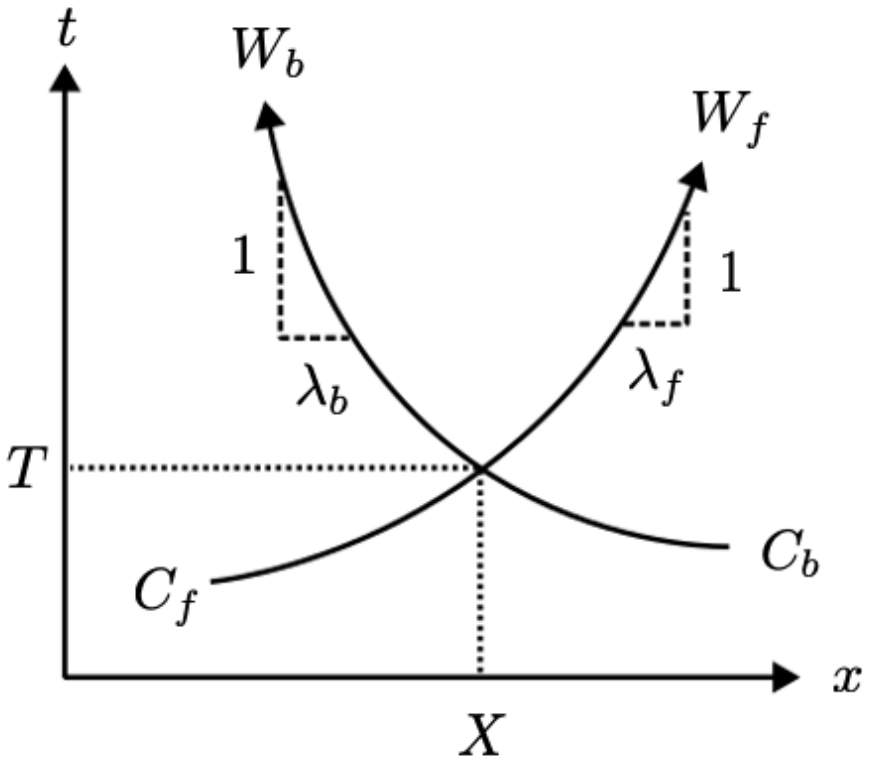

Figure (3.9) These are two characteristic paths, C_f and C_b, along which W_f and W_b propogate at speeds of λ_f and λ_b. These values change due to viscous dissipation and spatial variations of external pressure, wall distensibility, and reference luminal area.

Importantly, $W_{f,b}$ should be calculated at cell edges for proper wave propagation. Through the use of linear extrapolation, $W_{f,b}$ on $i = \pm\frac{1}{2}$ is calculated (Figure 3.10):

$$W_{f_{i-\frac{1}{2}}} = \frac{-3}{2}(W_{f_{i-2}} - W_{f_{i-1}}) + W_{f_{i-2}}$$

$$W_{b_{i-\frac{1}{2}}} = \frac{1}{2}(W_{b_i} - W_{b_{i+1}}) + W_{b_i}$$

$$W_{f,b_{i-\frac{1}{2}}} = u_{i-\frac{1}{2}} \pm 4\left(\sqrt{\frac{\beta}{2\rho\sqrt{A_{i-\frac{1}{2}}}}} - \sqrt{\frac{\beta}{2\rho\sqrt{A_{o_{i-\frac{1}{2}}}}}}\right) \tag{3.11}$$

$$W_{f_{i-\frac{1}{2}}} + W_{b_{i-\frac{1}{2}}} = 2u_{i-\frac{1}{2}}$$

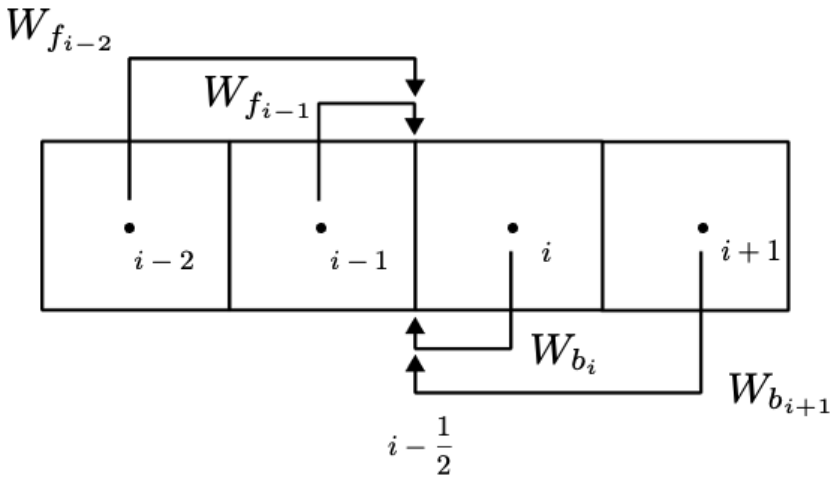

Figure (3.10) Linear extrapolation of the characteristic analysis solution to calculate the forward and backward waves in between the numerical cells.

$$p_{i-\frac{1}{2}} = p_o + \frac{hE\sqrt{\pi}}{1-\upsilon^2}\left(\frac{1}{\sqrt{A_o}} - \frac{1}{\sqrt{A_{i-\frac{1}{2}}}}\right)$$

3.10 1D Anatomical Structure Design

The design of the 1D vascular network portion of the model, is to cover all of the blood vessels from the heart leading up to the major brain blood vessels and include vessels relevant for appropriate pulse wave mechanics. The vessels included in the vascular network, identified by an ID number, are as follows: ascending aorta (1, 2), descending aorta (4, 8), brachiocephalic (3), subclavian (7, 9), brachial (15, 16), common carotid (5, 6), internal carotid (11, 12, 18, 21, 38, 39), external carotid (10, 13), vertebral (14, 17, 44, 45), basilar (22, 35, 34), posterior communicating (19, 20), anterior communicating (31), middle cerebral (23, 24), anterior cerebral (25, 26, 29, 30), posterior cerebral (27, 28, 32, 33), ophthalmic (36, 37), posterior inferior cerebellar (42, 43), anterior inferior cerebellar (41), and superior cerebellar (40) artery. The visual assembly of blood vessels, with according ID labels, is visualized in Figure 3.11 [253]. Terminal branches with three-element Windkessel models are marked with filled circles (coupling is described in section 3.11.3). Terminal branches with autoregulation models are labeled with an open circle (coupling is described in chapter 4). The reference morphological condition of the blood vessels (area, length parameters) are from a reference

point of zero transmural pressure. The unpressurized condition parameters are provided in Table 5.1.

3.11 Junction Coupling and Inlet/Outlet Boundary Conditions

Throughout the 1D vascular network, each vessel segment and terminal branch must have defined boundary conditions. Section 3.11.1 describes 1D vessel junction boundary conditions, section 3.11.2 describes the single inlet boundary condition at the aortic valve, and sections 3.11.3 and 3.11.4 cover the boundary conditions at terminal outlets. At the inlet boundary condition, flow rate ($Q_{in}(t)$) is prescribed, while terminal pressure (P_e) is determined at each terminal outlet. 1D segment junctions utilize conservation laws to maintain compatibility at each boundary.

3.11.1 1D Vessel Segment Junction Coupling Boundary Conditions

At vessel segment junctions, to obtain proper interface conditions, constant characteristic variables at each junction (x3 equations), conservation of mass (x1 equation), and conservation of total pressure (x2 equations) are enforced [249]. In total, these boundary conditions result in six equations with six unknown quantities (A_{parent}, u_{parent}, $A_{daughter1}$, $u_{daughter1}$, $A_{daughter2}$, and $u_{daughter2}$) to determine how flow splits across vessel segments.

Characteristic equations for each junction (1 forward characteristic and 2 backward characteristics) derived from Equation 3.10:

$$W_{f_{parent}} = \left(u_{parent} + 4 \left(\sqrt{\frac{\beta_{parent}}{2\rho\sqrt{A_{parent}}}} - \sqrt{\frac{\beta_{parent}}{2\rho\sqrt{A_{o_{parent}}}}} \right) \right)$$

$$W_{b_{daughter1}} = \left(u_{daughter1} - 4 \left(\sqrt{\frac{\beta_{daughter1}}{2\rho\sqrt{A_{daughter1}}}} - \sqrt{\frac{\beta_{daughter1}}{2\rho\sqrt{A_{o_{daughter1}}}}} \right) \right)$$

$$W_{b_{daughter2}} = \left(u_{daughter2} - 4 \left(\sqrt{\frac{\beta_{daughter2}}{2\rho\sqrt{A_{daughter2}}}} - \sqrt{\frac{\beta_{daughter2}}{2\rho\sqrt{A_{o_{daughter2}}}}} \right) \right)$$

$W_{f_{parent}}$, $W_{b_{daughter1}}$, and $W_{b_{daughter2}}$ are constant and determined from the last time step.

Flow rate balance equation derived from conservation of mass:

$$A_{parent}u_{parent} = A_{daughter1}u_{daughter1} + A_{daughter2}u_{daughter2}$$

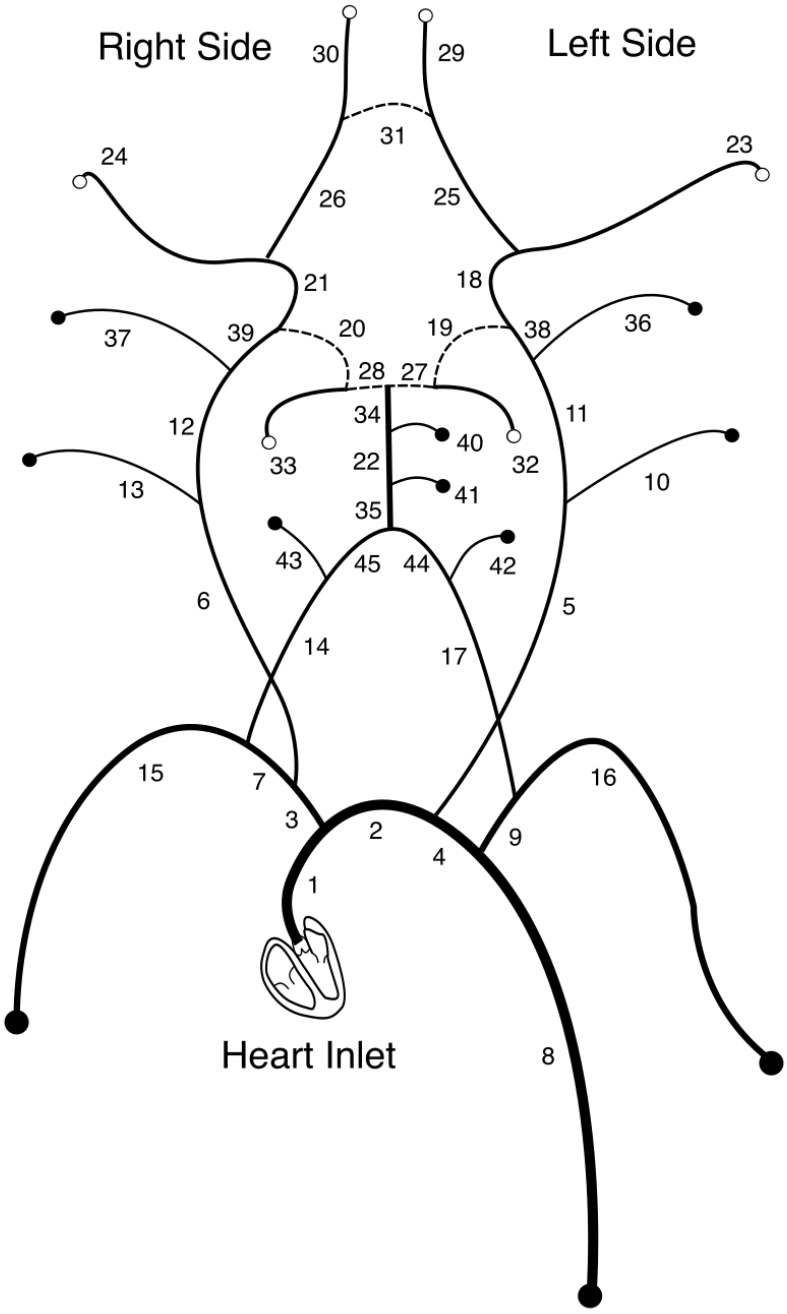

Figure (3.11) 1D vascular network representation with coverage of blood vessels relevant for cerebrovascular hemodynamics. Inlet condition (section 3.11.2) supplied at the aortic valve location (beginning of vessel 1). Terminal branches labeled with a filled circle have three-element Windkessel boundary conditions (section 3.11.3). Terminal branches labeled with an open circle are coupled to the LPN autoregulation model (chapter 4).

Conservation of momentum flux to maintain static continuous pressure:

$$\frac{1}{2}u_{parent}^2 + \frac{p_{parent}}{\rho} = \frac{1}{2}u_{daughter1}^2 + \frac{p_{daughter1}}{\rho}$$

$$\frac{1}{2}u_{parent}^2 + \frac{p_{parent}}{\rho} = \frac{1}{2}u_{daughter2}^2 + \frac{p_{daughter2}}{\rho}$$

3.11.2 Inlet Boundary Condition

As shown in Figure 3.11, the inlet boundary condition is applied at the beginning of the ascending aorta to represent the closest point to the aortic valve. A periodic inlet boundary condition ($Q_{in}(t)$) is applied to represent heart beats. Each cardiac cycle is assumed to be a half sine wave characterized by a peak value (Q_{max}) and a duration representing systole ($t_{systole} = 0.3$ sec). For the diastolic remainder of the cardiac cycle ($t_{diastole} = 0.9$ sec), a flow value of $Q_{in} = 0$ is prescribed. The purpose behind the zero flow rate is to represent the closure of the aortic valve. The closed aortic valve acts as a reflector and this characteristic is critical for the formation of the dicrotic notch in the aortic waveform. Note that a clinically-measured inlet waveform is explicitly not prescribed due to waveforms of that type already containing the influence of reflected waves which would thus be redundant to the pulse waves generated from the model [253].

$$Q_{in}(t) = \begin{cases} Q_{max} \sin\left(\frac{\pi t}{t_{systole}}\right) & \text{for } 0 \leq t \leq t_{systole} \\ 0 & \text{for } t_{systole} \leq t \leq t_{diastole} \end{cases}$$

3.11.3 Peripheral Windkessel Outlet Boundary Conditions

For the peripheral outlet blood vessels (non-autoregulation outlets), a three-element Windkessel model was applied to provide boundary conditions. The three elements are comprised of a characteristic resistance term (R_1), total downstream vascular bed resistance term (R_2), and total downstream vascular bed compliance term (C_T). The characteristic resistance (R_1) is organized in series to the parallel-organized total resistance (R_2) and total capacitance (C_T). The governing equation, derived through Kirchhoff's law, is as follows [262]:

$$\frac{dp(t)}{dt} + \frac{\Delta p}{R_2 C_T} = R_1 \frac{dq(t)}{dt} + \frac{q(R_1 + R_2)}{R_2 C_T}$$

For implementation, the Windkessel governing equation is discretized:

$$\frac{p_{n+1} - p_n}{\tau} + \frac{p_{n+1} - p_v}{R_2 C_T} = R_1 \frac{q_{n+1} - q_n}{\tau} + \frac{q_n(R_1 + R_2)}{R_2 C_T}$$

where p_v refers to venous pressure.

Solving for p_{n+1}:

$$p_{n+1} = \frac{\frac{R_1 R_2 C_T (q_{n+1} - q_n)}{\tau} + q_n(R_1 + R_2) + \frac{R_2 C_T p_n}{\tau} + p_v}{\left(1 + \frac{R_2 C_T}{\tau}\right)}$$

3.11.4 Autoregulation Outlet Boundary Conditions

Autoregulation outlet boundary conditions refer to those associated with autoregulation modeling and coupled to the cerebral lumped parameter network described in chapter 4. Ultimately, pressure at each autoregulation outlet will be provided by the lumped parameter network.

$$P_e = \frac{Q_d}{2G_d} + P_d$$

where Q_d, G_d, and P_d will be described further in chapter 4.

Chapter 4

Cerebral Lumped Parameter Network Formulation

4.1 Introduction

To effectively capture cerebral hemodynamics, it is essential to model the three main ways the brain can regulate blood flow. The first method is an autoregulatory response, where vascular beds will actively dilate or constrict based on current blood flow need. The second method is through the communicating arteries at the cerebral circle, also known as the circle of willis, which provides proximal collateral pathways. The third method is through smaller collateral connections in the distal pial arteries. These collateral connections are small vessels that run along the cortical surface of the brain and connect vascular territories together. The degree of communicating and collateral arteries largely determines the ability of the brain to reroute blood flow, which can determine, for example, stroke severity and outcome [263]. The cerebral blood flow regulation mechanisms are compelling to model because less than half the population has a complete cerebral circle [131] and approximately half of the population would typically be ranked has having good collateralization [263], which drives the need for patient-specific modeling in medical conditions of blood flow disruption. Additionally, the influence of age on cerebral hemodynamics, considering all of the various systemic vascular changes (chapter 1), is an important effect to incorporate in patient-specific modeling.

In this section, a comprehensive cerebral vascular model that has the ability to account for autoregulation, circle of willis variations, collateral flow modeling, and intracranial pressure in a patient-specific manner is described (Figure 4.1). The purpose of a lumped parameter model is to provide an equivalent vascular network representation with low computational expense and the ability to provide coupling behavior between all of these blood flow regulation phenomenon. Lumped parameter systems have direct analogs to electrical circuits where the design of the system utilizes a series of resistors and capacitors. In effect, a resistor-capacitor-resistor boundary condition best mimics the lumped behavior of a vascular bed. This means that a single radius vessel is used to represent each 1D outlet's downstream

network.

Autoregulation is built-in by having dynamic and nonlinear resistance elements whose values change by active myogenic processes that influence vessel tension and dilation. Essentially, this can be thought of as allowing these resistances to change based on a target flow rate. In building the rest of the lumped parameter model, to mimic the generation of cerebral-spinal fluid (CSF) from blood, each vascular territory has a resistor attached that pulls some fraction of the blood to be converted to CSF. The rest of the blood of this vascular territory then travels to the veins, hence another resistor is added for venous resistance. In the brain though, these cerebral territories are not isolated and flow can be shared across collateral channels. Hence, collateral connections between neighboring vascular territories are supplied where, ultimately, all connect downstream to a common ground which is the venous pressure. Collateral connections also exist across all six neighboring cerebral territories fed from the six major supplying arteries (such as a collateral connection between the right anterior cerebral artery and right middle cerebral artery). Specifically, the six major supplying arteries being represented as distal vascular territories are the anterior, middle, and posterior cerebral arteries. Additionally, this intracranial system requires cerebrospinal fluid reabsorption back to blood so an additional resistor is connected to the venous portion to represent this behavior. Lastly, the intracranial lumped parameter model is surrounded by a bounding box that represents the intracranial space filled with brain tissue. Here is where the non-linear relationship between intracranial pressure (ICP), cerebral blood flow, and cerebrospinal fluid generation/reabsorption is enforced. Ultimately, the lumped parameter network (LPN) model results in a series of ordinary differential equations with 19 total state variables solved using a backwards differentiation formulation and newton iteration [253, 264, 265].

4.2 Intracranial Compartment Volume Balance

In the design of the lumped parameter cerebrovascular model, an important characteristic is how cerebral blood flow is coupled to intracranial pressure and cerebrospinal fluid behavior. Following the Monro-Kellie principle [266], the skull (bounding box in Figure 4.1) represents a fully constrained volume filled with brain tissue, blood, and CSF, the balance of which then influences the intracranial pressure. The modeling of this behavior can be represented as a volume balance within a compliant volume (Equation 4.1). The LHS of equation 4.1 represents the compliance of the elastic brain C_{ic} with the intracranial pressure P_{ic}. The RHS of equation 4.1 is the volume balance of cerebral blood volume in each vascular territory and CSF inflow/outflow [253, 267].

$$C_{ic}\frac{dP_{ic}}{dt} = \sum_{k=1}^{6}\left(\frac{dV_k}{dt} + I_{f_k}\right) - I_o \tag{4.1}$$

where V_k is the blood volume for a modeled vascular territory, with k representing the six cerebral distal beds. Below, variables with the subscript k denote the quantity for each

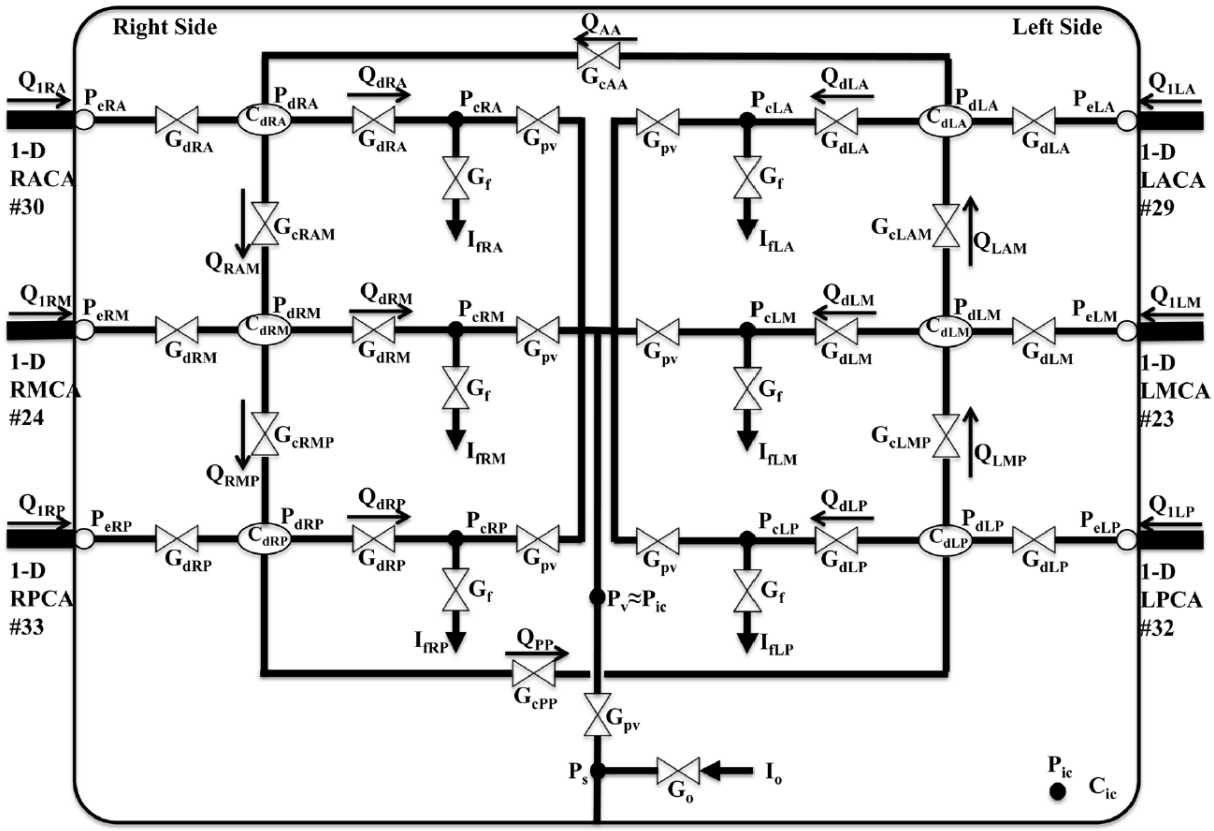

Figure (4.1) Lumped parameter model capable of modeling cerebrovascular autoregulation, collateral flow, CSF dynamimcs, and intracranial pressure. The six major supplying arteries being represented as distal vascular territories are the anterior, middle, and posterior cerebral arteries (R/L ACA, MCA and PCA). As blood travels from the coupled 1D inlets to the venous outlet of the LPN, dynamic autoregulation resistors, collateral pathways, and CSF pathways influence the distribution of blood flow to the various vascular territories under the volume constraint of the intracranial bounding box dynamics. Reproduced from [253] with permission.

vascular territory. I_f represents the production rate of CSF and I_o represents the outflow (reabsorption) of CSF.

4.2.1 Intracranial Compliance

Craniospinal compliance (C_{ic}), experimentally, has been shown not to be a simple linear relationship, but instead, is a non-linear function of ICP (P_{ic}) [267].

$$C_{ic} = \frac{1}{K_e|P_{ic} - P_{icn}| + \frac{1}{C_m}}$$

where K_e represents the elastance coefficient of the craniospinal compartment, P_{icn} represents the pressure value of maximum craniospinal compliance and C_m is a term to allow for model stability as P_{ic} approaches zero.

Solving for $\frac{dP_{ic}}{dt}$, the first state equation of the LPN is derived. The typical form of state equations is as such: $\dot{\vec{x}} = A\vec{x} + B\vec{u}$.

$$\frac{dP_{ic}}{dt} = \frac{\sum_{k=1}^{6}\left(\frac{dV_k}{dt} + I_{f_k}\right) - I_o}{C_{ic}} = \left(K_e|P_{ic} - P_{icn}| + \frac{1}{C_m}\right)\left(\sum_{k=1}^{6}\left(\frac{dV_k}{dt} + I_{f_k}\right) - I_o\right)$$

4.2.2 Vascular Territory Volume

To delineate the vascular pathways of the LPN (Figure 4.1), it is helpful to first define the pressure at various points across the model. P_e, P_d, P_c, P_s, and P_{ic} refers to 1D outflow, pial/small arterial beds, capillary, sagittal sinus, and intracranial pressure, respectively.

The change in blood volume for each vascular territory, is derived by the balance of inflow from the 1D outlets to the pial/small arterial beds, the outflow from the pial/small arterial beds to the capillary beds, and the inflow/outflow from neighboring collateral channels. Flow across a resistor is defined as $Q = \frac{P}{R} = G \cdot P$ where conductance is the inverse of resistance: $G = \frac{1}{R}$.

$$\frac{dV_k}{dt} = 2K_{v_k}r_{d_k} = G_{d_k}(P_{e_k} - P_{d_k}) - G_{d_k}(P_{d_k} - P_{c_k}) + \Delta Q_{coll_k}$$

where P_e, P_d, and P_c refers to 1D outflow, pial/small arterial beds, capillary, respectively. G_d represents the conductance of the pial arterial beds and K_v is a constant parameter designed to achieve a baseline blood volume in distal vascular beds further clarified in section 5.7.2. ΔQ_{coll_k} is the neighboring collateral flow further defined in section 4.4.

The conductance (also known as the inverse of the resistance) of the vascular bed ,G_{d_k}, is based on vessel radius following Poiseuille's Law:

$$G_{d_k} = K_{g_k}r_{d_k}^4$$

Note that due to the design of the LPN, G_{d_k} is half of vascular conductance of the modeled vascular territory. K_{g_k} is a constant parameter defined in section 5.7.1.

4.2.3 Cerebrospinal Fluid Inflow and Outflow

To model the direction-specific inflow and outflow of CSF, the pressure difference between the generation and reabsorption points are considered. For CSF inflow, the pressure difference between the vascular territory capillary vessel pressure and intracranial pressure influences the degree of CSF generation:

$$I_{f_k} = G_f(P_{c_k} - P_{ic})H(P_{c_k} - P_{ic})$$

where G_f is the conductance for the formation of CSF and H represents a heaviside function.

CSF production and reabsorption have one-way directionality, thus the purpose of the heaviside function is to maintain this one-way directionality.

Heaviside function:

$$H(x) := \begin{cases} 1, & x > 0 \\ 0, & x \leq 0 \end{cases}$$

For CSF outflow, the pressure difference between the intracranial pressure and sagittal sinus pressure (P_s) influences the degree of CSF reabsorption:

$$I_o = G_0(P_{ic} - P_s)H(P_{ic} - P_s)$$

where G_o is the conductance for the reabsorption of CSF.

4.2.4 Vascular Territory Pressure Equations

To further define the pressures within the LPN, the pressure in the capillary vessels of the vascular territory is represented by:

$$P_c = \frac{G_{pv}}{G_{pv} + G_d} P_{ic} + \frac{G_d}{G_{pv} + G_d} P_d$$

where G_{pv} is the conductance from the capillary to the venous bed.

4.3 Lumped Distal Vessel Vascular Bed Representation

To model cerebral autoregulation in the LPN, a key aspect is designing the dynamic and nonlinear resistance elements of the vascular territory. The changes of these resistance elements have been designed to mimic the active myogenic processes that govern vessel tension.

In the autoregulation design, is it assumed that a lumped distal vessel model can effectively capture the behavior of the entire vascular territory.

4.3.1 General Lumped Vascular Tension

Firstly, within the lumped distal vessel representing the vascular territory, the relationship between transmural pressure and vascular wall tension is applied by Laplace's law:

$$P_d r_d - P_{ic}(r_d + h_d) = T_d$$

where r_d is the lumped distal vessel radius, h_d is the lumped distal vessel wall thickness and T_d is the total lumped distal wall tension.

Total vascular tension is further decomposed into three components: passive elastic tension (T_e), viscous tension (T_v), and active tension (T_m).

$$T_d = T_e + T_v + T_m$$

4.3.2 Lumped Vessel Wall Thickness

For the derivation of the lumped distal vessel thickness at any vessel radius, a hollow thick pressurized cylinder is examined:

As defined, the unpressurized wall volume (Figure 4.2a) of the lumped vessel is as follows:

$$V_o = \pi l_o h_o (2(r_o + h_o) - h_o)$$

where V_o represents unpressurized wall volume, l_o represents unpressurized length, r_o represents unpressurized radius, and h_o represents unpressurized thickness.

Similarily, the pressurized wall volume (Figure 4.2b) of the lumped vessel is as follows:

$$V_d = \pi l_d h_d (2(r_d + h_d) - h_d)$$

where V_d represents pressurized wall volume, l_d represents pressurized length, r_d represents pressurized radius, and h_d represents pressurized thickness.

Assumptions of the lumped vessel are that the vessel wall volume is incompressible ($\upsilon = 0.5$) thus remaining constant ($V_o = V_d$) and that longitudinal strain can be neglected ($l_o = l_d$).

Setting the vessel wall volumes equal to each other:

$$\pi l_o h_o (2(r_o + h_o) - h_o) = \pi l_d h_d (2(r_d + h_d) - h_d)$$

$$2 r_o h_o + h_o^2 = h_d^2 + 2 r_d h_d$$

$$2 r_o h_o + h_o^2 = (h_d + r_d)^2 - r_d^2$$

$$h_d = -r_d + \sqrt{r_d^2 + 2 r_o h_o + h_o^2} \tag{4.2}$$

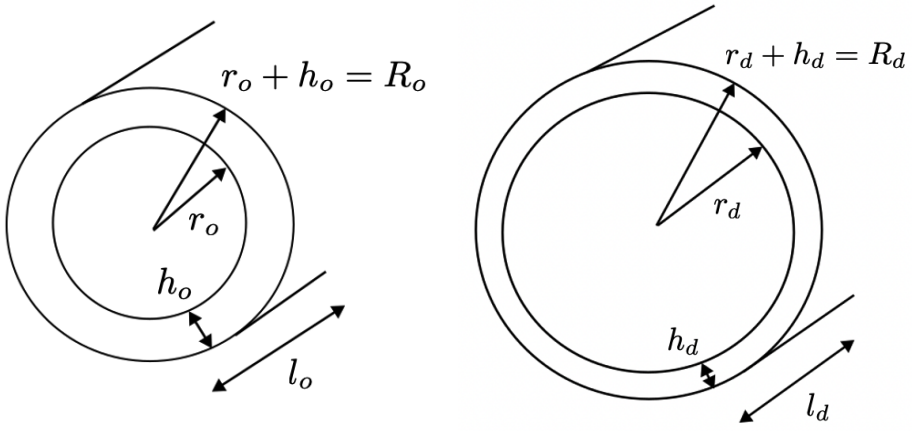

(a) (b)

Figure (4.2) a) Unpressurized hollow thick cylinder cross-section to represent the lumped distal blood vessel. b) Pressurized hollow thick cylinder cross-section.

4.3.3 Passive/Elastic Tension

The passive/elastic tensile behavior of the lumped blood vessel is applied through a radius-normalized exponential function:

$$T_e = h_d \sigma_{e_0} e^{K_\sigma \frac{r_d}{r_o}}$$

where σ_{e_0}, K_σ are constant model parameters assigned in section 2.5. r_o represents homeostatic radius of the blood vessel and acts as a normalization term for the current lumped blood vessel radius

Of note, this passive tension formulation assumes that T_e can never be negative. While this assumption is valid for tensile stress in a pressurized configuration, this assumption breaks down in radial compression of the blood vessel where, with enough compression, T_e can become negative [268].

4.3.4 Viscous Tension

The purpose of a viscous tension component to the total lumped vascular tension model is to dampen the intensity of wall movement (through the dampening of circumferential strain). The general formulation for viscous dampening is: $\sigma_v = \eta \frac{d\epsilon}{dt}$ where, $\epsilon_{\theta\theta} = (r_d - r_o)/r_o$ and η is a constant model parameter described in Section 5.4.

$$\sigma_v = \frac{\eta}{r_o} \frac{dr_d}{dt}$$

$$T_v = \frac{\eta h_d}{r_o}\frac{dr_d}{dt}$$

4.3.5 Active Tension

Active tension regulation of cerebral vessels, is maintained by circumferentially-aligned smooth muscle cell contraction/relaxation in response to an autoregulation stimulus (section 2.6). In the cerebrovascular LPN modeling, two of the most influential autoregulation components, myogenic tension (section 4.3.8) and CO_2 reactivity (section 4.3.9), are considered. While active tension compression and dilation were previously modeled as symmetric [253, 265], Chapter 2 describes asymmetric active tension behavior in terms of the homeostatic reference point (with respect to the minimum and maximum bounds of active tension), the sarcomere length-tension relationship, and varying contribution abilities of autoregulation components. Therefore, asymmetric modeling of active tension is a novel way to capture the intricacies of cerebral autoregulation applicable to a broad set of applications.

Broadly, the formulation for active tension (T_m) is derived around the reference point of homeostatic tension. Further, active tension is scaled through an intermediate variable M_{total} representing cerebral autoregulation activation factor (section 4.3.7). When T_m is at a global minimum, M_{total} is also at a global minimum representing complete vasodilation ($M_{total} = -1$). When T_m is at the homeostatic tension value, T_{homeo}, M_{total} is defined as $M_{total} = 0$. When T_m is at a global maximum, M is also at a global maximum representing complete vasoconstriction ($M_{total} = 1$).

$$M_{total} \Rightarrow -1 \rightarrow 0 \rightarrow 1$$
$$T_m \Rightarrow 0 \rightarrow T_{homeo} \rightarrow T_{max}$$

where T_{homeo} refers to the active tension at the homoestatic configuration and T_{max} refers to the maximum tension ability of the smooth muscle cells.

For the vasodilation and vasoconstriction conditions, with reference to the homeostatic state, a piece-wise formulation for active tension is defined:

if $M_{total} < 0$ (vasodilation):

$$T_m = [T_{homeo}(1 + M_{total})]\, e^{-\left|\frac{\bar{r}_d - r_{m_l}}{r_{t_l} - r_{m_l}}\right|^{n_{m_l}}}$$

if $M_{total} \geq 0$ (vasoconstriction):

$$T_m = [T_{homeo}(1 - M_{total}) + M_{total} T_{max}]\, e^{-\left|\frac{\bar{r}_d - r_{m_r}}{r_{t_r} - r_{m_r}}\right|^{n_{m_r}}}$$

where r_m, r_t, and n_m describe the shape of the active tension sarcomere length-tension relationship covered in section 4.3.6.

4.3.6 Active Tension Sarcomere Length-Tension Relationship

To explain the inclusion of this component of the active tension relationship, muscles generate force through having cross-bridge formations between overlapping actin and myosin filaments (these combinations are called sarcomeres). Depending on the resting state of the muscle, the sarcomeres can experience different levels of stretch (such as overly contracted or stretched too far) which affects muscle force response. Active tension is therefore maximal at a particular optimal value of inner radius and the progressively decreases with further contraction or stretch). This is known as the length-tension relationship [229].

Section 2.6 covers the length-tension relationship of cerebral blood vessels and, in particular, highlights the asymmetric behavior. The following sarcomere length-tension formulation splits the curve characterization into vasoconstriction and vasodilation components to capture the asymmetric fit. Importantly, the formulation is with respect to normalized vascular radius ($\bar{r}_d = \frac{r_d}{r_o}$) to maintain compatibility over any arbitrary radius.

Vasodilation:

$$e^{-\left|\frac{\bar{r}_d - r_{m_l}}{r_{t_l} - r_{m_l}}\right|^{n_{m_l}}}$$

Vasoconstriction:

$$e^{-\left|\frac{\bar{r}_d - r_{m_r}}{r_{t_r} - r_{m_r}}\right|^{n_{m_r}}}$$

4.3.7 Active Tension Activation Factor

The cerebral autoregulation activation factor (M_{total}), essentially, responds to maintain homeostatic conditions and doubles as an intermediate term to scale the maximum and minimum extent of active tension. The activation factor control function, M_{total}, is designed to be a sigmoid function that utilizes a first-order low pass system (x) to limit excessive changes:

$$M_{function} = \left(\frac{e^{2x} - 1}{e^{2x} + 1}\right)$$

Two of these sigmoid-type functions are built into M_{total} to account for the myogenic and CO_2 reactivity components of autoregulation. It is assumed that the autoregulation components act independently, due to independent sensors, and that their effective signal to smooth muscle cells is additive. Further, the additive effect is true up to the maximum and minimum bounds of M_{total}.

$$M_{total} = M_{myo} + M_{CO_2}$$

where $max(M_{total}) = 1$ and $min(M_{total}) = -1$.

4.3.8 Active Tension Myogenic Component

Starting with the myogenic component of active tension, the state variable x_{myo} dictates the activation factor of M_{myo} based on deviations from the homeostatic flow rate of the vascular territory.

$$M_{myo} = M_{function}(x_{myo})$$

There are an additional set of scaling parameters layered on M_{myo} to account for the component-specific activation limits. Essentially, if myogenic forces were signalling smooth muscle cells at maximum ability, the signal would not access the full range of smooth muscle cell ability (see section 2.10). The terms $A_{myo:C}$ and $A_{myo:D}$ dictate the asymmetric range of myogenic contribution ability.

if $x_{myo} \geq 0$ (vasoconstriction):

$$M_{myo} = A_{myo:C}\left(\frac{e^{2x_{myo}} - 1}{e^{2x_{myo}} + 1}\right)$$

if $x_{myo} < 0$ (vasodilation):

$$M_{myo} = A_{myo:D}\left(\frac{e^{2x_{myo}} - 1}{e^{2x_{myo}} + 1}\right)$$

The state variable x_{myo}, modeled as a first-order low pass system to limit excessive changes in M_{myo}, is characterized by a time constant τ_{myo} and gain G_{myo}. The degree of myogenic activation is dictated by flow rate deviations from the homeostatic flow rate.

$$\tau_{myo}\frac{dx_{myo}}{dt} = -x_{myo} + G_{myo}\frac{Q_d - Q_n}{Q_n}$$

where Q_{d_k} refers to cerebral blood flow rate at each of the vascular territories and Q_{n_k} represents the homeostatic flow rate of each vascular territory.

4.3.9 Active Tension CO_2 Reactivity Component

Similar to the myogenic component, the CO_2 reactivity component of active tension has a state variable x_{CO_2} that dictates the activation factor of M_{CO_2} based on deviations from the homeostatic CO_2 partial pressure of the arterial blood.

$$M_{CO_2} = M_{function}(x_{CO_2})$$

The terms $A_{CO_2:C}$ and $A_{CO_2:D}$ dictate the asymmetric range of CO_2 reactivity contribution ability.

if $x_{CO_2} \geq 0$ (vasoconstriction):

$$M_{CO_2} = A_{CO_2:C}\left(\frac{e^{2x_{CO_2}} - 1}{e^{2x_{CO_2}} + 1}\right)$$

if $x_{CO_2} < 0$ (vasodilation):

$$M_{CO_2} = A_{CO_2:D}\left(\frac{e^{2x_{CO_2}} - 1}{e^{2x_{CO_2}} + 1}\right)$$

The state variable x_{CO_2}, modeled as a first-order low pass system to limit excessive changes in M_{CO_2}, is characterized by a time constant τ_{CO_2} and gain G_{CO_2}. The degree of CO_2 reactivity autoregulation activation is dictated by deviations from the homeostatic CO_2 partial pressure of the arterial blood [269].

$$\tau_{CO_2}\frac{dx_{CO_2}}{dt} = -x_{CO_2} - G_{CO_2}A_{CO_2}log\left(\frac{Pa_{CO_2}}{Pan_{CO_2}}\right)$$

where Pa_{CO_2} refers to the current CO_2 partial pressure of arterial blood and Pan_{CO_2} refers to the homeostatic CO_2 partial pressure of arterial blood.

A_{CO_2} is a corrective factor term that essentially acts as an interaction term between myogenic and CO_2 reactivity regulation such that in conditions of excessive ischemia, the CO_2 reactivity influence on autoregulation is limited.

$$A_{CO_2} = \frac{1}{1 + e^{\left(-K_{CO_2}\left(\frac{Q_d - Q_n}{Q_n}\right) - b_{CO_2}\right)}}$$

where K_{CO_2} and b_{CO_2} are constant parameters that tune the degree of ischemia that limits CO_2 reactivity ability [269].

4.4 Cerebral and Collateral Flow Balance

Across the cerebral LPN, there are a series of distal collateral connections (cortical anasomosis) that allow for blood flow rerouting/sharing between vascular territories. For example, the flow to the right anterior cerebral distal vascular territory is a flow balance of flow entering the right anterior cerebral artery (from the coupled 1D model), flow shared with the neighboring left anterior cerebral vascular territory and flow shared with the neighboring right middle cerebral vascular territory. In the following equations, the subscripts of A, M, and P refer to the anterior, middle and posterior cerebral vascular territories [253].

$$Q_{dRA} = Q_{1RA} + Q_{AA} - Q_{RAM}$$

$$Q_{dLA} = Q_{1LA} - Q_{AA} + Q_{LAM}$$

$$Q_{dRM} = Q_{1RM} + Q_{RAM} - Q_{RMP}$$

$$Q_{dLM} = Q_{1LM} - Q_{LAM} + Q_{LMP}$$

$$Q_{dRP} = Q_{1RP} + Q_{RMP} - Q_{PP}$$

$$Q_{dLP} = Q_{1LP} - Q_{LMP} + Q_{PP}$$

For the determination of collateral flow between vascular territories, a conductance value (G_c) is supplied for the particular cortical collateral vessels along with the pressure difference between vascular territories. For example, the collateral flow between the right anterior and middle cerebral territories (Q_{RAM}) is based on the conductance between these territories (G_{cRAM}) and their pressure difference ($P_{dRA} - P_{dRM}$).

$$Q_{RAM} = G_{cRAM}(P_{dRA} - P_{dRM})$$

$$Q_{LAM} = G_{cLAM}(P_{dLM} - P_{dLA})$$

$$Q_{RMP} = G_{cRMP}(P_{dRM} - P_{dRP})$$

$$Q_{LMP} = G_{cLMP}(P_{dLP} - P_{dLM})$$

$$Q_{PP} = G_{cPP}(P_{dRP} - P_{dLP})$$

$$Q_{AA} = G_{cAA}(P_{dLA} - P_{dRA})$$

Lastly, flow to the venous bed is determined by:

$$Q_{venous} = G_{pv}(P_{c_k} - P_{ic})$$

4.5 LPN Cerebrovascular Model Solving

With the six cerebral autoregulation outlets, in total, the LPN model contains 19 state variables to be solved using a backwards differentiation formulation, with the inclusion of a newton iteration for the non-linear aspects, of the series of ordinary differential equations [253]. The state variables of LPN include distal radius r_d, myogenic activation x_{myo}, and CO_2 reactivity activation for each vascular bed with an additional state variable of intracranial pressure (P_{ic}) for the overall LPN model: $r_{d_{1\to6}}$, $x_{myo_{1\to6}}$, $x_{CO2_{1\to6}}$, P_{ic}. The input the LPN

equations is the flow rate from the coupled 1D outlets (Q_{1_k}). The time step size is set at: dt $= 5 \times 10^{-6}\, sec$.

The state equations of the cerebral LPN are as follows:

$$\frac{dr_{d_k}}{dt} = \frac{G_{d_k}(P_{e_k} - P_{d_k}) - G_{d_k}(P_{d_k} - P_{c_k}) + \Delta Q_{coll_k}}{2K_{v_k} r_{d_k}}$$

$$\frac{dx_{myo_k}}{dt} = \frac{-x_{myo_k} + G_{myo}\frac{Q_{d_k} - Q_{n_k}}{Q_{n_k}}}{\tau_{myo}}$$

$$\frac{dx_{CO2_k}}{dt} = \frac{-x_{CO2_k} - G_{CO_2} A_{CO_2} log\left(\frac{Pa_{CO2_k}}{Pan_{CO_2}}\right)}{\tau_{CO_2}}$$

$$\frac{dP_{ic}}{dt} = \left(K_e|P_{ic} - P_{icn}| + \frac{1}{C_m}\right)\left(\sum_{k=1}^{6}\left(\frac{dV_k}{dt} + I_{f_k}\right) - I_o\right)$$

Chapter 5

1D-LPN Cerebrovascular Model Parameter Values and Age-Related Parameter Tuning

5.1 Introduction

Previous chapters cover the current state-of-the-art for modeling cerebral hemodynamics with a coupled 1D and LPN model and age-related changes to the vascular system with age. A core aspect of the cerebrovascular model design is to facilitate patient-specific modeling and to provide relatively-quick hemodynamic predictions across a wide range of medical conditions. Thus, the parameter tuning of the cerebrovascular model becomes essential for accurate hemodynamic modeling. The following chapter discusses the on-going development of cerebrovascular model tuning and strategies for generating patient-specific hemodynamic simulations.

The challenges associated with tuning of the cerebrovascular model include varying sensitivity of model parameters [264], unknown ranges of parameters to obtain physiologically-valid simulations, high patient-specific variability of hemodynamic parameters, age-specific hemodynamic variability, and the high degree of freedom due to the number of cerebrovascular model parameters. In general, the tuning strategy utilized is to first reduce model complexity by introducing population-averaged age-dependent values for those parameters difficult or impossible to measure within an individual. Chapters 1 and 2 will supply the critical population-averaged age-dependent values that acts as a way to fix certain parameters within the 1D-LPN model and set objective function targets for parameters that cannot be directly set. Utilizing the same tuning framework, cerebrovascular model parameters can be further modified to be patient-specific, but with age-dependent considerations that would not typically be measured across patients. The advantage of having age-related tuning is the reduction of patient-specific tuning complexity by pre-determining parameter values that are difficult or currently impossible to measure with non-invasive imaging.

For the tuning procedure, parameter variables will be classified as age-independent fixed, age-dependent fixed, free parameters, and scaled parameters. Age-independent fixed variables refer to cardiovascular or cerebrovascular parameters that are age-independent and remain fixed at a population level, but could be modified if patient-specific data is provided. Age-dependent fixed variables refer to cardiovascular or cerebrovascular variables that are age-dependent and are known at the population level, but could be modified if patient-specific data is provided. Both age-independent fixed and age-dependent fixed parameters will be directly set in the cerebrovascular tuning process. Free variables are sensitive cerebrovascular parameters that either cannot be directly set or are released to allow for additional degrees of freedom for appropriate tuning. Scaled parameters are those parameter values directly scaled by the free variables which could have age-dependent modifications.

5.2 Age-Independent Fixed 1D Model Parameters

As part of the parameter assignment for the 1D portion of the cerebrovascular model, there are a series of parameters that are assigned in a age-independent fixed fashion. To fulfill the incompressible and Newtonian fluid assumptions of the 1D modeling (Section 3.2), the parameter values of blood density ($\rho = 1.05 \times 10^3\, kg \cdot \mathrm{m}^{-3}$) and blood shear viscosity ($\mu = 4.05 \times 10^{-3}\, Pa \cdot \mathrm{s}$) are constant [253]. For the 1D cerebrovascular arterial network design, both arterial geometry and topology, 1D arterial segments are assigned based on population-averaged values [253]. In particular, for each 1D arterial segment, a value of unpressurized cross-sectional area (A_o) and vascular length (L) were assigned (Table 5.1). The values of A_o, from the Section 3.6.2 formulation, were estimated such that at typical arterial blood pressure, the pressurized cross sectional-area (A) would approximate measured angiography data. Similarly, the values of L, from the Section 3.8 formulation, were approximated from angiography data.

5.3 Age-Dependent Fixed 1D Model Parameters

As part of the parameter assignment for the 1D portion of the cerebrovascular model, there are a series of parameters that are assigned in a age-dependent fixed fashion. These parameters include cardiac output, vascular segment stiffness, outlet flow distributions, outlet resistance, and outlet compliance.

For the inlet condition of the 1D model, the assigned cardiac output parameter is dependent on age. Specifically, Q_{max}, formulated in Section 3.11.2, is defined based on the relationship from Section 1.2.1. The half sine wave peak value, Q_{max}, is calculated such that the total flow prescribed to the inlet matches the mean cardiac output calculated from Section 1.2.1.

In the aging vasculature, the elastic modulus parameter for aortic stiffness, which undergoes significant age-related changes, is assigned from Section 1.2.9. For the remaining vascu-

Artery Name	Vessel ID	A_0 $[m^2]$	L $[m]$
ascending aorta	1	4.52389E-04	4.00E-02
ascending aorta II	2	3.94081E-04	2.00E-02
brachiocephalic	3	1.20763E-04	3.40E-02
descending aorta	4	3.59681E-04	3.90E-02
L common carotid	5	1.96349E-05	2.08E-01
R common carotid	6	1.96349E-05	1.77E-01
subclavian	7, 9	5.62122E-05	3.40E-02
descending aorta II	8	3.13531E-04	1.56E-01
external carotid	10, 13	7.06858E-06	1.77E-01
internal carotid	11, 12	1.25664E-05	1.66E-01
vertebral	14, 17	5.81068E-06	1.28E-01
brachial	15, 16	5.10222E-05	4.22E-01
internal carotid III	18, 21	1.25664E-05	5.00E-03
posterior communicating	19, 20	8.00000E-07	1.50E-02
basilar	22	8.24479E-06	1.90E-02
middle cerebral	23, 24	6.42424E-06	1.19E-01
anterior cerebral	25, 26	4.30052E-06	1.20E-02
posterior cerebral	27, 28	3.59681E-06	5.00E-03
anterior cerebral II	29, 30	4.52389E-06	1.03E-01
anterior communicating	31	8.00000E-07	3.00E-03
posterior cerebral	32, 33	3.46360E-06	8.60E-02
basilar II	34, 35	8.24479E-06	5.00E-03
ophthalmic	36, 37	8.00000E-07	1.00E-02
internal carotid II	38, 39	1.25664E-05	1.10E-02
superior cerebellar	40	2.47340E-06	1.00E-02
anterior inferior cerebellar	41	2.47340E-06	1.00E-02
posterior inferior cerebellar	42, 43	2.47340E-06	1.00E-02
vertebral II	44, 45	2.47340E-06	2.00E-02

Table (5.1) The artery name, vessel ID, unpressurized cross-sectional area, and vessel length parameters of the 1D portion of the cerebrovascular model from Figure 3.11 [253]. Unpressurized cross-sectional areas were determined from typical arterial pressures and population-averaged pressurized angiography data.

Peripheral Outlet Name	Vessel ID	Percent of Cardiac Output [%]
descending aorta II	8	$0.7983 \cdot \frac{peripheralFlow}{CO}$
R brachial	15	$0.0819 \cdot \frac{peripheralFlow}{CO}$
L brachial	16	$0.0825 \cdot \frac{peripheralFlow}{CO}$
external carotid	10, 13	$0.0175 \cdot \frac{peripheralFlow}{CO}$
ophthalmic	36, 37	$0.0011 \cdot \frac{peripheralFlow}{CO}$
superior cerebellar	40	$0.0409 \cdot \frac{tCBF}{CO}$
anterior inferior cerebellar	41	$0.0081 \cdot \frac{tCBF}{CO}$
posterior inferior cerebellar	42, 43	$5.0505E\text{-}04 \cdot \frac{tCBF}{CO}$
Autoregulation Outlet Name	**Vessel ID**	**Percent of Cardiac Output [%]**
middle cerebral	23, 24	$0.2267 \cdot \frac{tCBF}{CO}$
anterior cerebral	25, 26	$0.1403 \cdot \frac{tCBF}{CO}$
posterior cerebral	27, 28	$0.1080 \cdot \frac{tCBF}{CO}$

Table (5.2) The peripheral/autoregulation outlet boundary condition artery name, vessel ID, and the age-dependent flow distribution of cardiac output assumed for the 1D portion of the cerebrovascular model from Figure 3.11. Derived from Section 1.2.3, the flow distribution to each peripheral/autoregulation outlet is defined with respect to the age-dependent ratio of total cerebral blood flow (tCBF) and cardiac output (CO). $\frac{tCBF}{CO}$ is defined as the ratio of tCBF to CO, where $\frac{peripheralFlow}{CO}$ is defined as $\frac{peripheralFlow}{CO} = 1 - \frac{tCBF}{CO}$. Flow distribution data was acquired from [57] for peripheral outlets and from [72, 75] for autoregulation outlets.

lature, a normalized elastic modulus equation is developed based on a stiffness gradient across generalized homeostatic vascular diameter [37]: $E_{\theta\theta}[MPa] = -1.69E^4 * d_{homeo}[mm] + 1.14E^6$. The use of elastic modulus is based on the formulation from Section 3.6.2.

To assign target flow rates throughout the 1D model, the age-dependent ratio of total cerebral blood flow (tCBF) to cardiac output (CO) is first calculated (Section 1.2.3). Next flow distributions are further assigned to both peripheral and autoregulation outlets following Table 5.2. While target flow rates are assigned at the autoregulation boundary conditions, peripheral outlets have a non-direct assignment of flow rates based around resistance scaling (Section 3.11.3). For each peripheral outlet, age-dependent total systemic resistance (Section 1.2.3 and 5.6) is distributed based on Ohm's Law for parallel resistors: $\frac{1}{R_{systemic}} = \frac{1}{R_{outlet} \cdot FlowDistribution_{outlet}}$. Similar to the assignment of outlet resistance, total vascular compliance is distributed based on Ohm's Law for parallel capacitors: $C_{outlet} = C_{systemic} \cdot FlowDistribution_{outlet}$.

5.4 Age-Independent Fixed LPN Model Parameters

As part of the parameter assignment for the LPN portion of the cerebrovascular model, there are a series of parameters that are assigned in a age-independent fixed fashion. These parameters include those for passive tension, viscous tension, active tension length-tension relationship, autoregulation gain and time constants, CO_2 reactivity-specific behavior, relative autoregulation strength, intracranial dynamics, CSF generation/reabsorption, and venous behavior.

Within the passive tension formulation (Section 4.3.3), one of the parameter values, K_σ, is age-independent and fix. The value for K_σ is derived from Section 2.5. Similarly, η, from the viscous tension formulation (Section 4.3.4), remains fixed with age [253]. Values for both K_σ and η are provided in Table 5.3.

Within the active tension formulation for the sarcomere length-tension relationship (Section 4.3.6), the parameter values of r_{m_l}, r_{t_l}, n_{m_l}, r_{m_r}, r_{t_r}, and n_{m_r} are age-independent and defined from Section 2.6. The non-symmetric behavior of the normalized length-tension relationship is incorporated by the piece-wise formulation. Values for these parameters are provided in Table 5.3.

Within the autoregulation formulation, both myogenic (Section 4.3.8) and metabolic (Section 4.3.9), have many parameter values that are age-independent and fixed throughout the tuning process. Age-independent values include the autoregulation gain constants (G_{myo}, G_{CO_2}) and time constants (τ_{myo}, τ_{CO_2}). Parameter values for autoregulation gain constants are derived from [253], while parameter values for autoregulation time constants are defined from Section 2.3. Further, additional parameters that govern the behavior of metabolic / CO_2 reactivity, Pan_{CO_2}, K_{CO_2} and b_{CO_2} from Section 4.3.9, are age-independent [269]. Lastly, the autoregulation relative strength parameters, $A_{myo:C}$, $A_{myo:D}$, $A_{CO_2:C}$ and $A_{CO_2:D}$ derived from 2.10, are age-independent. Values for autoregulation parameters are provided in Table 5.3.

Lastly, LPN parameters governing intracranial dynamics, CSF generation/reabsorption, and venous behavior have age-independent components. Parameter values for intracranial dynamics, K_e, P_{icn} and C_m formulated in Section 4.2.1, are derived from [253, 267]. Parameter values for CSF generation/reabsorption, G_f and G_o formulated in Section 4.2.3, and venous behavior, G_{pv} and P_s formulated in Section 4.4, are derived from [253]. Values for age-independent LPN parameters are provided in Table 5.3.

5.5 Age-Dependent Fixed LPN Model Parameters

As part of the parameter assignment for the LPN portion of the cerebrovascular model, there are a series of parameters that are assigned in an age-dependent fixed fashion. These parameters include those for cerebral outlet target flow rate and collateral resistance.

The age-dependent outlet target flow rates, labeled as Q_n from Section 4.3.8, are defined in Table 5.2. Following similar procedures to Section 5.3, resistance and compliance

Passive Tension	**Viscous Tension**	
$K_\sigma = 21.16$	$\eta = 232$ mmHg $\cdot$ s	
Active Length-Tension		
$r_{m_l} = 1.0$	$r_{t_l} = 1.3168$	$n_{m_l} = 1.5048$
$r_{m_r} = 1.0$	$r_{t_r} = 0.8859$	$n_{m_r} = 3.2550$
Myogenic Autoregulation		
$G_{myo} = 0.5\frac{1}{\text{mmHg}}$	$\tau_{myo} = 6.7$ s	
$A_{myo:C} = 0.06$	$A_{myo:D} = 0.33$	
Metabolic Autoregulation		
$G_{CO_2} = 15.5\frac{1}{\text{mmHg}}$	$\tau_{CO_2} = 20$ s	
$A_{CO_2:C} = 0.75$	$A_{CO_2:D} = 1.03$	
$Pan_{CO_2} = 40$ mmHg	$K_{CO_2} = 20$	$b_{CO_2} = 0.65$
Intracranial Dynamics		
$K_e = 0.077\frac{1}{\text{mL}}$	$P_{icn} = 9.5$ mmHg	$C_m = 1.3671\frac{\text{mL}}{\text{mmHg}}$
Cerebrospinal Fluid Dynamics		
$G_f = 7.00E^{-5}\frac{\text{mL}}{\text{mmHg}\cdot\text{s}}$	$G_o = 3.167E^{-4}\frac{\text{mL}}{\text{mmHg}\cdot\text{s}}$	
Venous Dynamics		
$G_{pv} = 0.189\frac{\text{mL}}{\text{mmHg}\cdot\text{s}}$	$P_s = 6.0$ mmHg	

Table (5.3) Age-independent fixed parameters for the LPN portion of the cerebrovascular model.

	$r_{d_{MCA}}$ [cm]	$r_{d_{ACA}}$ [cm]	$r_{d_{PCA}}$ [cm]	R_{total} Scaling
Parameter Range	[.04 -.27]	[.02 -.24]	[.02 -.20]	[.5 - 2.5]

Table (5.4) Free cerebrovascular model parameters ranges for the Bayesian optimization procedure.

values can be distributed to the autoregulation outlets. Lastly, the age-dependent collateral resistances, G_c formulated in Section 4.4, are derived from Section 1.3.5.

5.6 Free Variable LPN Parameters

Remaining after the assignment of both the age-independent and age-dependent fixed cerebrovascular model parameters is the determination of the free variables for the cerebrovascular model tuning process. One of the most important free variables in the model is the outlet state variable: lumped distal radius (r_{d_k}). As a state variable, the cerebrovascular model does not have direct control of this value, but the assumed homeostatic value of the lumped distal radius influences numerous sensitive features including passive tension, active tension, and flow rate. The tuning process is thus apriori predicting the homeostatic lumped distal radius value for each autoregulation outlet. For a coarse cerebrovascular model tuning procedure, to decrease the number of objective function evaluations required, symmetry is assumed for the lumped distal radius values. For patient-specific considerations, the assumption of symmetry can be relaxed in exchange for a higher computational cost. Additionally, a total systemic vascular resistance scaling term was added to the free variables due to the variable's strong influence on blood pressure in the model. While there is an age-dependent estimation for total systemic resistance, considering it as a free variable add a degree of freedom into the tuning process to assist with convergence. Ranges for all free variables are provided in Table 5.4.

5.7 Scaled LPN Model Parameters

For each iteration of the cerebrovascular model tuning procedure, in order to reduce the number of free variables, estimates for the remaining LPN parameters are scaled based off of the current iteration's free variable values. Overall, keeping lumped distal radius as a free variable has systemic implications across the entire cerebrovascular model tuning process. Importantly, the free variable lumped distal radius values (r_{d_k}) have a significant scaling impact on many cerebrovascular model aspects including passive tension, active tension, autoregulation outlet resistance, and autoregulation outlet blood volume.

The scaled LPN model parameters for passive tension include h_o and σ_{eo}. h_o is formulated in Section 4.3.2 with parameter values provided from Section 1.2.11. σ_{eo} is formulated in

Section 4.3.3 with parameter values derived from 2.5. h_o and σ_{eo} are both scaled based on homeostatic lumped distal radius.

The scaled LPN model parameters for active tension include T_{homeo} and T_{max}. Both T_{homeo} and T_{max} are formulated in Section 4.3.5 with parameter values derived from 2.9. T_{homeo} and T_{max} are both scaled based on homeostatic lumped distal radius.

5.7.1 Outlet Resistance

Another important and sensitive variable in the cerebrovascular model is K_{g_k} influencing the outlet resistance of each lumped vascular bed (formulation in Section 4.2.2) [267]. Based on the assigned target flow rate, Q_n, an approximate homeostatic resistance value for each autoregulation outlet can be calculated. Paired with the free variable value for lumped distal radius, K_{g_k} is scaled accordingly.

Outlet resistance for 1D model:

$$R_{CA_{outlet}} = \left(\frac{2}{K_g r_d^4} + \frac{2}{G_{pv}} \right)$$

Scaled approximation for K_g:

$$K_g = \frac{2}{r_d^4} \frac{1}{R_{CA_{outlet}} - \frac{2}{G_{pv}}}$$

5.7.2 Outlet Blood Volume

Keeping the lumped distal radius value as a free variable has scaling implications for K_{v_k} (formulated in Section 4.2.2). In the vascular bed volume balance equation, K_{v_k}, representing the length of the lumped distal blood vessel, is a sensitive parameter of the cerebrovascular model [267]. The first assumption made with K_{v_k}, like the free variable r_{d_k}, is symmetry but this assumption can be relaxed in a patient-specific context. The second assumption for K_{v_k} is that K_{v_k}, or essentially lumped vessel volume, linearly scales with lumped distal radius r_{d_k}. Note that an alternative way to solve for K_{v_k} is to utilize approximate vascular bed volume, derived from Section 1.3.3.

Approximation of vascular arterial beds:

$$\frac{dV_k}{dt} = 2K_{v_k} r_{d_k} \frac{dr_k}{dt}$$

$$V_k = \sum K_{v_k} r_{d_k}^2$$

$$V_k = K_{v_1} r_{d_1}^2 + K_{v_2} r_{d_2}^2 + K_{v_3} r_{d_3}^2 + K_{v_4} r_{d_4}^2 + K_{v_5} r_{d_5}^2 + K_{v_6} r_{d_6}^2$$

Assuming r_{d_k} symmetry:

$$V_k = 2K_{v_1} r_{d_1}^2 + 2K_{v_2} r_{d_2}^2 + 2K_{v_3} r_{d_3}^2$$

$$\frac{K_{v_1}}{K_{v_2}} = \frac{r_{d_1}}{r_{d_2}}$$
$$\frac{K_{v_1}}{K_{v_3}} = \frac{r_{d_1}}{r_{d_3}}$$
$$\frac{K_{v_2}}{K_{v_3}} = \frac{r_{d_2}}{r_{d_3}}$$

5.8 Free LPN Parameter Fitting

5.8.1 Bayesian Optimization Theory

Bayesian optimization, the methodology being utilized for the free parameter tuning of the cerebrovascular model, is a gradient-free optimization technique commonly used by machine learning algorithms to minimize an objective function [270]. One of the main advantages of bayesian optimization includes enhanced efficiency for situations with expensive cost function evaluations and uncertainty in the global minima location. Bayesian optimization can be thought of using a surrogate optimization procedure where a surrogate function is assumed based on existing initial values or prior values (also known as a gaussian process). The Bayesian aspect of the optimization is employed in the estimation of the confidence interval between the gaussian process surrogate function and the true function value. Then, the objective function is further evaluated in areas of low confidence to explore global minima and in areas of high confidence to locate the best observed value. Any new evaluation points are known as the posterior, and are thus added to the prior to improve the estimations for each new iteration.

5.8.2 Latin Hypercube Initialization and Bayesian Optimization Settings

To initially sample the free variable domain space, latin hypercube (LHC) sampling is an alternative to Monte Carlo that is slightly more efficient due to a more evenly distributing samples across the domain space [271]. The evaluation of the objective function at each sample provides the prior to the bayesian optimization. As the number of input variables and objective function evaluations increases, LHC sampling approaches Monte Carlo in terms of efficiency. Providing an appropriate sampling of the domain space allows for the exploration of global minima. For the cerebrovascular tuning, with four free variables (Section 5.8) and an expensive cost function evaluation, LHC provides one of the most efficient methods for sampling the free variable domain space. For the current free parameter tuning procedure,

900 LHC samples are evaluated across the domain space with 2000 maximum bayesian optimization evaluations. The objective function was evaluated at the 20th cardiac cycle for each converged cerebrovascular simulation.

5.8.3 Objective Function

The objective function for the bayesian optimization procedure is guided by 9 different comparison evaluations. Relevant for the 1D portion of the cerebrovascular model, the cross-sectional areas of each simulated vessel segment are compared against their expected area values, model peripheral flow rates are compared against target peripheral flow rates, and model mean systemic blood pressure, pulse wave velocity, and cerebrospinal fluid flow rates are compared against expected age-dependent values. For the lumped parameter objective values of the cerebrovascular model, the most important for this particular tuning problem, model cerebral flow rates are compared against expected target values, cerebral autoregulation is checked against homeostatic values, lumped parameter radius is compared against assigned homeostatic target values and lastly, intracranial pressure range is checked against an expected range. All objective function components are self-normalized so that weighting terms can be equally applied across all components.

1D Cerebrovascular Objective Function Components:

1. Model 1D vessel cross-sectional mean areas matches expected angiography data (Table 5.1).

$$OFC_1 = \sum_{ID} \frac{|A_{ID} - A_{n_{ID}}|}{A_{n_{ID}}}$$

2. Model peripheral mean flow rates matches target values (Table 5.2).

$$OFC_2 = \sum_{ID} \frac{|Q_{ID} - Q_{n_{ID}}|}{Q_{n_{ID}}}$$

3. Model mean systemic blood pressure matches target values (Section 1.2.2).

$$OFC_3 = \frac{|BP_{model} - BP_{target}|}{BP_{target}}$$

4. Model cfPWV matches target values (Section 1.2.10).

$$OFC_4 = \frac{|cfPWV_{model} - cfPWV_{target}|}{cfPWV_{target}}$$

5. Model mean CSF matches target values (Section 1.2.7).

$$OFC_5 = \frac{|CSF_{model} - CSF_{target}|}{CSF_{target}}$$

LPN Cerebrovascular Objective Function Components:

6. Model autoregulation outlet mean flow rates match target values (Table 5.2).

$$OFC_6 = \sum_k \frac{|q_{d_k} - q_{n_k}|}{q_{n_k}}$$

7. Cerebral autoregulation mean activation factor is within homeostatic range (Section 4.3.7).

$$OFC_7 = \begin{cases} 0 & \text{for } |M_{k_{model}}| \leq 0.05 \\ \sum_k |M_{k_{model}}| & \text{for } else \end{cases}$$

8. Model lumped distal mean radius matches target homeostatic values (Section 5.6).

$$OFC_8 = \sum_k \frac{|r_{d_k} - r_{homeo_k}|}{r_{homeo_k}}$$

9. Model mean intracranial pressure matches within expected range (Section 4.2.1).

$$OFC_9 = \begin{cases} 0 & \text{for } 7 \text{ mmHg} \leq ICP_{model} \leq 15 \text{ mmHg} \\ 1 & \text{for } else \end{cases}$$

The objective function weightings (Table 5.5) focus heavily on the lumped parameter network objectives with the objective function components of lumped distal radius and intracranial pressure being the most heavily weighted.

$$OF = \sum_{a=1}^{9} OFC_a \cdot W_a$$

$W_1 = 0.1$	$W_2 = 0.1$	$W_3 = 1.0$
$W_4 = 0.0$	$W_5 = 1.0$	$W_6 = 1.0$
$W_7 = 2.0$	$W_8 = 15.0$	$W_9 = 10.0$

Table (5.5) Objective function component weights.

Age [years]	$r_{d_{MCA}}$ [cm]	$r_{d_{ACA}}$ [cm]	$r_{d_{PCA}}$ [cm]	R_{total} Scaling
25	0.0519	0.0353	0.0382	1.7197

Table (5.6) Final free variable parameter values from the completed Bayesian optimization. Results are compiled for a population-average young 25 year old individual with idealized vascular aging.

5.9 Fitting Results for Age-Specific Tuning

At the completion of the bayesian optimization maximum number of objective function evaluations or the reaching of the optimal global tolerance, the tuning process identifies the free variables with the global minimum objective function. Example free variable parameters of a young 25 year old with idealized vascular aging are provided in Table 5.6. Figure 5.1 supplies each iteration step of the minimization of the global objective value with only the converged simulation results counting as an iterations (all non-converged free variable configurations were filtered out). Similarly, Figure 5.2 supplies each converged iteration step for the highly weighted lumped distal radius objective function component. For the global objective value and lumped distal radius objective function component, a base and ideal tolerance level was reached for each, respectively.

5.9.1 Future Tuning Work

Further objective function weighting modifications, free variable inclusions, and/or scaling variable alterations are needed for the fine tuning of the cerebovascular model. While coarse tuning objectives are achieved with current tuning protocols, objective function components such as the cerebrospinal fluid and intracranial components are not yet matched to reasonable tolerances. Additionally, current converged total systemic resistance scaling values are higher than expected age-related values. Lastly, the establishment of a pre-tuned model parameter database across all ages will allow for a simpler and more efficient estimation of free variable ranges (to lower computational expense) for future patient-specific tuning protocols built upon the provided age-specific tuning protocol.

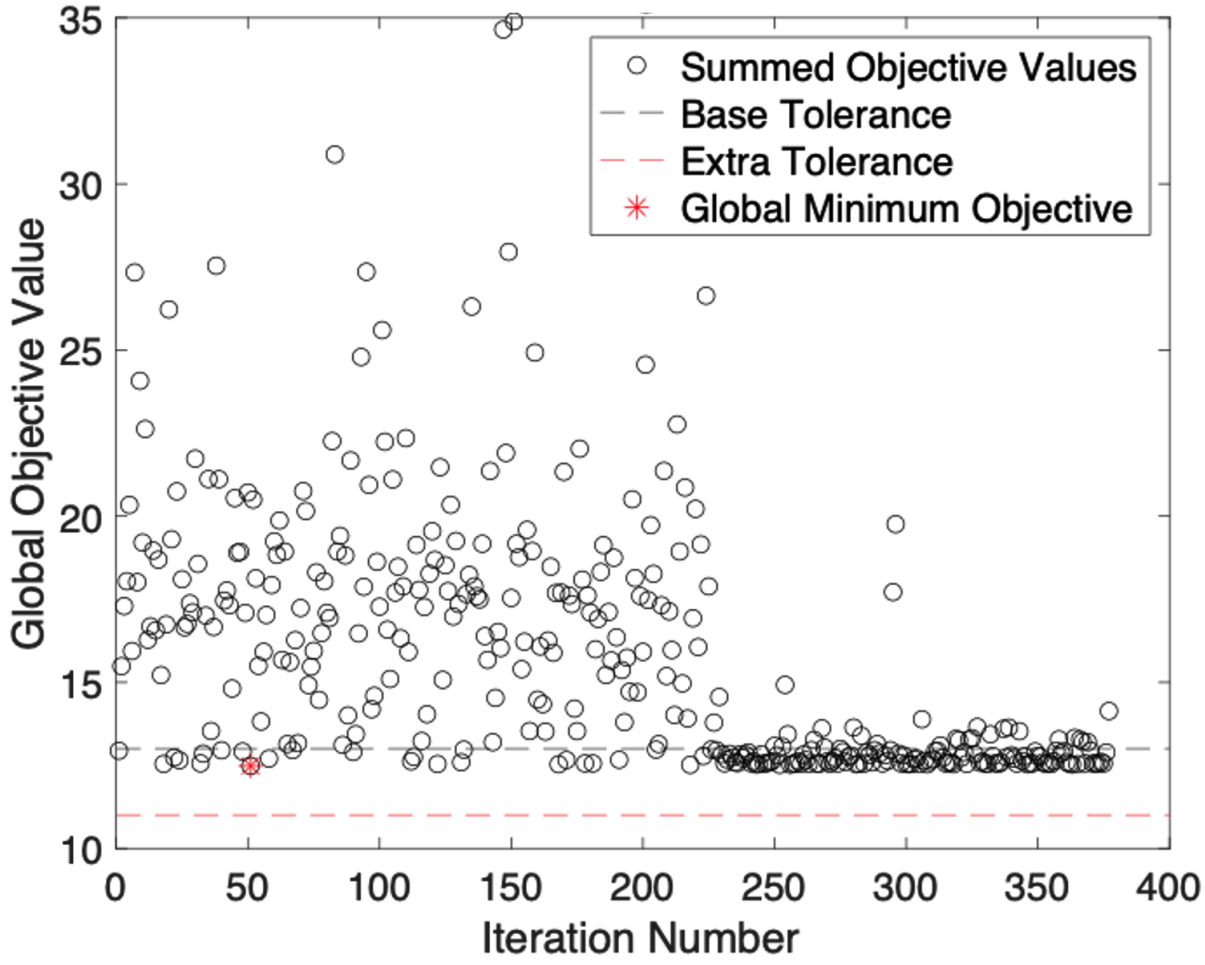

Figure (5.1) Global objective function tuning of a 25 year old individual with idealized vascular aging. Base and ideal tolerance levels are provided with the minimum objective evaluation.

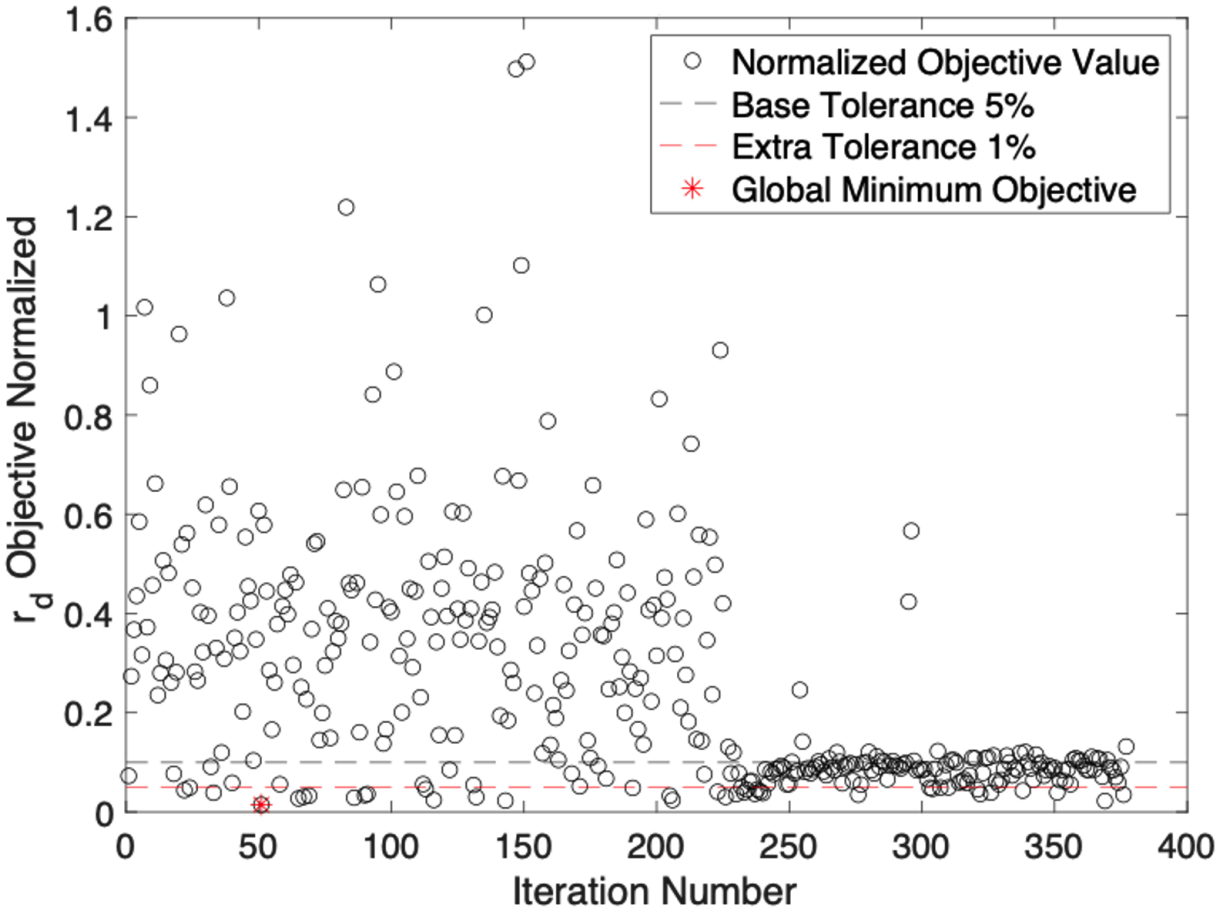

Figure (5.2) Lumped distal radius objective function component tuning of a 25 year old individual with idealized vascular aging. Base and ideal tolerance levels are provided with the minimum objective evaluation.

Bibliography

[1] Colin D Mathers and Dejan Loncar. "Projections of global mortality and burden of disease from 2002 to 2030". In: *PLoS medicine* 3.11 (2006), e442.

[2] RWV Flynn, RSM MacWalter, and ASF Doney. "The cost of cerebral ischaemia". In: *Neuropharmacology* 55.3 (2008), pp. 250–256.

[3] Michael A Moskowitz, Eng H Lo, and Costantino Iadecola. "The science of stroke: mechanisms in search of treatments". In: *Neuron* 67.2 (2010), pp. 181–198.

[4] Behnam Sabayan et al. "Cerebrovascular hemodynamics in Alzheimer's disease and vascular dementia: a meta-analysis of transcranial Doppler studies". In: *Ageing research reviews* 11.2 (2012), pp. 271–277.

[5] Peter Toth et al. "Functional vascular contributions to cognitive impairment and dementia: mechanisms and consequences of cerebral autoregulatory dysfunction, endothelial impairment, and neurovascular uncoupling in aging". In: *American Journal of Physiology-Heart and Circulatory Physiology* 312.1 (2016), H1–H20.

[6] Melanie D Sweeney et al. "The role of brain vasculature in neurodegenerative disorders". In: *Nature neuroscience* 21.10 (2018), p. 1318.

[7] Raj N Kalaria. "The role of cerebral ischemia in Alzheimer's disease". In: *Neurobiology of aging* 21.2 (2000), pp. 321–330.

[8] John T O'Brien and Alan Thomas. "Vascular dementia". In: *The Lancet* 386.10004 (2015), pp. 1698–1706.

[9] Poornima Venkat, Michael Chopp, and Jieli Chen. "Models and mechanisms of vascular dementia". In: *Experimental neurology* 272 (2015), pp. 97–108.

[10] Katja Ritz et al. "Cause and mechanisms of intracranial atherosclerosis". In: *Circulation* 130.16 (2014), pp. 1407–1414.

[11] Juan F Arenillas and José Álvarez-Sabın. "Basic mechanisms in intracranial large-artery atherosclerosis: advances and challenges". In: *Cerebrovascular Diseases* 20.Suppl. 2 (2005), pp. 75–83.

[12] C Lecrux and E Hamel. "The neurovascular unit in brain function and disease". In: *Acta physiologica* 203.1 (2011), pp. 47–59.

[13] OB Paulson. "Blood–brain barrier, brain metabolism and cerebral blood flow". In: *European Neuropsychopharmacology* 12.6 (2002), pp. 495–501.

[14] Philipp Mergenthaler et al. "Sugar for the brain: the role of glucose in physiological and pathological brain function". In: *Trends in neurosciences* 36.10 (2013), pp. 587–597.

[15] Mark W Peters, Peter B Canham, and Helen M Finlay. "Circumferential alignment of muscle cells in the tunica media of the human brain artery". In: *Journal of Vascular Research* 20.5 (1983), pp. 221–233.

[16] Gary L Baumbach and Donald D Heistad. "Regional, segmental, and temporal heterogeneity of cerebral vascular autoregulation". In: *Annals of biomedical engineering* 13.3-4 (1985), p. 303.

[17] Tobias Kulik et al. "Regulation of cerebral vasculature in normal and ischemic brain". In: *Neuropharmacology* 55.3 (2008), pp. 281–288.

[18] Eszter Farkas and Paul GM Luiten. "Cerebral microvascular pathology in aging and Alzheimer's disease". In: *Progress in neurobiology* 64.6 (2001), pp. 575–611.

[19] Stephen Payne. *Cerebral autoregulation: control of blood flow in the brain*. Springer, 2016.

[20] MAURO Ursino, PATRIZIA Di Giammarco, and ENZO Belardinelli. "A mathematical model of cerebral blood flow chemical regulation. I. Diffusion processes". In: *IEEE Transactions on Biomedical Engineering* 36.2 (1989), pp. 183–191.

[21] Yuan-cheng Fung. *Biomechanics: mechanical properties of living tissues*. Springer Science & Business Media, 2013.

[22] Peter F Davies. "Flow-mediated endothelial mechanotransduction". In: *Physiological reviews* 75.3 (1995), pp. 519–560.

[23] T.M. De Silva and F.M. Faraci. "Chapter 7 - Cerebral Vascular Muscle". In: *Primer on Cerebrovascular Diseases (Second Edition)*. Ed. by Louis R. Caplan et al. Second Edition. San Diego: Academic Press, 2017, pp. 42–47. ISBN: 978-0-12-803058-5.

[24] Paul M Vanhoutte et al. "Modulation of vascular smooth muscle contraction by the endothelium". In: *Annual Review of Physiology* 48.1 (1986), pp. 307–320.

[25] GEOFFREY BURNSTOCK. "Release of vasoactive substances from endothelial cells by shear stress and purinergic mechanosensory transduction". In: *The Journal of Anatomy* 194.3 (1999), pp. 335–342.

[26] David W Busija and Donald D Heistad. "Factors involved in the physiological regulation of the cerebral circulation". In: *Reviews of Physiology, Biochemistry and Pharmacology, Volume 101*. Springer, 1984, pp. 161–211.

[27] Murad Banaji et al. "A physiological model of cerebral blood flow control". In: *Mathematical biosciences* 194.2 (2005), pp. 125–173.

[28] GL Smith et al. "A review of the actions and control of intracellular pH in vascular smooth muscle". In: *Cardiovascular research* 38.2 (1998), pp. 316–331.

[29] R.J. Traystman. "Chapter 11 - Cerebral Blood Flow Regulation (Carbon Dioxide, Oxygen, and Nitric Oxide)". In: *Primer on Cerebrovascular Diseases (Second Edition)*. Ed. by Louis R. Caplan et al. Second Edition. San Diego: Academic Press, 2017, pp. 60–67. ISBN: 978-0-12-803058-5.

[30] H Hotta. "Neurogenic control of parenchymal arterioles in the cerebral cortex". In: *Progress in brain research*. Vol. 225. Elsevier, 2016, pp. 3–39.

[31] Nathaniel H Greene and Lorri A Lee. "Modern and evolving understanding of cerebral perfusion and autoregulation". In: *Advances in anesthesia* 30.1 (2012), pp. 97–129.

[32] Gail D Thomas. "Neural control of the circulation". In: *Advances in physiology education* 35.1 (2011), pp. 28–32.

[33] Horacio Kaufmann, Lucy Norcliffe-Kaufmann, and Jose-Alberto Palma. "Baroreflex dysfunction". In: *New England Journal of Medicine* 382.2 (2020), pp. 163–178.

[34] Julie C Kohn, Marsha C Lampi, and Cynthia A Reinhart-King. "Age-related vascular stiffening: causes and consequences". In: *Frontiers in genetics* 6 (2015), p. 112.

[35] Laurent Duca et al. "Matrix ageing and vascular impacts: focus on elastin fragmentation". In: *Cardiovascular research* 110.3 (2016), pp. 298–308.

[36] Jessica E Wagenseil and Robert P Mecham. "Elastin in large artery stiffness and hypertension". In: *Journal of cardiovascular translational research* 5.3 (2012), pp. 264–273.

[37] Charalambos Vlachopoulos, Michael O'Rourke, and Wilmer W Nichols. *McDonald's blood flow in arteries: theoretical, experimental and clinical principles*. CRC press, 2011.

[38] Edouard Fonck et al. "Effect of aging on elastin functionality in human cerebral arteries". In: *Stroke* 40.7 (2009), pp. 2552–2556.

[39] JD Humphrey et al. "Fundamental role of axial stress in compensatory adaptations by arteries". In: *Journal of biomechanics* 42.1 (2009), pp. 1–8.

[40] Imo E Hoefer, Brigit den Adel, and Mat JAP Daemen. "Biomechanical factors as triggers of vascular growth". In: *Cardiovascular research* 99.2 (2013), pp. 276–283.

[41] Alexander Rachev. "Remodeling of arteries in response to changes in their mechanical environment". In: *Biomechanics of soft tissue in cardiovascular systems*. Springer, 2003, pp. 221–271.

[42] JD Humphrey. "Vascular adaptation and mechanical homeostasis at tissue, cellular, and sub-cellular levels". In: *Cell biochemistry and biophysics* 50.2 (2008), pp. 53–78.

[43] WCA Man and Yu Wang. "Age-associated arterial remodelling". In: *EC Cardiology* (2017).

[44] Bernard J van Varik et al. "Mechanisms of arterial remodeling: lessons from genetic diseases". In: *Frontiers in genetics* 3 (2012), p. 290.

[45] Jorge A Castorena-Gonzalez et al. "Mechanisms of the inward remodeling process in resistance vessels: is the actin cytoskeleton involved?" In: *Microcirculation* 21.3 (2014), pp. 219–229.

[46] Carmel M McEniery et al. "Normal vascular aging: differential effects on wave reflection and aortic pulse wave velocity: the Anglo-Cardiff Collaborative Trial (ACCT)". In: *Journal of the American College of Cardiology* 46.9 (2005), pp. 1753–1760.

[47] Ryo Katori. "Normal cardiac output in relation to age and body size". In: *The Tohoku Journal of Experimental Medicine* 128.4 (1979), pp. 377–387.

[48] Ambarish Pandey et al. "Healthy aging and cardiovascular function: Invasive hemodynamics during rest and exercise in 104 healthy volunteers". In: *JACC: Heart Failure* 8.2 (2020), pp. 111–121.

[49] Marcus Carlsson et al. "Cardiac output and cardiac index measured with cardiovascular magnetic resonance in healthy subjects, elite athletes and patients with congestive heart failure". In: *Journal of Cardiovascular Magnetic Resonance* 14.1 (2012), pp. 1–7.

[50] Dalane W Kitzman and William D Edwards. "Age-related changes in the anatomy of the normal human heart". In: *Journal of gerontology* 45.2 (1990), pp. M33–M39.

[51] David A Kass. "Age-related changes in venticular–arterial coupling: pathophysiologic implications". In: *Heart failure reviews* 7.1 (2002), pp. 51–62.

[52] Gianfranco Parati et al. "Prognostic value of blood pressure variability and average blood pressure levels in patients with hypertension and diabetes". In: *Diabetes care* 36.Supplement 2 (2013), S312–S324.

[53] Maria H Mehlum et al. "Blood pressure variability and risk of cardiovascular events and death in patients with hypertension and different baseline risks". In: *European heart journal* 39.24 (2018), pp. 2243–2251.

[54] *Centers for Disease Control and Prevention (CDC). National Center for Health Statistics (NCHS). National Health and Nutrition Examination Survey Data. Hyattsville, MD: U.S. Department of Health and Human Services, Centers for Disease Control and Prevention, 2005-2006 https://wwwn.cdc.gov/nchs/nhanes/ContinuousNhanes/Default.aspx?BeginYear=2005.*

[55] Stanley S. Franklin et al. "Hemodynamic Patterns of Age-Related Changes in Blood Pressure". In: *Circulation* 96.1 (1997), pp. 308–315.

[56] Angelo Scuteri et al. "Longitudinal perspective on the conundrum of central arterial stiffness, blood pressure, and aging". In: *Hypertension* 64.6 (2014), pp. 1219–1227.

[57] Pablo J Blanco et al. "Blood flow distribution in an anatomically detailed arterial network model: criteria and algorithms". In: *Biomechanics and modeling in mechanobiology* 13.6 (2014), pp. 1303–1330.

[58] Chang-Yang Xing et al. "Distribution of cardiac output to the brain across the adult lifespan". In: *Journal of Cerebral Blood Flow & Metabolism* 37.8 (2017), pp. 2848–2856.

[59] Mark E Leithe et al. "The effect of age on central and regional hemodynamics". In: *Gerontology* 30.4 (1984), pp. 240–246.

[60] Gary E McVeigh et al. "Age-related abnormalities in arterial compliance identified by pressure pulse contour analysis: aging and arterial compliance". In: *Hypertension* 33.6 (1999), pp. 1392–1398.

[61] Giles N Cattermole et al. "The normal ranges of cardiovascular parameters measured using the ultrasonic cardiac output monitor". In: *Physiological reports* 5.6 (2017), e13195.

[62] J Alastruey et al. "Lumped parameter outflow models for 1-D blood flow simulations: effect on pulse waves and parameter estimation". In: *Communications in Computational Physics* 4.2 (2008), pp. 317–336.

[63] KEVIN P Davy and DOUGLAS R Seals. "Total blood volume in healthy young and older men". In: *Journal of applied physiology* 76.5 (1994), pp. 2059–2062.

[64] Hidemasa Takao, Naoto Hayashi, and Kuni Ohtomo. "A longitudinal study of brain volume changes in normal aging". In: *European journal of radiology* 81.10 (2012), pp. 2801–2804.

[65] Rachael I Scahill et al. "A longitudinal study of brain volume changes in normal aging using serial registered magnetic resonance imaging". In: *Archives of neurology* 60.7 (2003), pp. 989–994.

[66] Catriona D Good et al. "A voxel-based morphometric study of ageing in 465 normal adult human brains". In: *Neuroimage* 14.1 (2001), pp. 21–36.

[67] Ivan I Kirov et al. "Global brain volume and N-acetyl-aspartate decline over seven decades of normal aging". In: *Neurobiology of Aging* 98 (2021), pp. 42–51.

[68] Lorna Harper et al. "Patterns of atrophy in pathologically confirmed dementias: a voxelwise analysis". In: *Journal of Neurology, Neurosurgery & Psychiatry* 88.11 (2017), pp. 908–916.

[69] Anthony F Fotenos et al. "Normative estimates of cross-sectional and longitudinal brain volume decline in aging and AD". In: *Neurology* 64.6 (2005), pp. 1032–1039.

[70] David Smeijer, M Kamran Ikram, and Saima Hilal. "Enlarged Perivascular Spaces and Dementia: A Systematic Review". In: *Journal of Alzheimer's Disease* Preprint (2019), pp. 1–10.

[71] Can Wu et al. "Age-related changes of normal cerebral and cardiac blood flow in children and adults aged 7 months to 61 years". In: *Journal of the American Heart Association* 5.1 (2016), e002657.

[72] Laleh Zarrinkoob et al. "Blood flow distribution in cerebral arteries". In: *Journal of Cerebral Blood Flow & Metabolism* 35.4 (2015), pp. 648–654.

[73] Bente Pakkenberg and Hans Jørgen G Gundersen. "Neocortical neuron number in humans: effect of sex and age". In: *Journal of comparative neurology* 384.2 (1997), pp. 312–320.

[74] Pieter C Buijs et al. "Effect of age on cerebral blood flow: measurement with ungated two-dimensional phase-contrast MR angiography in 250 adults." In: *Radiology* 209.3 (1998), pp. 667–674.

[75] Sepideh Amin-Hanjani et al. "Effect of age and vascular anatomy on blood flow in major cerebral vessels". In: *Journal of Cerebral Blood Flow & Metabolism* 35.2 (2015), pp. 312–318.

[76] Adriaan CGM van Es et al. "Associations between total cerebral blood flow and age related changes of the brain". In: *PloS one* 5.3 (2010), e9825.

[77] Jeroen Hendrikse et al. "Distribution of cerebral blood flow in the circle of Willis". In: *Radiology* 235.1 (2005), pp. 184–189.

[78] A Fleur van Raamt et al. "Arterial blood flow to the brain in patients with vascular disease: the SMART Study". In: *Radiology* 240.2 (2006), pp. 515–521.

[79] Meike W Vernooij et al. "Total cerebral blood flow and total brain perfusion in the general population: the Rotterdam Scan Study". In: *Journal of Cerebral Blood Flow & Metabolism* 28.2 (2008), pp. 412–419.

[80] Manu S Goyal et al. "Aerobic glycolysis in the human brain is associated with development and neotenous gene expression". In: *Cell metabolism* 19.1 (2014), pp. 49–57.

[81] Manu S Goyal et al. "Loss of brain aerobic glycolysis in normal human aging". In: *Cell metabolism* 26.2 (2017), pp. 353–360.

[82] Carolyn Cidis Meltzer et al. "Comparative evaluation of MR-based partial-volume correction schemes for PET". In: *Journal of Nuclear Medicine* 40.12 (1999), pp. 2053–2065.

[83] Vicente Ibáñez et al. "Resting state brain glucose metabolism is not reduced in normotensive healthy men during aging, after correction for brain atrophy". In: *Brain research bulletin* 63.2 (2004), pp. 147–154.

[84] Fumihito Yoshii et al. "Sensitivity of cerebral glucose metabolism to age, gender, brain volume, brain atrophy, and cerebrovascular risk factors". In: *Journal of Cerebral Blood Flow & Metabolism* 8.5 (1988), pp. 654–661.

[85] Carolyn Cidis Meltzer et al. "Does cerebral blood flow decline in healthy aging? A PET study with partial-volume correction". In: *Journal of Nuclear Medicine* 41.11 (2000), pp. 1842–1848.

[86] Souraya Stoquart-ElSankari et al. "Aging effects on cerebral blood and cerebrospinal fluid flows". In: *Journal of Cerebral Blood Flow & Metabolism* 27.9 (2007), pp. 1563–1572.

[87] B Schaller. "Physiology of cerebral venous blood flow: from experimental data in animals to normal function in humans". In: *Brain research reviews* 46.3 (2004), pp. 243–260.

[88] Jody L Greaney and William B Farquhar. *Why do veins stiffen with advancing age?* 2011.

[89] Laurent Sakka, Guillaume Coll, and Jean Chazal. "Anatomy and physiology of cerebrospinal fluid". In: *European annals of otorhinolaryngology, head and neck diseases* 128.6 (2011), pp. 309–316.

[90] Hansotto Reiber. "Proteins in cerebrospinal fluid and blood: barriers, CSF flow rate and source-related dynamics". In: *Restorative neurology and neuroscience* 21.3, 4 (2003), pp. 79–96.

[91] Nader El Khatib et al. "Mathematical modelling of atherosclerosis". In: *Mathematical modelling of natural phenomena* 14.6 (2019), p. 603.

[92] Linda L Demer and Yin Tintut. "Vascular calcification: pathobiology of a multifaceted disease". In: *Circulation* 117.22 (2008), pp. 2938–2948.

[93] Oddmund Joakimsen et al. "Age and sex differences in the distribution and ultrasound morphology of carotid atherosclerosis: the Tromsø Study". In: *Arteriosclerosis, thrombosis, and vascular biology* 19.12 (1999), pp. 3007–3013.

[94] Xuan Shi et al. "Calcification in Atherosclerotic Plaque Vulnerability: Friend or Foe?" In: *Frontiers in Physiology* 11 (2020), p. 56.

[95] João L Cavalcante et al. "Aortic stiffness: current understanding and future directions". In: *Journal of the American College of Cardiology* 57.14 (2011), pp. 1511–1522.

[96] Julio A Chirinos et al. "Large-artery stiffness in health and disease: JACC state-of-the-art review". In: *Journal of the American College of Cardiology* 74.9 (2019), pp. 1237–1263.

[97] Isabel N Schellinger, Karin Mattern, and Uwe Raaz. "The Hardest Part: Arterial Stiffness in the Context of Healthy Aging". In: *Arteriosclerosis, thrombosis, and vascular biology* 39.7 (2019), pp. 1301–1306.

[98] Gary F Mitchell et al. "Arterial stiffness, pressure and flow pulsatility and brain structure and function: the Age, Gene/Environment Susceptibility–Reykjavik study". In: *Brain* 134.11 (2011), pp. 3398–3407.

[99] Michael F O'rourke and Junichiro Hashimoto. "Mechanical factors in arterial aging: a clinical perspective". In: *Journal of the American College of Cardiology* 50.1 (2007), pp. 1–13.

[100] Darren Haskett et al. "Microstructural and biomechanical alterations of the human aorta as a function of age and location". In: *Biomechanics and modeling in mechanobiology* 9.6 (2010), pp. 725–736.

[101] Åsa Rydén Ahlgren et al. "Stiffness and diameter of the common carotid artery and abdominal aorta in women". In: *Ultrasound in medicine & biology* 23.7 (1997), pp. 983–988.

[102] Floris L Wuyts et al. "Elastic properties of human aortas in relation to age and atherosclerosis: a structural model". In: *Physics in Medicine & Biology* 40.10 (1995), p. 1577.

[103] Alban Redheuil et al. "Reduced ascending aortic strain and distensibility: earliest manifestations of vascular aging in humans". In: *Hypertension* 55.2 (2010), pp. 319–326.

[104] Athanase Benetos et al. "Arterial alterations with aging and high blood pressure. A noninvasive study of carotid and femoral arteries." In: *Arteriosclerosis and thrombosis: a journal of vascular biology* 13.1 (1993), pp. 90–97.

[105] Lian Engelen et al. "Reference values for local arterial stiffness. Part A: carotid artery". In: *Journal of hypertension* 33.10 (2015), pp. 1981–1996.

[106] Daniel Bia et al. "Integrated evaluation of age-related changes in structural and functional vascular parameters used to assess arterial aging, subclinical atherosclerosis, and cardiovascular risk in Uruguayan adults: CUiiDARTE project". In: *International Journal of Hypertension* 2011 (2011).

[107] Pierre Boutouyrie et al. "Opposing effects of ageing on distal and proximal large arteries in hypertensives." In: *Journal of hypertension. Supplement: official journal of the International Society of Hypertension* 10.6 (1992), S87–91.

[108] Janneke J van der Heijden-Spek et al. "Effect of age on brachial artery wall properties differs from the aorta and is gender dependent: a population study". In: *Hypertension* 35.2 (2000), pp. 637–642.

[109] Janice M Diaz-Otero et al. "Aging is associated with changes to the biomechanical properties of the posterior cerebral artery and parenchymal arterioles". In: *American Journal of Physiology-Heart and Circulatory Physiology* 310.3 (2016), H365–H375.

[110] Michael A Hajdu et al. "Effects of aging on mechanics and composition of cerebral arterioles in rats." In: *Circulation research* 66.6 (1990), pp. 1747–1754.

[111] Mohammad Shafigh, Nasser Fatouraee, and A Seddighi. "Determining the biomechanical properties of human intracranial blood vessels through biaxial tensile test and fitting them to a hyperelastic model". In: *Engineering Solid Mechanics* 1.2 (2013), pp. 43–56.

[112] Justine Ina Davies and Allan D Struthers. "Pulse wave analysis and pulse wave velocity: a critical review of their strengths and weaknesses". In: *Journal of hypertension* 21.3 (2003), pp. 463–472.

[113] Alberto Milan et al. "Current assessment of pulse wave velocity: comprehensive review of validation studies". In: *Journal of hypertension* 37.8 (2019), pp. 1547–1557.

[114] Yi Zhang et al. "Characteristics of pulse wave velocity in elastic and muscular arteries: a mismatch beyond age". In: *Journal of Hypertension* 31.3 (2013), pp. 554–559.

[115] Reference Values for Arterial Stiffness' Collaboration. "Determinants of pulse wave velocity in healthy people and in the presence of cardiovascular risk factors:'establishing normal and reference values'". In: *European heart journal* 31.19 (2010), pp. 2338–2350.

[116] Alejandro Dıaz et al. "Reference values of pulse wave velocity in healthy people from an urban and rural argentinean population". In: *International journal of hypertension* 2014 (2014).

[117] Peter H Charlton et al. "Modeling arterial pulse waves in healthy aging: a database for in silico evaluation of hemodynamics and pulse wave indexes". In: *American Journal of Physiology-Heart and Circulatory Physiology* 317.5 (2019), H1062–H1085.

[118] Alyssa A Torjesen et al. "Forward and backward wave morphology and central pressure augmentation in men and women in the Framingham Heart Study". In: *Hypertension* 64.2 (2014), pp. 259–265.

[119] DB Camasão and DJMTB Mantovani. "The mechanical characterization of blood vessels and their substitutes in the continuous quest for physiological-relevant performances. A critical review". In: *Materials Today Bio* 10 (2021), p. 100106.

[120] Kazunori Nakagawa and Yutaka Nakashima. "Pathologic intimal thickening in human atherosclerosis is formed by extracellular accumulation of plasma-derived lipids and dispersion of intimal smooth muscle cells". In: *Atherosclerosis* 274 (2018), pp. 235–242.

[121] Aleksandra Milutinović, Dušan Šuput, and Ruda Zorc-Pleskovič. "Pathogenesis of atherosclerosis in the tunica intima, media, and adventitia of coronary arteries: An updated review". In: *Bosnian journal of basic medical sciences* 20.1 (2020), p. 21.

[122] David M Pierce et al. "A method for incorporating three-dimensional residual stretches /stresses into patient-specific finite element simulations of arteries". In: *Journal of the mechanical behavior of biomedical materials* 47 (2015), pp. 147–164.

[123] Hannah Weisbecker et al. "Layer-specific damage experiments and modeling of human thoracic and abdominal aortas with non-atherosclerotic intimal thickening". In: *Journal of the mechanical behavior of biomedical materials* 12 (2012), pp. 93–106.

[124] Zhongzhao Teng et al. "An experimental study on the ultimate strength of the adventitia and media of human atherosclerotic carotid arteries in circumferential and axial directions". In: *Journal of biomechanics* 42.15 (2009), pp. 2535–2539.

[125] Evrim B Turkbey et al. "Determinants and normal values of ascending aortic diameter by age, gender, and race/ethnicity in the Multi-Ethnic Study of Atherosclerosis (MESA)". In: *Journal of Magnetic Resonance Imaging* 39.2 (2014), pp. 360–368.

[126] I Van den Munckhof et al. "Impact of age and sex on carotid and peripheral arterial wall thickness in humans". In: *Acta physiologica* 206.4 (2012), pp. 220–228.

[127] John A Bevan et al. "As human pial arteries (internal diameter 200–1000 μm) get smaller, their wall thickness and capacity to develop tension relative to their diameter increase". In: *Life sciences* 65.11 (1999), pp. 1153–1161.

[128] Reba Babu Alex and Lathikumari Kalyani Kutty Amma. "Microanatomical study of age changes in tunica media of ascending aorta". In: *Journal of Evolution of Medical and Dental Sciences* 5.101 (2016), pp. 7409–7413.

[129] Jang-Ho Bae et al. "The changes of individual carotid artery wall layer by aging and carotid intima-media thickness value for high risk". In: *Cardiovascular Therapeutics* 34.6 (2016), pp. 397–403.

[130] Khaled Menshawi, Jay P Mohr, and Jose Gutierrez. "A functional perspective on the embryology and anatomy of the cerebral blood supply". In: *Journal of stroke* 17.2 (2015), p. 144.

[131] S Iqbal. "A comprehensive study of the anatomical variations of the circle of willis in adult human brains". In: *Journal of clinical and diagnostic research: JCDR* 7.11 (2013), p. 2423.

[132] Zvonimir Vrselja et al. "Function of circle of Willis". In: *Journal of Cerebral Blood Flow & Metabolism* 34.4 (2014), pp. 578–584.

[133] Arjun Burlakoti et al. "The cerebral basal arterial network: morphometry of inflow and outflow components". In: *Journal of Anatomy* 230.6 (2017), pp. 833–841.

[134] JR Cebral et al. "Flow–area relationship in internal carotid and vertebral arteries". In: *Physiological measurement* 29.5 (2008), p. 585.

[135] Christophe Chnafa et al. "Vessel calibre and flow splitting relationships at the internal carotid artery terminal bifurcation". In: *Physiological Measurement* 38.11 (2017), p. 2044.

[136] Cassot Francis et al. "Scaling laws for branching vessels of human cerebral cortex". In: *Microcirculation* 16.4 (2009), pp. 331–344.

[137] Hamidreza Rajabzadeh-Oghaz et al. "Inter-patient variations in flow boundary conditions at middle cerebral artery from 7T PC-MRI and influence on computational fluid dynamics of intracranial aneurysms". In: *Computers in biology and medicine* 120 (2020), p. 103759.

[138] Chang S Park et al. "Quantification of blood flow patterns in the cerebral arterial circulation of individual (human) subjects". In: *International journal for numerical methods in biomedical engineering* 36.1 (2020), e3288.

[139] Laurent Tatu et al. "Arterial territories of the human brain". In: *Manifestations of Stroke*. Vol. 30. Karger Publishers, 2012, pp. 99–110.

[140] Nolan S Hartkamp et al. "Mapping of cerebral perfusion territories using territorial arterial spin labeling: techniques and clinical application". In: *NMR in Biomedicine* 26.8 (2013), pp. 901–912.

[141] Michael A Chappell et al. "A general framework for the analysis of vessel encoded arterial spin labeling for vascular territory mapping". In: *Magnetic resonance in medicine* 64.5 (2010), pp. 1529–1539.

[142] Dong-Eog Kim et al. "Mapping the supratentorial cerebral arterial territories using 1160 large artery infarcts". In: *JAMA neurology* 76.1 (2019), pp. 72–80.

[143] Albert van der Zwan and Berend Hillen. "Review of the variability of the territories of the major cerebral arteries." In: *Stroke* 22.8 (1991), pp. 1078–1084.

[144] Nolan S Hartkamp et al. "Misinterpretation of ischaemic infarct location in relationship to the cerebrovascular territories". In: *Journal of Neurology, Neurosurgery & Psychiatry* 87.10 (2016), pp. 1084–1090.

[145] Michaël Bernier, Stephen C Cunnane, and Kevin Whittingstall. "The morphology of the human cerebrovascular system". In: *Human brain mapping* 39.12 (2018), pp. 4962–4975.

[146] Roberto Viviani. "A digital atlas of middle to large brain vessels and their relation to cortical and subcortical structures". In: *Frontiers in neuroanatomy* 10 (2016), p. 12.

[147] Wieslaw L Nowinski et al. "Analysis of ischemic stroke MR images by means of brain atlases of anatomy and blood supply territories". In: *Academic radiology* 13.8 (2006), pp. 1025–1034.

[148] Dong-Eog Kim et al. "Supratentorial Cerebral Arterial Territories for Computed Tomograms: A Mapping Study in 1160 Large Artery Infarcts". In: *Scientific reports* 9.1 (2019), pp. 1–8.

[149] Alun D Hughes. "Optimality, cost minimization and the design of arterial networks". In: *Artery research* 10 (2015), pp. 1–10.

[150] Qing Pan et al. "A one-dimensional mathematical model for studying the pulsatile flow in microvascular networks". In: *Journal of biomechanical engineering* 136.1 (2014), p. 011009.

[151] Axel R Pries and Tim W Secomb. "Microvascular blood viscosity in vivo and the endothelial surface layer". In: *American Journal of Physiology-Heart and Circulatory Physiology* 289.6 (2005), H2657–H2664.

[152] Albert van der Zwan et al. "A quantitative investigation of the variability of the major cerebral arterial territories." In: *Stroke* 24.12 (1993), pp. 1951–1959.

[153] Hai-Chao Han. "Twisted blood vessels: symptoms, etiology and biomechanical mechanisms". In: *Journal of vascular research* 49.3 (2012), pp. 185–197.

[154] Clara R Thore et al. "Morphometric analysis of arteriolar tortuosity in human cerebral white matter of preterm, young, and aged subjects". In: *Journal of neuropathology and experimental neurology* 66.5 (2007), pp. 337–345.

[155] Elizabeth Bullitt et al. "The effects of healthy aging on intracerebral blood vessels visualized by magnetic resonance angiography". In: *Neurobiology of aging* 31.2 (2010), pp. 290–300.

[156] Myron D Ginsberg. "The cerebral collateral circulation: Relevance to pathophysiology and treatment of stroke". In: *Neuropharmacology* 134 (2018), pp. 280–292.

[157] Hua Zhang et al. "Wide genetic variation in the native pial collateral circulation is a major determinant of variation in severity of stroke". In: *Journal of Cerebral Blood Flow & Metabolism* 30.5 (2010), pp. 923–934.

[158] Shiliang Wang et al. "Genetic architecture underlying variation in extent and remodeling of the collateral circulation". In: *Circulation research* 107.4 (2010), pp. 558–568.

[159] Juha-Pekka Pienimäki et al. "Carotid Artery Stenosis Is Associated with Better Intracranial Collateral Circulation in Stroke Patients". In: *Cerebrovascular Diseases* 49.2 (2020), pp. 200–205.

[160] Elisa Cuccione et al. "Cerebral collateral circulation in experimental ischemic stroke". In: *Experimental & translational stroke medicine* 8.1 (2016), pp. 1–9.

[161] Daniel J Beard et al. "Intracranial pressure elevation reduces flow through collateral vessels and the penetrating arterioles they supply. A possible explanation for 'collateral failure'and infarct expansion after ischemic stroke". In: *Journal of Cerebral Blood Flow & Metabolism* 35.5 (2015), pp. 861–872.

[162] James E Faber et al. "Aging causes collateral rarefaction and increased severity of ischemic injury in multiple tissues". In: *Arteriosclerosis, thrombosis, and vascular biology* 31.8 (2011), pp. 1748–1756.

[163] Scott M Moore et al. "Cardiovascular risk factors cause premature rarefaction of the collateral circulation and greater ischemic tissue injury". In: *Angiogenesis* 18.3 (2015), pp. 265–281.

[164] Hua Zhang, Bo Jin, and James E Faber. "Mouse models of Alzheimer's disease cause rarefaction of pial collaterals and increased severity of ischemic stroke". In: *Angiogenesis* 22.2 (2019), pp. 263–279.

[165] Wojciech Rzechorzek et al. "Aerobic exercise prevents rarefaction of pial collaterals and increased stroke severity that occur with aging". In: *Journal of Cerebral Blood Flow & Metabolism* 37.11 (2017), pp. 3544–3555.

[166] Sulagna Dutta and Pallav Sengupta. "Men and mice: relating their ages". In: *Life sciences* 152 (2016), pp. 244–248.

[167] Ethem Murat Arsava et al. "The detrimental effect of aging on leptomeningeal collaterals in ischemic stroke". In: *Journal of Stroke and Cerebrovascular Diseases* 23.3 (2014), pp. 421–426.

[168] Stefania Nannoni et al. "Determining factors of better leptomeningeal collaterals: a study of 857 consecutive acute ischemic stroke patients". In: *Journal of neurology* 266.3 (2019), pp. 582–588.

[169] Bijoy K Menon et al. "Leptomeningeal collaterals are associated with modifiable metabolic risk factors". In: *Annals of neurology* 74.2 (2013), pp. 241–248.

[170] Henry M Vander Eecken and Raymond D Adams. "The anatomy and functional significance of the meningeal arterial anastomoses of the human brain". In: *Journal of neuropathology and experimental neurology* 12.2 (1953), pp. 132–157.

[171] F McVerry, DS Liebeskind, and KW Muir. "Systematic review of methods for assessing leptomeningeal collateral flow". In: *American journal of neuroradiology* 33.3 (2012), pp. 576–582.

[172] Junqiang Ma et al. "Impaired collateral flow in pial arterioles of aged rats during ischemic stroke". In: *Translational stroke research* 11.2 (2020), pp. 243–253.

[173] William A. Banks et al. "Healthy aging and the blood–brain barrier". In: *Nature Aging* 1.3 (2021), pp. 243–254.

[174] Inge CM Verheggen et al. "Increase in blood–brain barrier leakage in healthy, older adults". In: *GeroScience* 42.4 (2020), pp. 1183–1193.

[175] Axel Montagne et al. "Blood-brain barrier breakdown in the aging human hippocampus". In: *Neuron* 85.2 (2015), pp. 296–302.

[176] Dema Abdelkarim et al. "A neural-vascular complex of age-related changes in the human brain: anatomy, physiology, and implications for neurocognitive aging". In: *Neuroscience & Biobehavioral Reviews* 107 (2019), pp. 927–944.

[177] Dimitris Tousoulis et al. "The role of nitric oxide on endothelial function". In: *Current vascular pharmacology* 10.1 (2012), pp. 4–18.

[178] M Tesauro et al. "Arterial ageing: from endothelial dysfunction to vascular calcification". In: *Journal of internal medicine* 281.5 (2017), pp. 471–482.

[179] Marıa Dolores Herrera et al. "Endothelial dysfunction and aging: an update". In: *Ageing research reviews* 9.2 (2010), pp. 142–152.

[180] Michael S Goligorsky. "Microvascular rarefaction: the decline and fall of blood vessels". In: *Organogenesis* 6.1 (2010), pp. 1–10.

[181] Yukihito Higashi, Yasuki Kihara, and Kensuke Noma. "Endothelial dysfunction and hypertension in aging". In: *Hypertension Research* 35.11 (2012), pp. 1039–1047.

[182] Eric Thorin and Nathalie Thorin-Trescases. "Vascular endothelial ageing, heartbeat after heartbeat". In: *Cardiovascular research* 84.1 (2009), pp. 24–32.

[183] Anthony J Donato, Daniel R Machin, and Lisa A Lesniewski. "Mechanisms of dysfunction in the aging vasculature and role in age-related disease". In: *Circulation Research* 123.7 (2018), pp. 825–848.

[184] Shahar Lavi et al. "Impaired cerebral CO2 vasoreactivity: association with endothelial dysfunction". In: *American Journal of Physiology-Heart and Circulatory Physiology* 291.4 (2006), H1856–H1861.

[185] Shahar Lavi et al. "Role of nitric oxide in the regulation of cerebral blood flow in humans: chemoregulation versus mechanoregulation". In: *Circulation* 107.14 (2003), pp. 1901–1905.

[186] Hai-na Zhang et al. "Endothelial dysfunction in diabetes and hypertension: role of microRNAs and long non-coding RNAs". In: *Life sciences* 213 (2018), pp. 258–268.

[187] Patrice Brassard et al. "Losing the dogmatic view of cerebral autoregulation". In: *Physiological reports* 9.15 (2021), e14982.

[188] Jurgen AHR Claassen et al. "Regulation of cerebral blood flow in humans: physiology and clinical implications of autoregulation". In: *Physiological Reviews* (2021).

[189] JW Hamner, Keita Ishibashi, and Can Ozan Tan. "Revisiting human cerebral blood flow responses to augmented blood pressure oscillations". In: *The Journal of physiology* 597.6 (2019), pp. 1553–1564.

[190] Can Ozan Tan. "Defining the characteristic relationship between arterial pressure and cerebral flow". In: *Journal of applied physiology* 113.8 (2012), pp. 1194–1200.

[191] Gabriela A Santos et al. "Pathophysiologic differences in cerebral autoregulation after subarachnoid hemorrhage". In: *Neurology* 86.21 (2016), pp. 1950–1956.

[192] Nicolai Goettel et al. "Monitoring of cerebral blood flow autoregulation in adults undergoing sevoflurane anesthesia: a prospective cohort study of two age groups". In: *Journal of clinical monitoring and computing* 30.3 (2016), pp. 255–264.

[193] SVEND Strandgaard. "Autoregulation of cerebral blood flow in hypertensive patients. The modifying influence of prolonged antihypertensive treatment on the tolerance to acute, drug-induced hypotension." In: *Circulation* 53.4 (1976), pp. 720–727.

[194] Hsin-Wen Chen et al. "Magnetic resonance angiographic evaluation of circle of Willis in general population: a morphologic study in 507 cases". In: 29.5 (2004), pp. 223–229.

[195] G Cavill, EJ Simpson, and RP Mahajan. "Factors affecting assessment of cerebral autoregulation using the transient hyperaemic response test". In: *British journal of anaesthesia* 81.3 (1998), pp. 317–321.

[196] Stephan J Schreiber et al. "Assessment of blood flow velocity and diameter of the middle cerebral artery during the acetazolamide provocation test by use of transcranial Doppler sonography and MR imaging". In: *American Journal of Neuroradiology* 21.7 (2000), pp. 1207–1211.

[197] David H Evans. "On the measurement of the mean velocity of blood flow over the cardiac cycle using Doppler ultrasound". In: *Ultrasound in medicine & biology* 11.5 (1985), pp. 735–741.

[198] JM Harrison, KJ Girling, and RP Mahajan. "Effects of target-controlled infusion of propofol on the transient hyperaemic response and carbon dioxide reactivity in the middle cerebral artery". In: *British journal of anaesthesia* 83.6 (1999), pp. 839–844.

[199] Daan LK de Jong et al. "Lack of linear correlation between dynamic and steady-state cerebral autoregulation". In: *The Journal of physiology* 595.16 (2017), pp. 5623–5636.

[200] Arenda HEA Van Beek et al. "Cerebral autoregulation: an overview of current concepts and methodology with special focus on the elderly". In: *Journal of Cerebral Blood Flow & Metabolism* 28.6 (2008), pp. 1071–1085.

[201] Bart Spronck et al. "A lumped parameter model of cerebral blood flow control combining cerebral autoregulation and neurovascular coupling". In: *American Journal of Physiology-Heart and Circulatory Physiology* 303.9 (2012), H1143–H1153.

[202] Marit L Sanders et al. "Dynamic cerebral autoregulation reproducibility is affected by physiological variability". In: *Frontiers in physiology* 10 (2019), p. 865.

[203] Chang-Yang Xing et al. "Arterial pressure, heart rate, and cerebral hemodynamics across the adult life span". In: *Hypertension* 69.4 (2017), pp. 712–720.

[204] Kayla B Stefanidis et al. "Healthy aging affects cerebrovascular reactivity and pressure-flow responses, but not neurovascular coupling: a cross-sectional study". In: *PLoS One* 14.5 (2019), e0217082.

[205] Santiago Ortega-Gutierrez et al. "Reliability, asymmetry, and age influence on dynamic cerebral autoregulation measured by spontaneous fluctuations of blood pressure and cerebral blood flow velocities in healthy individuals". In: *Journal of Neuroimaging* 24.4 (2014), pp. 379–386.

[206] Lewis A Lipsitz et al. "Dynamic regulation of middle cerebral artery blood flow velocity in aging and hypertension". In: *Stroke* 31.8 (2000), pp. 1897–1903.

[207] Jonathan D Smirl et al. "Relationship between blood pressure and cerebral blood flow during supine cycling: influence of aging". In: *Journal of Applied Physiology* 120.5 (2016), pp. 552–563.

[208] Fiona G Brodie et al. "Long-term changes in dynamic cerebral autoregulation: a 10 years follow up study". In: *Clinical physiology and functional imaging* 29.5 (2009), pp. 366–371.

[209] Angus P Batterham et al. "Does depth of squat-stand maneuver affect estimates of dynamic cerebral autoregulation?" In: *Physiological reports* 8.16 (2020), e14549.

[210] Navpreet Reehal et al. "Differentiating Dynamic Cerebral Autoregulation Across Vascular Territories". In: *Frontiers in Neurology* 12 (2021), p. 365.

[211] Lingzhong Meng and Adrian W Gelb. "Regulation of cerebral autoregulation by carbon dioxide". In: *Anesthesiology* 122.1 (2015), pp. 196–205.

[212] Peiying Liu, B Jill, and Hanzhang Lu. "Cerebrovascular reactivity (CVR) MRI with CO2 challenge: a technical review". In: *Neuroimage* 187 (2019), pp. 104–115.

[213] Christopher K Willie et al. "Integrative regulation of human brain blood flow". In: *The Journal of physiology* 592.5 (2014), pp. 841–859.

[214] CK Willie et al. "Regional brain blood flow in man during acute changes in arterial blood gases". In: *The Journal of physiology* 590.14 (2012), pp. 3261–3275.

[215] Gerdi Kemmer and Sandro Keller. "Nonlinear least-squares data fitting in Excel spreadsheets". In: *Nature protocols* 5.2 (2010), pp. 267–281.

[216] JULIUS Melbin et al. "Coherence of cardiac output with rate changes". In: *American Journal of Physiology-Heart and Circulatory Physiology* 243.4 (1982), H499–H504.

[217] Tsubasa Tomoto et al. "Cerebral vasomotor reactivity during hypo-and hypercapnia across the adult lifespan". In: *Journal of Cerebral Blood Flow & Metabolism* 40.3 (2020), pp. 600–610.

[218] SD Galvin et al. "Effects of age and coronary artery disease on cerebrovascular reactivity to carbon dioxide in humans". In: *Anaesthesia and intensive care* 38.4 (2010), pp. 710–717.

[219] Madelijn H Oudegeest-Sander et al. "Assessment of dynamic cerebral autoregulation and cerebrovascular CO2 reactivity in ageing by measurements of cerebral blood flow and cortical oxygenation". In: *Experimental physiology* 99.3 (2014), pp. 586–598.

[220] Carissa J Murrell et al. "Cerebral blood flow and cerebrovascular reactivity at rest and during sub-maximal exercise: effect of age and 12-week exercise training". In: *Age* 35.3 (2013), pp. 905–920.

[221] Yong-Sheng Zhu et al. "Cerebral vasomotor reactivity during hypo-and hypercapnia in sedentary elderly and Masters athletes". In: *Journal of Cerebral Blood Flow & Metabolism* 33.8 (2013), pp. 1190–1196.

[222] Shigehiko Ogoh et al. "Effects of acute hypoxia on cerebrovascular responses to carbon dioxide". In: *Experimental physiology* 99.6 (2014), pp. 849–858.

[223] Feng Xu et al. "Effect of hypoxia and hyperoxia on cerebral blood flow, blood oxygenation, and oxidative metabolism". In: *Journal of Cerebral Blood Flow & Metabolism* 32.10 (2012), pp. 1909–1918.

[224] A MURRAY Harper and HI Glass. "Effect of alterations in the arterial carbon dioxide tension on the blood flow through the cerebral cortex at normal and low arterial blood pressures." In: *Journal of neurology, neurosurgery, and psychiatry* 28.5 (1965), p. 449.

[225] PIYUSH M Patel, JOHN C Drummond, BRIAN P Lemkuil, et al. "Cerebral physiology and the effects of anesthetic drugs". In: *Miller's anesthesia* 1 (2010), pp. 594–674.

[226] Eiichi Hirano et al. "Functional rescue of elastin insufficiency in mice by the human elastin gene: implications for mouse models of human disease". In: *Circulation research* 101.5 (2007), pp. 523–531.

[227] Douglas E Busby and Alan C Burton. "The effect of age on the elasticity of the major brain arteries". In: *Canadian journal of physiology and pharmacology* 43.2 (1965), pp. 185–202.

[228] MJ Mulvany and DM Warshaw. "The active tension-length curve of vascular smooth muscle related to its cellular components." In: *The Journal of general physiology* 74.1 (1979), pp. 85–104.

[229] Brian E Carlson and Timothy W Secomb. "A theoretical model for the myogenic response based on the length–tension characteristics of vascular smooth muscle". In: *Microcirculation* 12.4 (2005), pp. 327–338.

[230] Shiro Nagasawa et al. "Biomechanical study on aging changes and vasospasm of human cerebral arteries". In: *Biorheology* 19.3 (1982), pp. 481–489.

[231] Jeanette Mitchell. "Differences between left and right suboccipital and intracranial vertebral artery dimensions: an influence on blood flow to the hindbrain?" In: *Physiotherapy research international* 9.2 (2004), pp. 85–95.

[232] G Gamble et al. "B-mode ultrasound images of the carotid artery wall: correlation of ultrasound with histological measurements". In: *Atherosclerosis* 102.2 (1993), pp. 163–173.

[233] Goran Spasojević et al. "Internal carotid and vertebral arteries diameters and their interrelationships to sex and left/right side". In: *Folia Morphologica* 79.2 (2020), pp. 219–225.

[234] Nathalie Thorin-Trescases et al. "Diameter dependence of myogenic tone of human pial arteries: possible relation to distensibility". In: *Stroke* 28.12 (1997), pp. 2486–2492.

[235] Christopher Imray et al. "Time course variations in the mechanisms by which cerebral oxygen delivery is maintained on exposure to hypoxia/altitude". In: *High altitude medicine & biology* 15.1 (2014), pp. 21–27.

[236] Mark H Wilson et al. "Cerebral artery dilatation maintains cerebral oxygenation at extreme altitude and in acute hypoxia—an ultrasound and MRI study". In: *Journal of Cerebral Blood Flow & Metabolism* 31.10 (2011), pp. 2019–2029.

[237] Pablo J Blanco, Lucas O Müller, and J David Spence. "Blood pressure gradients in cerebral arteries: a clue to pathogenesis of cerebral small vessel disease". In: *Stroke and vascular neurology* 2.3 (2017).

[238] Maha Coucha et al. "Impact of metabolic diseases on cerebral circulation: structural and functional consequences". In: *Comprehensive Physiology* 8.2 (2018), p. 773.

[239] Nobuhide Masawa et al. "Morphometry of structural preservation of tunica media in aged and hypertensive human intracerebral arteries." In: *Stroke* 25.1 (1994), pp. 122–127.

[240] Marilyn J Cipolla et al. "Threshold duration of ischemia for myogenic tone in middle cerebral arteries: effect on vascular smooth muscle actin". In: *Stroke* 32.7 (2001), pp. 1658–1664.

[241] Johan Fredrik Brekke, Natalia I Gokina, and George Osol. "Vascular smooth muscle cell stress as a determinant of cerebral artery myogenic tone". In: *American Journal of Physiology-Heart and Circulatory Physiology* 283.6 (2002), H2210–H2216.

[242] Brian E Carlson, Julia C Arciero, and Timothy W Secomb. "Theoretical model of blood flow autoregulation: roles of myogenic, shear-dependent, and metabolic responses". In: *American Journal of Physiology-Heart and Circulatory Physiology* 295.4 (2008), H1572–H1579.

[243] Yuansheng Gao. *Biology of vascular smooth muscle: vasoconstriction and dilatation*. Vol. 8. Springer, 2017.

[244] Shigehiko Ogoh and Takashi Tarumi. "Cerebral blood flow regulation and cognitive function: a role of arterial baroreflex function". In: *The journal of physiological sciences* 69.6 (2019), pp. 813–823.

[245] Ramakrishna Mukkamala et al. "Estimation of arterial and cardiopulmonary total peripheral resistance baroreflex gain values: validation by chronic arterial baroreceptor denervation". In: *American Journal of Physiology-Heart and Circulatory Physiology* 290.5 (2006), H1830–H1836.

[246] Henry Raymundo et al. "Cardiovascular control by arterial and cardiopulmonary baroreceptors in awake dogs with atrioventricular block". In: *American Journal of Physiology-Heart and Circulatory Physiology* 257.6 (1989), H2048–H2058.

[247] JW Hamner and Can Ozan Tan. "Relative contributions of sympathetic, cholinergic, and myogenic mechanisms to cerebral autoregulation". In: *Stroke* 45.6 (2014), pp. 1771–1777.

[248] Takashi Tarumi and Rong Zhang. "Cerebral blood flow in normal aging adults: cardiovascular determinants, clinical implications, and aerobic fitness". In: *Journal of neurochemistry* 144.5 (2018), pp. 595–608.

[249] SJ Sherwin et al. "One-dimensional modelling of a vascular network in space-time variables". In: *Journal of engineering mathematics* 47.3 (2003), pp. 217–250.

[250] Jordi Alastruey Arimon. "Numerical modelling of pulse wave propagation in the cardiovascular system: development, validation and clinical applications". PhD thesis. Imperial College London (University of London), 2006.

[251] A Cengel Yunus. *Fluid Mechanics: Fundamentals And Applications (Si Units).* Tata McGraw Hill Education Private Limited, 2010.

[252] Vuk Milišić and Alfio Quarteroni. "Analysis of lumped parameter models for blood flow simulations and their relation with 1D models". In: *ESAIM: Mathematical modelling and numerical analysis* 38.4 (2004), pp. 613–632.

[253] Jaiyoung Ryu, Xiao Hu, and Shawn C Shadden. "A coupled lumped-parameter and distributed network model for cerebral pulse-wave hemodynamics". In: *Journal of biomechanical engineering* 137.10 (2015).

[254] NP Smith, AJ Pullan, and Peter J Hunter. "An anatomically based model of transient coronary blood flow in the heart". In: *SIAM Journal on Applied mathematics* 62.3 (2002), pp. 990–1018.

[255] Mette S Olufsen et al. "Numerical simulation and experimental validation of blood flow in arteries with structured-tree outflow conditions". In: *Annals of biomedical engineering* 28.11 (2000), pp. 1281–1299.

[256] Brooke N Steele et al. "In vivo validation of a one-dimensional finite-element method for predicting blood flow in cardiovascular bypass grafts". In: *IEEE Transactions on Biomedical Engineering* 50.6 (2003), pp. 649–656.

[257] Jordi Alastruey et al. "Physical determining factors of the arterial pulse waveform: theoretical analysis and calculation using the 1-D formulation". In: *Journal of Engineering Mathematics* 77.1 (2012), pp. 19–37.

[258] David Bessems, Marcel Rutten, and Frans Van De Vosse. "A wave propagation model of blood flow in large vessels using an approximate velocity profile function". In: *Journal of Fluid Mechanics* 580 (2007), pp. 145–168.

[259] Jordi Alastruey, Kim H Parker, and Spencer J Sherwin. "Arterial pulse wave haemodynamics". In: *11th international conference on pressure surges*. Virtual PiE Led t/a BHR Group. 2012, pp. 401–443.

[260] Alfio Quarteroni and Luca Formaggia. "Mathematical modelling and numerical simulation of the cardiovascular system". In: *Handbook of numerical analysis* 12 (2004), pp. 3–127.

[261] Clément Cancès and Pascal Omnes. "Finite Volumes for Complex Applications VIII Hyperbolic, Elliptic and Parabolic Problems". In: ().

[262] Tao Du, Dan Hu, and David Cai. "Outflow boundary conditions for blood flow in arterial trees". In: *PLoS One* 10.5 (2015), e0128597.

[263] Ido R Van Den Wijngaard et al. "Assessment of collateral status by dynamic CT angiography in acute MCA stroke: timing of acquisition and relationship with final infarct volume". In: *American Journal of Neuroradiology* 37.7 (2016), pp. 1231–1236.

[264] Mark Connolly et al. "Reproduction of consistent pulse-waveform changes using a computational model of the cerebral circulatory system". In: *Medical engineering & physics* 36.3 (2014), pp. 354–363.

[265] Mauro Ursino and Carlo Alberto Lodi. "A simple mathematical model of the interaction between intracranial pressure and cerebral hemodynamics". In: *Journal of Applied Physiology* 82.4 (1997), pp. 1256–1269.

[266] Mark H Wilson. "Monro-Kellie 2.0: The dynamic vascular and venous pathophysiological components of intracranial pressure". In: *Journal of Cerebral Blood Flow & Metabolism* 36.8 (2016), pp. 1338–1350.

[267] Xiao Hu et al. "Estimation of hidden state variables of the intracranial system using constrained nonlinear Kalman filters". In: *IEEE transactions on biomedical engineering* 54.4 (2007), pp. 597–610.

[268] CJ Chuong and YC Fung. "Compressibility and constitutive equation of arterial wall in radial compression experiments". In: *Journal of biomechanics* 17.1 (1984), pp. 35–40.

[269] M Ursino et al. "Cerebral hemodynamics during arterial and CO2 pressure changes: in vivo prediction by a mathematical model". In: *American Journal of Physiology-Heart and Circulatory Physiology* 279.5 (2000), H2439–H2455.

[270] Jasper Snoek, Hugo Larochelle, and Ryan P Adams. "Practical bayesian optimization of machine learning algorithms". In: *Advances in neural information processing systems* 25 (2012).

[271] Wei-Liem Loh. "On Latin hypercube sampling". In: *The annals of statistics* 24.5 (1996), pp. 2058–2080.